

**ULTRASONIC MEASUREMENTS FOR THE EVALUATION OF
THERMAL FATIGUE DAMAGE**

A Thesis Submitted to the College of Graduate Studies and Research

in Partial Fulfillment of the Requirements

for the Degree of Master of Science

in the Department of Electrical Engineering

University of Saskatchewan

Saskatoon

By

David Sean Forsyth

September, 1992

Copyright © 1992: David Sean Forsyth

COPYRIGHT

The author has agreed that the Library, University of Saskatchewan, may make this thesis freely available for inspection. Moreover, the author has agreed that permission for extensive copying of this thesis for scholarly purposes may be granted by the Professor who supervised the thesis work recorded herein, or in his absence, by the Head of the Department or the Dean of the College in which the thesis work was done. It is understood that due recognition will be given to the author of this thesis and to the University of Saskatchewan in any use of the material in this thesis. Copying or publication or any other use of this thesis for financial gain without approval by the University of Saskatchewan and the author's written permission is prohibited.

Requests for permission to copy or to make any other use of the material of this thesis in whole or in part should be addressed to:

Head of the Department of Electrical Engineering

University of Saskatchewan

Saskatoon, Canada S7N 0W0

ACKNOWLEDGEMENTS

I would like to thank my supervisors Dr. S.O. Kasap and Dr. S. Yannacopoulos for their direction and assistance in this project. I am grateful for technical assistance from Phil Seminoff and Lloyd Litwin, and for use of the thermal cycling apparatus and associated work performed by Ian Wacker. The assistance of Maurice Romaniuk in the image analysis measurements was greatly appreciated.

I would like to thank my colleagues for many useful discussions and helpful advice, and my friends for their support and encouragement. I am especially grateful to my parents for their constant support.

University of Saskatchewan

Electrical Engineering Abstract #92A368

Ultrasonic Measurements for the Evaluation of Thermal Fatigue Damage

Student: D.S. Forsyth

Supervisors: S.O. Kasap, S. Yannacopoulos

M. Sc. Thesis Submitted to the
College of Graduate Studies and Research
September 1992

ABSTRACT

An ultrasonic test system was assembled to evaluate the ability of ultrasonic measurements to measure thermal fatigue damage in composite material systems. The ultrasonic test system used a modification of the ring-around technique. The sample to be studied was placed between a transmitting and a receiving transducer, and the time between the first peak on the transmitted waveform and the first peak of the received waveform was measured as the transit time through the sample. The peak to peak voltage at both transducers was also measured, and used to define an attenuation.

Cyclic thermal fatigue loading was carried out on three fibre-reinforced plastics, two uniaxial and one randomly oriented. Before any loading, and at intervals during loading, measurements of ultrasonic velocities and attenuations at frequencies of 3.00, 4.00, and 5.00MHz were performed. These measurements were made for a number of samples, normalized, and averaged. Generally it was found that ultrasonic attenuations increased and ultrasonic velocities decreased with increasing number of thermal fatigue cycles. This depended on the material tested and the propagation direction of the ultrasound. Scanning electron microscopy (SEM) was used as a qualitative tool to examine specimens after fatigue to provide information on the modes of stress relief in the specimens.

It was found that ultrasonic attenuation is sensitive to thermal fatigue damage in these materials. The main mode of damage is fibre-matrix debonding at the fibre ends, occasionally accompanied by matrix cracking. This is demonstrated by the SEM examinations of the fatigued specimens. A damaged surface layer in the uniaxial composites did not have a great effect on the bulk properties of the specimens, and ultrasonic velocities were not always sensitive to damage, due to the nature of the stress relief.

TABLE OF CONTENTS

COPYRIGHT	-i-
ACKNOWLEDGEMENTS	-ii-
ABSTRACT	-iii-
TABLE OF CONTENTS	-iv-
LIST OF TABLES	-viii-
LIST OF FIGURES	-ix-
LIST OF ABBREVIATIONS	-xv-
1.INTRODUCTION	1
1.1 Ultrasonics	1
1.2 Composite Materials	2
1.3 Research Objectives	4
1.4 Thesis Outline	5

2. ULTRASOUND GENERATION AND PROPAGATION	6
2.1 Introduction	6
2.2 Hooke's Law	8
2.2.1 Stress Tensor	8
2.2.2 Strain Tensor	10
2.2.3 Elastic Moduli	11
2.3 Linear Elastic Wave Theory	13
2.3.1 Characteristic Acoustic Impedance	16
2.4 Ultrasonic Velocity	17
2.5 Ultrasonic Attenuation	19
2.6 Ultrasonic Waves	20
2.7 Wave Excitation	21
2.7.1 Piezoelectricity	22
2.7.2 Ferroelectricity	24
2.7.3 Piezoelectric Transducers	25
3. ULTRASONIC MEASUREMENT TECHNIQUES	30
3.1 Introduction	30
3.2 The Sing-Around Technique	30
3.2.1 Absolute Velocity	32
3.2.2 Absolute Attenuation	33
3.3 Other Ultrasonic NDT Techniques	33

3.4 Scanning Electron Microscopy	36
4. EXPERIMENTAL APPARATUS AND PROCEDURES	37
4.1 Experimental Apparatus	37
4.1.1 Circuit Timing and Triggering	38
4.1.2 Transducers	39
4.1.3 Signal Amplification	41
4.1.4 Oscilloscope Measurements	46
4.1.5 Scanning Electron Microscopy	47
4.2 Test Materials	48
4.2.1 Properties	49
4.2.2 Sample Preparation	51
4.3 Thermal Cycling	53
5. RESULTS AND DISCUSSION	55
5.1 Thermal Cycling	55
5.2 Composite 1: Carbon Fibres in Vinylester Matrix	58
5.2.1 Determination of Ultrasonic Velocity and Attenuation	59
5.2.2 Ultrasonic Waves Perpendicular to the Fibre Axis	
(Composite 1)	65
5.2.3 Ultrasonic Waves Parallel to the Fibre Axis (Composite 1) ..	71
5.3 Composite 2: Aramid Fibres in Vinylester	75

5.3.1 Determination of Ultrasonic Velocity and Attenuation	75
5.3.2 Ultrasonic Waves Perpendicular to the Fibre Axis (Composite 2)	79
5.3.3 Ultrasonic Waves Parallel to the Fibre Axis (Composite 2) . .	85
5.4 Composite 3: Aramid Fibres in Polyphenylene Sulphide	89
5.4.1 Determination of Absolute Velocity and Attenuation	89
5.4.2 Ultrasonic Waves in Composite 3	93
5.5 Discussion	97
6. CONCLUSIONS AND RECOMMENDATIONS FOR FUTURE WORK	103
6.1 Conclusions	103
6.2 Recommendations for Future Work	104
References	106
APPENDIX A: MODELS OF INTERFACIAL STRESSES	111
A.1 Introduction	111
A.2 Modelling	111
A.2.1 Chawla's Model	111
A.2.2 Chamis' Model	113
A.3 Modelling Results	114

LIST OF TABLES

Table 2.1	Equivalent indices for contracted notation.	18
Table 2.2	A comparison of different piezoelectric materials (from [15] except for * from manufacturer's specifications).	25
Table 4.1	Properties of component materials. Asterix indicates from manufacturer's specifications.	50
Table 4.2	Fibre content of the composites.	50
Table 5.1	Absolute velocity and attenuation values for composite 1 (unfatigued).	65
Table 5.2	Absolute velocity and attenuation values for composite 2 (unfatigued).	76
Table 5.3	Absolute velocity and attenuation values for composite 3 (unfatigued).	90
Table 5.4	A summary of the materials examined.	97

LIST OF FIGURES

Fig. 2.1	Mass-spring model of crystalline structure.	6
Fig. 2.2	Examples of crystal imperfections affecting wave propagation: a) substitution and b) interstitial atom.	7
Fig. 2.3	Forces acting on the surface of a small cube of a solid.	9
Fig. 2.5	Comparison of centre symmetric structure to non-centre symmetric. (after Beam [16]).	23
Fig. 2.4	Showing motion of top layer of particles for Rayleigh waves, with oscillation ellipse on right. (After Krautkramer and Krautkramer[2].)	21
Fig. 2.6	Equivalent electrical circuit for a piezoelectric transformer at resonance (after Blitz [15]).	26
Fig. 3.1	A functional block diagram of the sing-around technique for ultrasonic velocity measurement.	31
Fig. 4.1	Block diagram of system used in this study.	37
Fig. 4.2	Timing for the modified sing-around apparatus.	38
Fig. 4.3	Transducer and specimen mounting arrangement.	41
Fig. 4.4	Implementation of the PA19 power amplifier.	42
Fig. 4.5	Performance data for the PA19 based transmitter amplifier.	44
Fig. 4.6	Design of output amplifier.	45
Fig. 4.7	Performance of output amplifier.	46
Fig. 4.8	Specimens cut from composites 1 and 2 (transversely isotropic). ...	52

Fig. 4.9	A block diagram of the thermal cycling apparatus.	54
Fig. 5.1	Temperature versus time plot for thermal cycle schedules: a) schedule 1 and b) schedule 2. Composite 1 test sample.	57
Fig. 5.2	Schematic of transducer assembly for absolute measurement derivations.	60
Fig. 5.3	Dependence of transit time on specimen length. (Graph used for determination of v_{\parallel} for composite 1.)	63
Fig. 5.4	Dependence of attenuation on specimen length. (Graph used for determination of α_{\parallel} for composite 1.)	64
Fig. 5.5	Graph of velocity and attenuation changes for composite 1: longitudinal wave perpendicular to fibre axis (thermal cycle schedule 1).	67
Fig. 5.6	Graph of velocity and attenuation changes for composite 1: longitudinal wave perpendicular to fibre axis (thermal cycle schedule 2).	68
Fig. 5.7	SEM photograph of composite 1, 2000 \times magnification, unfatigued.	69
Fig. 5.8	SEM photograph of composite 1, 2000 \times magnification, 1000 cycles (schedule 2).	69
Fig. 5.9	SEM photograph of composite 1, 3500 \times magnification, unfatigued.	70

Fig. 5.10	SEM photograph of composite 1, 3500× magnification, 1000 cycles (schedule 2).	70
Fig. 5.11	Graph of velocity and attenuation changes for composite 1: longitudinal wave parallel to fibre axis (thermal cycle schedule 2)	72
Fig. 5.12	SEM photograph of composite 1, perpendicular to fibre axis. The magnification is 350×, and the specimen is unfatigued.	73
Fig. 5.13	SEM photograph of unfatigued specimen of composite 1, 5000× magnification. See Figures 5.14 and 5.15 for comparison.	73
Fig. 5.14	SEM photograph of composite 1, after 800 cycles (schedule 2). Magnification is 5000×. Note low fibre density.	74
Fig. 5.15	SEM photograph of composite 1 after 600 cycles (schedule 2). Magnification is 7500×.	74
Fig. 5.16	Dependence of transit time on specimen length. (Graph used for determination of v_{\parallel} for composite 2.)	77
Fig. 5.17	Dependence of attenuation on specimen length. (Graph used for determination of α_{\parallel} for composite 2.)	78
Fig. 5.18	Graph of velocity and attenuation changes for composite 2: longitudinal wave perpendicular to fibre axis (thermal cycle schedule 2).	80
Fig. 5.19	SEM photograph of composite 2, unfatigued at 350× magnification.	82

Fig. 5.20	SEM photograph of composite 2, unfatigued at 1500× magnification. Note fibre ends at edge of specimen (see Figures 5.23, 5.24).	82
Fig. 5.21	SEM photograph of composite 2, after 500 cycles (schedule 1) at 200× magnification. Note matrix cracking at surface.	83
Fig. 5.22	SEM photograph of composite 2 at 1000× magnification, after 500 cycles (schedule 1). Note fibre pullout.	83
Fig. 5.23	SEM photograph of composite 2 at 500× magnification, after 1000 cycles (schedule 2). Note fibres pulled out from matrix.	84
Fig. 5.24	SEM photograph of composite 2: same view as Figure 5.23, at 1500× magnification.	84
Fig. 5.25	Graph of velocity and attenuation changes for composite 2: longitudinal wave parallel to fibre axis (thermal cycle schedule 2).	86
Fig. 5.26	SEM photograph of composite 2 unfatigued at 1000× magnification.	87
Fig. 5.27	SEM photograph of composite 2 after 1000 cycles (schedule 2) at 1000× magnification.	87
Fig. 5.28	SEM photograph of composite 2 unfatigued at 3500× magnification.	88
Fig. 5.29	SEM photograph of composite 2, after 800 cycles (schedule 1) at 3500× magnification.	88

Fig. 5.30	Dependence of transit time on specimen length. (Graph for determination of absolute velocity for composite 3.)	91
Fig. 5.31	Dependence of attenuation on specimen length. (Graph for determination of absolute attenuation for composite 3.)	92
Fig. 5.32	Graph of velocity and attenuation changes for composite : longitudinal wave in random fibre orientation (thermal cycle schedule 1).	94
Fig. 5.33	SEM photograph of composite 3 at 200× magnification, unfatigued.	95
Fig. 5.34	SEM photograph of composite 3 at 2000× magnification, unfatigued.	95
Fig. 5.35	SEM photograph of composite 3, after 1000 cycles (schedule 2), at 2000× magnification. Note fibre pullout.	96
Fig. 5.36	SEM photograph of composite 3, after 1000 cycles (schedule 2), at 3500× magnification. Again note separation of fibre from matrix.	96
Fig. A.1	Geometrical arrangement of composite for Chawla and Chamis models.	113
Fig. A.2	Schematic of shear stress variation in composite.	115
Fig. A.3	Models of interfacial shear stress for composite 1 as a function of distance from the end of the specimen.	117

Fig. A.4 Models of interfacial shear stress for composite 1 as a function
of distance from the end of the specimen. 118

LIST OF ABBREVIATIONS

FRP	fibre reinforced plastic(s)
NDE	non-destructive evaluation
NDI	non-destructive inspection
NDT	non-destructive testing
PEO	pulse-echo overlap
PPS	polyphenylene sulphide
PZT	lead zirconate titanate
RF	radio frequency
ULSI	ultra-large scale integration
VLSI	very large scale integration

1.INTRODUCTION

1.1 Ultrasonics

Ultrasound is defined as sound of frequencies greater than 20kHz, the normal limit of human hearing. Non-destructive testing (NDT) of materials is defined as any method of testing which yields information without causing any permanent change in material properties. Other terms used interchangeably are non-destructive inspection (NDI) and non-destructive evaluation (NDE), the only difference being that NDE usually implies an acceptance or rejection of the material or component being examined[1].

The beginnings of the use of ultrasound for NDT were in 1929[2] when Sokolow measured variations in the intensity of transmitted sound across specimens to locate defects. Since the Second World War, ultrasonic NDT has become very popular and is an accepted and well studied technique.

Frequencies used for testing depend on the material involved, but commonly range from 100kHz to 10MHz. Laser generation of ultrasound can involve frequencies in the tens of gigahertz range. The use of high frequency or short wavelength sound in the evaluation of material properties has benefits because as the wavelength becomes small with respect to specimen size, it can be better focussed. Smaller wavelengths also imply better resolution and increased sensitivity to specimen inhomogeneities.

1.2 Composite Materials

Advances in technology require better materials, suited to individual applications. Composite materials ideally allow the designer to change the material to fit the design, rather than changing designs to accommodate less than optimum materials. Composite materials can be defined as any man-made material consisting of two or more distinct components, with a definite interface. The major difference between composites and alloys is the homogeneity of the mixture: alloys are generally homogeneous on a smaller scale.

Because of the different distinct components which make up composite materials, their properties are often described in terms of the properties of the individual components by what are called mixture rules[3]. These rules are based on the relative amounts of the different components, and their geometries. These mixture rules can be applied to any multiphase material, with varying success depending on the knowledge of the actual makeup of the composite. Mixture rules are used not only to describe mechanical properties of solids, but electrical and thermal properties as well[4]. They are used in calculations of properties for metal alloys and dielectrics.

Electrical engineering uses of composites include dielectrics as in cermet resistors. Structural components in electrical systems are usually plastics, as are insulators and wire packaging[36]. Composite materials are expected to improve on many of the plastics now used in these applications[4, 36]. The important concept of a definite interface between two materials is analogous to the interface of a soldered joint on a board or thin film interconnections on chips[7-9, 32-34].

Polymer composites consist of a polymer matrix which is filled to a desired degree with another component to cause a major change in the properties of the material. Thus dyes added to a polymer would not create a composite material. The addition of 60% by volume of carbon fibres, having a drastic effect on the mechanical properties, would be considered a composite. When the additive is in the form of a fibre, as opposed to spherical or randomly shaped fillers, these composites are often referred to as FRP's, or fibre reinforced polymers/plastics.

Composite materials are designed to have properties superior to the individual components. Polymers are generally light in weight, but have relatively low strengths. Typical additives such as carbon or aramid fibres are very strong, but are also very brittle. The optimum combination of these properties is determined by the designer, who then creates a mixture of the two components in response to the desired result.

The ability to take advantage of the benefits of each component in a composite depends on the interface between them[5, 25]. A typical polymer composite has a stiff and brittle additive in a soft ductile matrix. If the interface itself is brittle, the material will not elongate easily and will not be capable of dissipating energy from environmental stresses. If the interface is very elastic, the stiffness of the filler will never influence the properties of the composite.

If the interface between the fibre and the matrix is critical to the performance of the composite, then environmental factors affecting the interface must be understood. Failure of composite materials is a complex matter, and usually occurs in a number of different modes. Failure of the interface is an important contributor[6].

In many applications, especially in the aerospace and automotive industries, materials undergo large temperature variations often many times a day. Different thermal expansion of the elements of composite materials cause interfacial stresses, and the cyclic stresses may cause degradation of material properties, leading to failure[6, 7, 34]. In applications where failure may cause property damage or loss of life it is necessary to understand and to design to avoid these failures.

In electrical engineering applications as previously mentioned, thermal fatigue at interfaces is analogous to the problem in composites. These interfaces can occur between soldered joints, the plastic-die interface of a plastic package chip, and between layers of multichip packages. Thermal fatigue in these cases is an important factor in the reliability of these devices[7-9, 32-34]. There is little information about thermal fatigue in heterojunction semiconductor devices, or if it will present a reliability problem.

1.3 Research Objectives

The study of thermal fatigue of polymer composites by ultrasonic NDT is the primary focus of this research. Ultrasonic NDT gives direct and indirect measurements of mechanical properties of materials, and as such is a useful tool to evaluate the changes in these properties.

The objectives of this work were to design and implement a system to study changes in ultrasonic velocity and attenuation in materials, and to evaluate the ability

of this system to assess these changes in composites as they undergo cyclic thermal fatigue. Experiments verifying the usefulness of this system were carried out and results are presented herein.

1.4 Thesis Outline

This thesis has been divided into six chapters. The present chapter is an introduction to the thesis topic. Theoretical background on sound propagation in solids is presented in the second chapter. Methods for ultrasonic NDT are presented in the third chapter, with emphasis on the method used in this experiment. In the fourth chapter the apparatus used is described in detail. Experimental results and their analysis are presented in Chapter 5, and the final chapter contains a summary of the work and discussions of directions for future research.

2. ULTRASOUND GENERATION AND PROPAGATION

2.1 Introduction

The principles of sound propagation in solids, with emphasis on how this understanding can be utilized in ultrasonic NDT, are reviewed in this chapter. The transfer of energy through solids by sound waves is governed by the same mathematical description as all wave propagation, including electromagnetic. It will be demonstrated how impedance boundaries and the actual propagation velocity of sound in a solid are related to important physical properties and are examinable through ultrasonic NDT.

The simplest solid is isotropic, homogeneous, and crystalline monatomic: a regular array of one type of atom. The "mass and spring" model of a crystalline solid is realised by replacing atoms with point masses linked by springs[2], as illustrated in Figure 2.1.

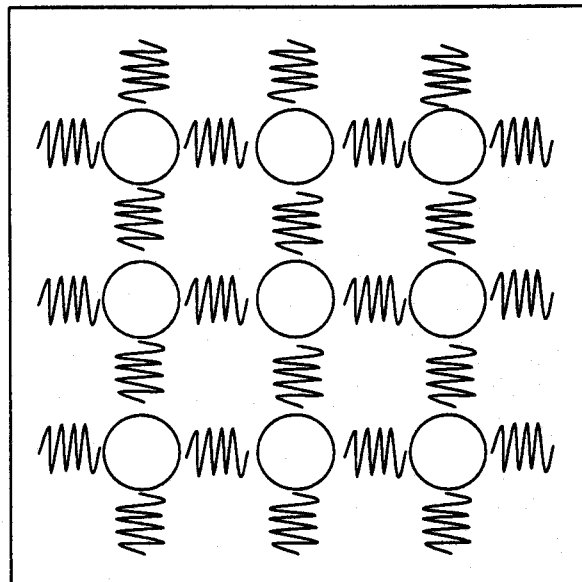


Fig. 2.1 Mass-spring model of crystalline structure.

At equilibrium, there will be small oscillations about a centre point due to thermal energy. If an external vibration is coupled to the system, it will be transmitted but modified by the masses and the interatomic forces.

As a material departs from the ideal solid, its transmission of mechanical energy changes as well. Any change in the crystal structure is a change in the impedance of the medium of the wave, with resultant reflections and refractions. This is one of two crucial reasons for the success of ultrasonic NDT. Flaws such as voids, inclusions, dislocations, and grain boundaries will all affect the transmission of sound energy in a solid, and can be examined through ultrasonic NDT. The mass-spring model is useful in visualizing these effects, as is shown in Figure 2.2.

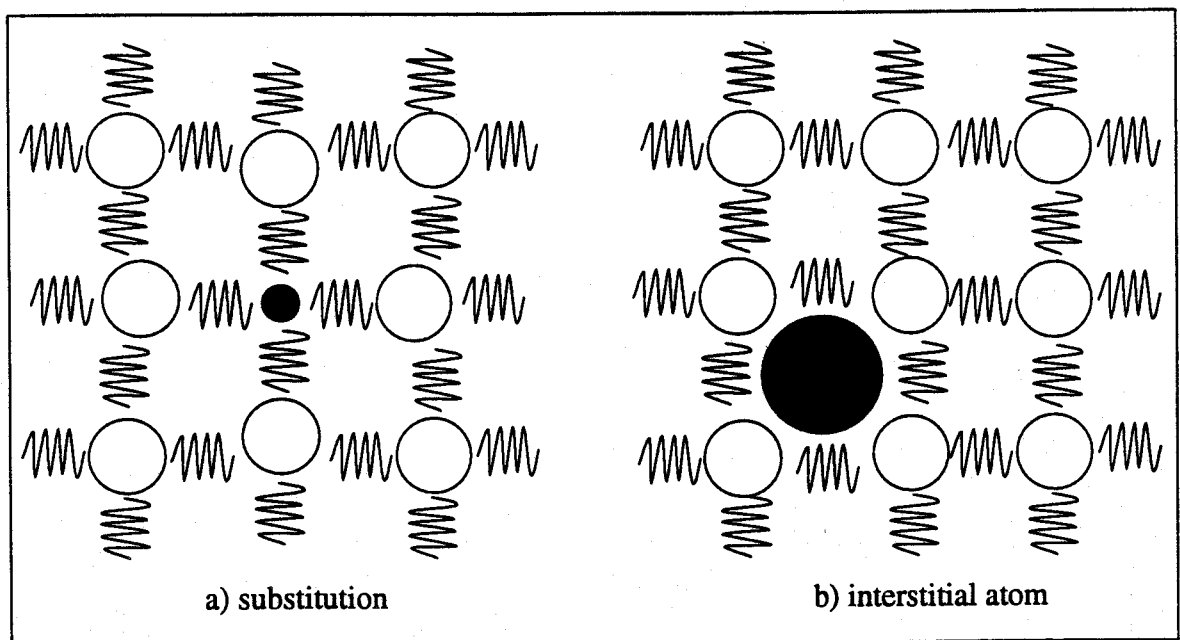


Fig. 2.2 Examples of crystal imperfections affecting wave propagation: a) substitution and b) interstitial atom.

The theory of wave propagation in solids will be presented for linear elastic

materials. This theory is valid for low strain amplitudes in many solids; including metals, semiconductors, and some polymeric materials under appropriate testing conditions[10]. The materials examined in this work were polymeric composites, which were assumed to be elastic[10, 11].

The following derivation for wave propagation in solids has been presented by Truell, Elbaum, and Chick [38].

Cartesian coordinates are used throughout this derivation. Boldface type indicates vectors (and tensors). Subscripts are used to refer to the Cartesian axes, and thus x_i implies the vector \mathbf{x} :

$$\mathbf{x} = x_i \mathbf{n}_i = x_1 \mathbf{n}_1 + x_2 \mathbf{n}_2 + x_3 \mathbf{n}_3 \quad (2.1)$$

where \mathbf{n}_1 , \mathbf{n}_2 , and \mathbf{n}_3 are unit vectors, and x_1 , x_2 , x_3 are the magnitudes of the components in these directions.

The spatial derivative, of the vector \mathbf{u} for example, is written in tensor notation as follows:

$$\nabla \mathbf{u} = \frac{\partial u_i}{\partial x_j} \equiv u_{i,j} \quad (2.2)$$

where the comma indicates the derivative with respect to the j index.

2.2 Hooke's Law

2.2.1 Stress Tensor

Consider a small cube of material inside a large solid. Forces on the surface of

the cube, due to the interaction with the bulk material, result in stresses in the cube. If ΔF_i is the force acting on the cube on the face in the i -th direction and ΔA is the area of that face (see Figure 2.3), the stress across that face is defined as:

$$\begin{aligned}\sigma_{(i)} &= \lim_{(\Delta A \rightarrow 0)} \frac{\Delta F}{\Delta A} \\ &= \sigma_{(i)j} n_j\end{aligned}\tag{2.3}$$

where n_j is the unit vector in the j -th direction. The parentheses around the subscript indicate that only one component is being considered. The complete stress tensor is the

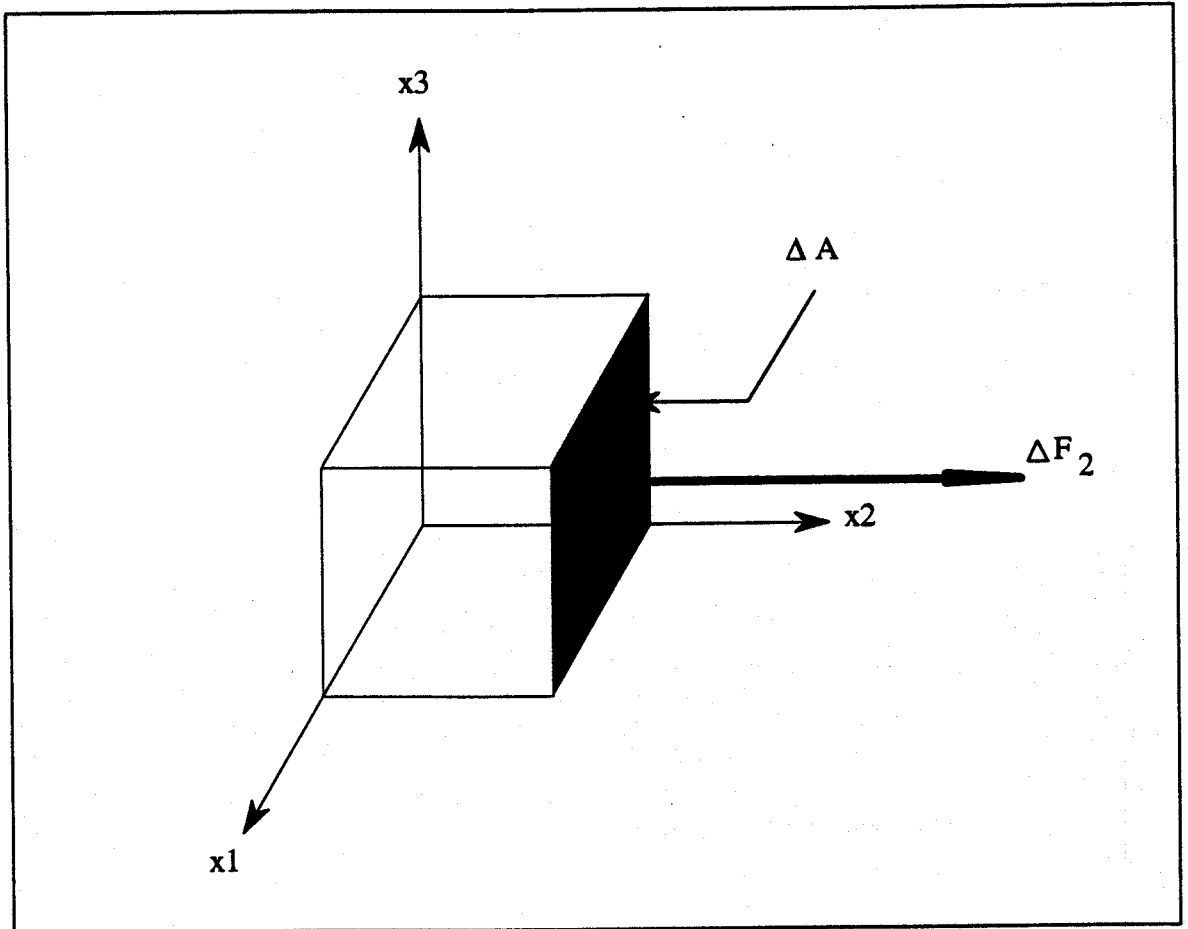


Fig. 2.3 Forces acting on the surface of a small cube of a solid.

sum of the component $\sigma_{(i)}$'s for all three directions: σ_{ij} .

2.2.2 Strain Tensor

Strain in a material is defined as a relative movement between different portions of a solid from their equilibrium position. It can be described in terms of the displacement vector $\mathbf{u}(x_i, t)$ for the solid as a whole. The displacement vector includes information about centre of mass translations and rotations, and the strain.

Consider two elemental volumes of material in a solid with equilibrium positions x_i and $x_i + dx_i$. At time t , after some displacement, the positions are:

$$\mathbf{x}(t) = x_i + \mathbf{u}(x_i, t) \quad (2.4)$$

$$\mathbf{x}(t) + d\mathbf{x}(t) = x_i + dx_i + \mathbf{u}(x_i + dx_i, t)$$

The change in the displacement between the two volumes is the sum of the centre of mass movement, the local strain, and the rotation about the centre of mass of the small volumes. This can be written as Δx_i , which can be shown to be:

$$\Delta x_i = \frac{\partial u_i}{\partial x_k} dx_k \quad (2.5)$$

The only important changes in displacement are those due to the actual deformation of the material. The strain tensor ϵ_{ij} is defined from:

$$\Delta x_i \text{ (deformation)} = \epsilon_{ij} dx_j \quad (2.6)$$

The strain tensor is given in terms of the displacement vector by:

$$\epsilon_{ij} = \frac{1}{2}(u_{i,j} + u_{j,i}) \quad (2.7)$$

It should be noted that the strain tensor is dimensionless.

2.2.3 Elastic Moduli

Stress is dependent on the strain, and for small strains (in the elastic region) relationship between the two can be approximated by expanding $\sigma_{ij}(\epsilon_{mn})$ in a Taylor series about zero, noting that $\sigma(0) = 0$: no strain means no stress. Hooke's Law results when only the first (non-zero) term is considered.

$$\begin{aligned} \sigma_{ij}(\epsilon) &= \sigma_{ij}(0) + \left. \frac{\partial \sigma_{ij}}{\partial \epsilon_{mn}} \right|_{\epsilon=0} \epsilon_{mn} + 0\epsilon^2 + \dots \\ &\approx \left. \frac{\partial \sigma_{ij}}{\partial \epsilon_{mn}} \right|_{\epsilon=0} \epsilon_{mn} \end{aligned} \quad (2.8)$$

The coefficients of ϵ_{mn} are the moduli of elasticity c_{ijmn} :

$$c_{ijmn} = \left. \frac{\partial \sigma_{ij}}{\partial \epsilon_{mn}} \right|_{\epsilon=0} \quad (2.9)$$

and Hooke's Law is now written as:

$$\sigma_{ij} = c_{ijkl} \epsilon_{kl} \quad (2.10)$$

The above equation implies that there are 81 coefficients which fully determine the stress-strain relationship for a material. Fortunately, this is not the case. Both the

stress and strain tensors are symmetric. This requires the following:

$$C_{ijmn} = C_{jimn} = C_{ijnm} \quad (2.11)$$

and it can be shown if the material is elastic, meaning strains are recovered when loading is removed, that:

$$C_{ijmn} = C_{mnij} \quad (2.12)$$

This reduces the number of independent coefficients to 21, and symmetries in the structure of the material will further reduce the number of coefficients required. For a fully isotropic material, the number of coefficients needed to describe the behaviour is two.

The elastic moduli have been defined from Hooke's Law as shown in Equation 2.8. However, traditional engineering materials have often been considered as isotropic, and more empirical definitions of elastic moduli are common. While most metals are crystalline, in bulk they are made up of many randomly oriented grains and over the dimensions of typical applications can be considered isotropic.

For isotropic materials, such as the aramid fibre in polyphenylene sulphide composite studied in this work, Young's modulus (E) is defined as the ratio of stress to strain for axial loading:

$$\sigma = E \epsilon \quad (2.13)$$

This neglects the induced stresses, which are related by Poisson's ratio ν .

Poisson's ratio is defined as the negative of the ratio of induced transverse strain to longitudinal strain:

$$\nu = -\frac{\epsilon_2}{\epsilon_1} = -\frac{\epsilon_3}{\epsilon_1} \quad (2.14)$$

where n_1 is the direction of applied stress. Hooke's Law can be written in terms of Young's modulus and Poisson's ratio as:

$$\sigma_{ik} = \frac{E}{1 + \nu} \left[\epsilon_{ik} + \frac{\nu}{1 - 2\nu} \sum_i \epsilon_i \delta_{ik} \right] \quad (2.15)$$

where δ_{ik} is the Kroneker delta defined by:

$$\begin{aligned} \delta_{ik} &= 1 \text{ for } i = k \\ &= 0 \text{ for } i \neq k \end{aligned} \quad (2.16)$$

2.3 Linear Elastic Wave Theory

By analyzing the equations of motion for solids, the speed of wave propagation can be related to the mechanical properties of the solid. Considering an isotropic solid under internal stresses, a small cube of the material at the position \mathbf{r} is subjected to the force \mathbf{F}_{net} :

$$\mathbf{F}_{\text{net}} = \rho(\mathbf{r}, t) a^3 \frac{\partial^2 \mathbf{u}}{\partial t^2} \quad (2.17)$$

where ρ is the density and a the side length of the cube, \mathbf{u} being the displacement vector used previously (see Figure 2.3). The net force across the cube faces perpendicular to \mathbf{n}_1 (the faces in x_2x_3 planes) is given by the product of the stress across the faces and the area of the faces:

$$F_{net} \mathbf{n}_1 = \frac{[\sigma_1(x_1 + a, x_2, x_3) - \sigma_1(x_1, x_2, x_3)]}{a} \cdot a \cdot a^2 \quad (2.18)$$

For very small a , the right hand side is the derivative of σ_1 with respect to x_1 , multiplied by the volume of the cube a^3 . Symmetrical expressions can be written in the other directions, and the net force is the sum:

$$\begin{aligned} F_{net} &= \rho a^3 \ddot{u}_i = \left(\frac{\partial \sigma_1}{\partial x_1} + \frac{\partial \sigma_2}{\partial x_2} + \frac{\partial \sigma_3}{\partial x_3} \right) a^3 \\ &= \frac{\partial \sigma_{ij}}{\partial x_j} a^3 = \sigma_{ij,j} a^3 \end{aligned} \quad (2.19)$$

Using Hooke's Law (Equation 2.10) and the definition of the strain tensor (Equation 2.7), the stress σ in the above equation can be replaced by the displacement vector \mathbf{u} :

$$\begin{aligned} \rho \ddot{u}_i &= \frac{\partial}{\partial x_j} (c_{ijkl} \varepsilon_{kl}) \\ &= \frac{1}{2} c_{ijkl} \frac{\partial}{\partial x_j} \left(\frac{\partial u_k}{\partial x_l} + \frac{\partial u_l}{\partial x_k} \right) \end{aligned} \quad (2.20)$$

Using the fact that $c_{ijkl} = c_{ijlk}$, it is now possible to write the equations of motion for any solid:

$$\rho \ddot{u}_i = c_{ijkl} u_{l, kj} \quad (2.21)$$

$$u_{l, kj} = \frac{\rho}{c_{ijkl}} \ddot{u}_i$$

The propagation velocity in the medium can be found by considering a plane wave solution to Equation 2.21. The displacement vector \mathbf{u} is written as:

$$\mathbf{u} = u_l = U_l e^{i(\omega t - \mathbf{k} \cdot \mathbf{r})} \quad (2.22)$$

where U_l is the amplitude, \mathbf{k} is the wave vector, and \mathbf{r} the position vector. In an elastic medium, \mathbf{k} is simply given by:

$$\mathbf{k} = \frac{\omega}{\mathbf{v}} \quad (2.23)$$

When the plane wave solution of Equation 2.22 is substituted into Equation 2.21, the relationship between the speed of propagation of sound waves in a solid to the elastic moduli of the solid is found:

$$v_{ij} = \sqrt{\frac{c_{ijkl}}{\rho}} \quad (2.24)$$

It is relatively simple to measure the speed of waves in a solid, and to measure changes in the speed due to changing microstructural variables. This yields a powerful tool for the analysis of the mechanical properties of a material and the changes in these properties due to such factors as fatigue loading.

2.3.1 Characteristic Acoustic Impedance

The characteristic acoustic impedance of materials is an important property for ultrasonic testing. Reflections at impedance boundaries are used for many testing methods, and for bonding transducers to specimens reflections must be minimized. The characteristic impedance Z of a material can be defined as the ratio of acoustic pressure σ_A to particle velocity [15, 39], as given by the time derivative of the displacement vector \mathbf{u} . This is directly analogous to the ratio of electric potential to current in defining an electrical impedance.

$$Z \equiv \frac{\sigma_A}{\dot{u}_k} \quad (2.25)$$

Consider a plane longitudinal wave travelling in a medium of density ρ with elastic moduli c_{ijkl} . The change in displacement Δx_i at time t between two points in the medium due to the wave is given by Equation 2.5, repeated here:

$$\Delta x_i = \frac{\partial u_i}{\partial x_j} dx_j$$

The strain ϵ_A caused by the wave is then simply $u_{i,j}$. The acoustic pressure σ_A can be expressed in terms of the elastic moduli and the displacement vector using Equations 2.10 and 2.22. Positive acoustic pressure results in compression, which is why there is a negative sign in Equation 2.26.

$$\sigma_A = -c_{ijkl} \epsilon_A = -c_{ijkl} \cdot -\frac{i\omega}{v} u_k \quad (2.26)$$

The characteristic impedance can now be found using Equations 2.26 and 2.22.

$$Z = \frac{\sigma_A}{\dot{u}_k} = \frac{c_{ijkl} \frac{i\omega}{v_{kl}} u_k}{i\omega u_k} = \frac{c_{ijkl}}{v_{kl}} \quad (2.27)$$

Note that for a plane wave in an elastic or non-dispersive medium, the characteristic impedance is real. The more familiar result for a homogeneous, isotropic medium is found from Equations 2.27 and 2.24.

$$Z = \rho v \quad (2.28)$$

2.4 Ultrasonic Velocity

For an isotropic material, the only distinctions to be made between velocities is whether the wave is longitudinal or transverse. For a longitudinal wave in an isotropic material, the propagation velocity is given by:

$$v_x = \sqrt{\frac{c_{xx}}{\rho}} = \sqrt{\frac{E}{\rho} \frac{1 - \nu}{(1 + \nu)(1 - 2\nu)}} \quad (2.29)$$

The subscripts xx refer to the fact that particle oscillation is in the propagation direction. Equation 2.29 also relates the common engineering parameters Young's modulus E and Poisson's ratio ν to the velocity, from Equations 2.14 and 2.23.

For the anisotropic materials studied in this work, Young's modulus and Poisson's ratio are dependent on direction. The elastic moduli c_{ijkl} are routinely used to

describe the mechanical properties of these materials, rather than a Young's modulus.

Poisson's ratios can be determined through measurements of the elastic moduli.

To analyze the uniaxial fibre composites, the fibre direction is chosen as the primary axis x_1 . The choice of the other axes is arbitrary. Measurements of longitudinal velocity were performed along the fibre axis and perpendicular to the fibre axis. A contracted notation is used to write equations for stress-strain, following standard usage, where pairs of indices are replaced by a single index (see Table 2.1).

Table 2.1 Equivalent indices for contracted notation.

tensor notation	11 22 33	23, 32	13, 31	12, 21
matrix notation	1 2 3	4	5	6

Hooke's law is now written as:

$$\sigma_i = c_{ij} \varepsilon_j \quad (2.30)$$

For the problem of the transversely isotropic composites, the elastic coefficients are reduced by symmetry to:

$$c_{ij} = \begin{vmatrix} c_{11} & c_{12} & c_{12} & 0 & 0 & 0 \\ c_{12} & c_{22} & c_{23} & 0 & 0 & 0 \\ c_{12} & c_{23} & c_{22} & 0 & 0 & 0 \\ 0 & 0 & 0 & c_{44} & 0 & 0 \\ 0 & 0 & 0 & 0 & c_{44} & 0 \\ 0 & 0 & 0 & 0 & 0 & c_{66} \end{vmatrix} \quad (2.32)$$

Thus the velocities measured along the fibre axis are given by:

$$v_1 = \sqrt{\frac{c_{11}}{\rho}} \quad (2.33)$$

and perpendicular to the fibre axis direction by:

$$v_2 = \sqrt{\frac{c_{22}}{\rho}} \quad (2.34)$$

2.5 Ultrasonic Attenuation

There are many mechanisms for the attenuation of ultrasound in materials. The most important are physical defects in the material which cause scattering. Actual absorption may not be a major factor. Scattering will occur at any change in material within a solid, such as grain boundaries, dislocations, and air voids. These result in changes in material impedance (see Equation 2.27). The magnitude of this scattering will depend on the comparative size of the wavelength and the defect, and the difference in impedance of the regions.

An attenuation coefficient α can be defined by [12, 37]:

$$P = P_0 e^{-\alpha L} \quad (2.35)$$

where P_0 is the sound pressure at an arbitrary reference point, and P is the pressure at a point a distance L from reference. Experimentally determined attenuation is affected by a number of external factors, which will be discussed in greater detail in Chapter 3.

Composite materials are in general very highly attenuating due to the existence of physical discontinuities of a relatively large size. Boundary layers provide surfaces for scattering energy away from the propagation direction. Absorption in the matrix material may also be important, depending on the particular material and the physical structure.

Other mechanisms of attenuation do not depend on the material, but the geometry. Diffraction and interference from internal reflections can also be major contributors to measured attenuation.

2.6 Ultrasonic Waves

Ultrasonic waves are usually defined as any (sound) wave with a frequency greater than 20kHz, which is about the limit of human hearing. Gases can support only longitudinal (compressional) waves, which are what we hear as sound. Liquids allow propagation of longitudinal and surface waves, and solids can support longitudinal, shear, and surface waves.

Particle motion of longitudinal waves is in the direction of wave propagation. Shear waves have particle oscillation perpendicular to the direction of propagation, similar to electromagnetic waves. Note that this means there are two possible shear waves for any direction of propagation.

There is almost an infinite variety of surface waves that are possible in solids, because they are dependent on the actual shape of the specimen. The two types of

surface waves most commonly used in NDT are Rayleigh waves (see Figure 2.4) and Lamb waves. There is very little oscillation at depths greater than one wavelength into the material.

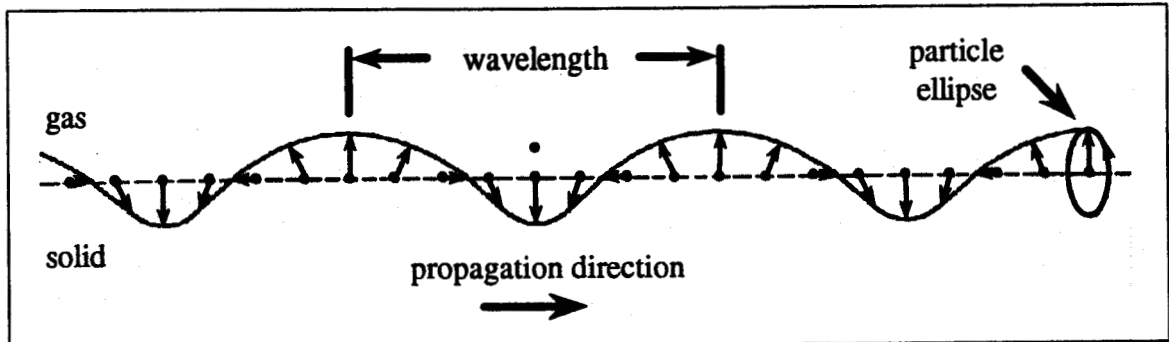


Fig. 2.4 Showing motion of top layer of particles for Rayleigh waves, with oscillation ellipse on right. (After Krautkramer and Krautkramer[2].)

At an interface between two different media, mode conversion can take place. This makes it possible to excite surface, shear, and longitudinal waves from incident shear or longitudinal waves at appropriate angles, according to Snell's Law. Remembering that liquids do not support shear waves, this property is very important. Many industrial testing facilities use water as a medium between the transducer and the specimen. This allows easy changing of specimens without adjusting the test equipment, and removes any air gap between the specimen and the transducers.

2.7 Wave Excitation

The excitation of ultrasonic waves in a material is usually accomplished with piezoelectrics. They act as transducers, converting electrical energy to mechanical energy. Commonly used transducer materials are quartz, barium titanate (BaTiO_3), and

lead zirconate titanate or PZT. The measurements herein utilized PZT transducers.

2.7.1 Piezoelectricity

Piezoelectricity is generally defined as any phenomenon which couples electrical and mechanical behaviour in materials[13]. The *piezoelectric effect* is defined as the production of a net polarization in a material due to externally applied mechanical deformation. The effect is a result of non-centre symmetric crystal structures in ionic solids (see Figure 2.5). Few natural crystals exhibit a strong enough effect to be useful. Quartz is the most commonly used natural piezoelectric material.

The *inverse piezoelectric effect* is the more utilized property. This is defined as mechanical deformation in response to an externally applied field. In reality, any dielectric will expand somewhat in an electric field, as this changes the dielectric constant and lowers the system energy. This weak effect is proportional to the square of the applied electric field. The structure of piezoelectrics is much more sensitive to external fields, and the deformation is directly proportional to the applied field.

The equations defining piezoelectricity are Hooke's law and the relation between electric polarization P and electric field E . In general, assuming a linear coupling of electric and mechanical properties, they are[16]:

$$\epsilon_i = \sum_{j=1}^6 s_{ij} \sigma_j + \sum_{j=1}^3 d_{ij} E_j \quad P_i = \sum_{j=1}^6 d_{ij} \epsilon_j + \sum_{j=1}^3 \zeta_{ij} E_j \quad (2.36)$$

for piezoelectric strain constants d_{ij} and dielectric permittivity ζ_{ij} . The coefficients s_{ij} are the inverse of the elastic coefficients c_{ij} .

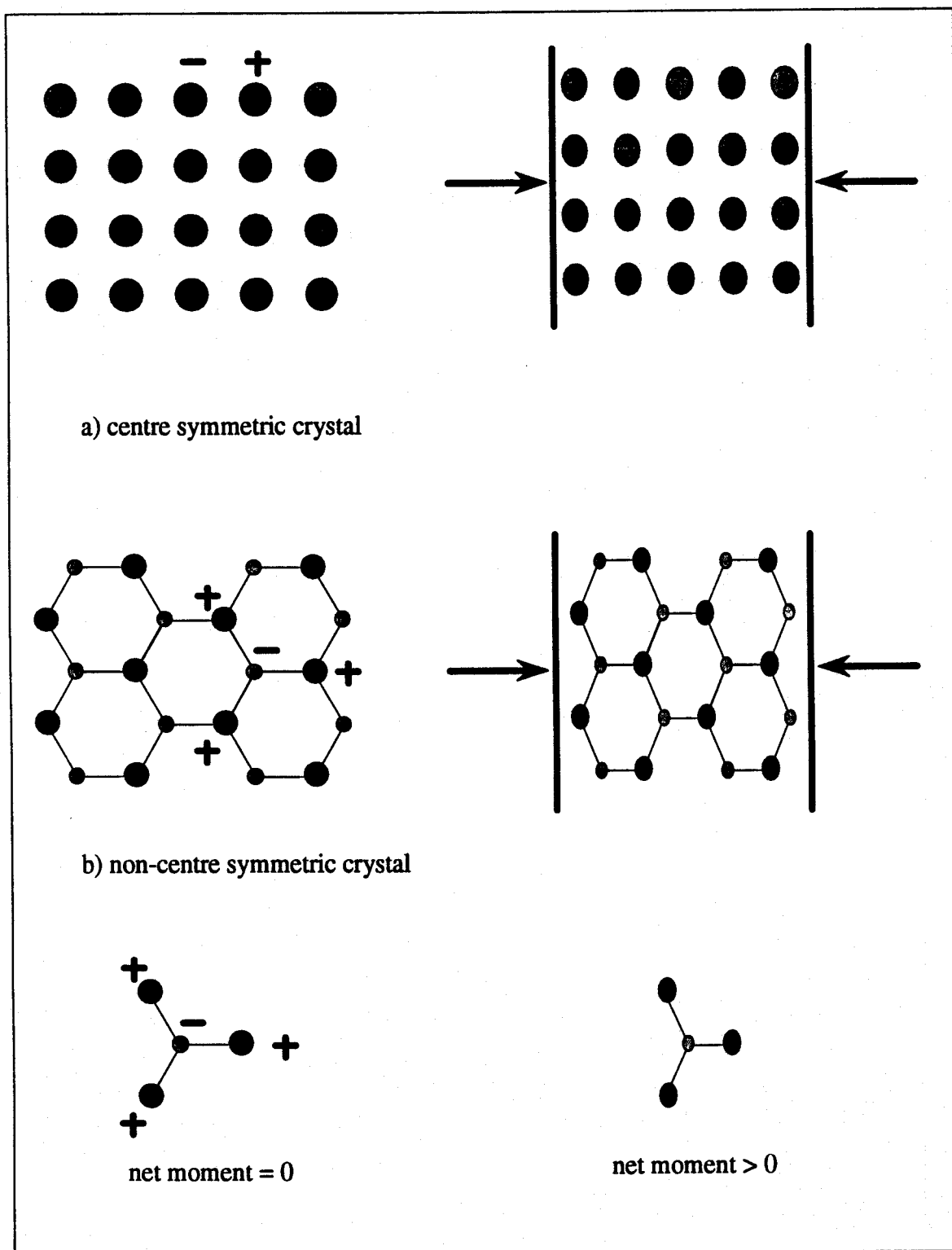


Fig. 2.5 Comparison of centre symmetric structure to non-centre symmetric. (after Beam [16]).

Piezoelectrics are used in many electronic timing devices, from watches to computers, and are used in ultrasonic NDT to convert electric impulses into mechanical waves (and vice versa). It is important to note that because the effect is due to the crystal structure, different directions of strain will produce different directions and magnitudes of polarization. The off-axis components of the tensors c_{ij} and ζ_{ij} are non-zero, meaning there will be for example shear stress in the yz plane due to an electric field in the x direction.

Knowledge of the elastic moduli and the piezoelectric strain constants enables the design of transducers operating in (mainly) shear or longitudinal modes. Crystals are cut so that the strains in undesired directions are kept to a minimum.

2.7.2 Ferroelectricity

Ferroelectricity is only of interest in this work in that many transducers used in ultrasonic NDE are ferroelectrics. For these purposes, ferroelectrics are defined as materials which exist as polarized ionic crystals below a certain temperature called the Curie temperature and denoted T_c . They are **not** ferrous, but are dielectrics; the name being derived from the similarity to ferromagnetism.

Ferroelectric crystals are naturally randomly oriented, but can be preferentially aligned by annealing in a strong external electric field. This results in a strong piezoelectric effect in the desired direction. The ferroelectric materials are generally more efficient in converting electrical energy to mechanical energy than quartz, but are

less stable than quartz and can not be operated at temperatures higher than T_C , which for $BaTiO_3$ is 120C compared to an upper limit of 550C for quartz. Some properties of different transducer materials are shown in Table 2.2.

Table 2.2 A comparison of different piezoelectric materials (from [15] except for * from manufacturer's specifications).

material	relative permittivity	piezoelectric coefficient d_{11} ($10^{-12}C/N$)	Curie temperature (C)
quartz (x cut)	4.5	2.3	550
PZT*	1730	374	365
barium titanate	400-1700	60-190	120

2.7.3 Piezoelectric Transducers

Piezoelectric transducers are very common in ultrasonic NDE for a number of reasons. Piezoelectrics have been extensively studied and used, which means that there is a good library of knowledge about their performance. The function of the transducer is to convert electrical energy into sound energy and the reverse. To design electrical circuitry to excite and receive these signals, it is instructive to look at an equivalent circuit model of the transducer as shown in Figure 2.6.

The voltage V across the transducer is modeled as being V across the capacitance C_0 of the piezoelectric material between the electrodes, in parallel with the

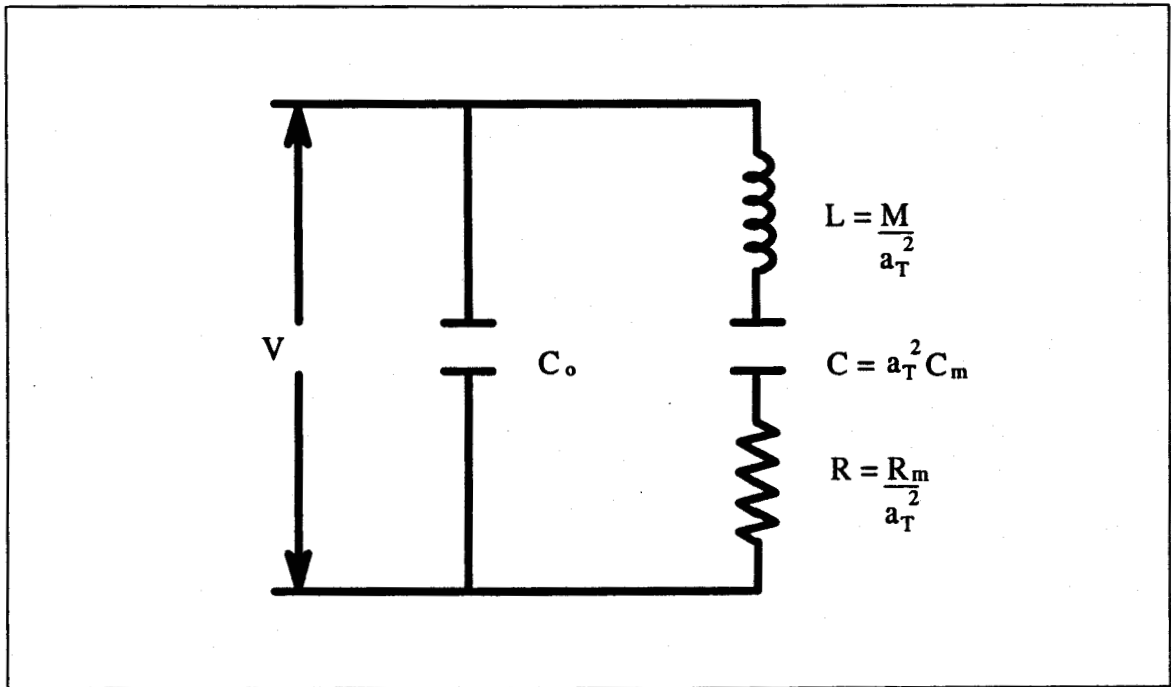


Fig. 2.6 Equivalent electrical circuit for a piezoelectric transformer at resonance (after Blitz [15]).

mechanical branch. The mechanical branch is represented by an inertial element or the mass M , an energy storage element C_m , and a loss R_m . These are related to the electrical equivalents by the transformation factor, a_T . This is a constant for any one transducer, and is defined from[15]:

$$i = \frac{Ae}{t} v = a_T v \quad (2.37)$$

where i is the instantaneous current across the transducer, e the charge of an electron, A is the area of the face, t the thickness of the transducer, and v the velocity of one face relative to the other. Thus a_T relates the charge movement to the physical deformation.

The coupling between the mechanical components and electrical components of

the transducers can create a very complex system, and the above model is very limited in quantitative work. However, piezoelectrics tend to have sharp resonances, and are generally operated at or near their resonant frequencies. For longitudinal waves, the fundamental mechanical resonance frequency f_r occurs when the crystal thickness is half of the wavelength:

$$f_r = \frac{v}{2t} \quad (2.38)$$

where v is the speed of sound in the crystal, and t is the thickness of the crystal in the direction of oscillation. Excitation at odd multiples can be used, but even harmonics result in no net change in thickness, and thus do not propagate.

There are many different factors to be considered when choosing a frequency to operate at. Obviously the crystal becomes thinner and more fragile as the frequency increases. It is possible to excite crystals at odd harmonics, but the efficiency decreases. The types of materials to be evaluated must be considered, as the frequency response of the specimen may make it desirable to operate at frequencies which are less attenuating, giving a stronger output signal and therefore a better signal to noise ratio. Higher frequencies are necessarily more sensitive to inhomogeneities in the material being examined.

The choice of the transducer material is also important. As can be seen from Table 2.2, quartz has a much lower permittivity than the other materials. This means that it requires much less current. However, it is not as efficient in converting charge

separation into physical deformation as PZT, for example[14]. Quartz transducers generally have a much higher quality factor, as they are much more regularly crystalline than polarized ferroelectrics. This restricts the useable bandwidth. Matec Penetran (PZT) transducers, with a nominal 4MHz resonance, were chosen for this work.

A significant problem with piezoelectric transducers is the requirement for contact with the specimen. As at any impedance boundary, there will be some reflection of wave energy at the crystal-specimen interface. If the crystal is not firmly bonded to the specimen surface, this reflection dramatically increases. Any kind of air gap will dramatically reduce transmitted sound energy, as the impedance change between air and most solids is drastic. Much work has been done on the proper bonding of transducer to specimen to ensure that enough energy is transmitted to the specimen, and that reflected energy to the crystal is not strong enough to severely distort the excitation.

The simplest solution to the bonding problem is to glue the crystal on the specimen surface. However, it is usually desirable to examine many specimens with the same experimental parameters, and the exchange of specimens should not require a great deal of effort. The most common solution is to immerse the specimen in a water bath, using water as a medium or couplant between the transducer and the specimen. This will be adequate for many applications. The technique used in these measurements is described in Section 4.1.2.

Piezoelectric transducers offer a range of physical sizes and frequency ranges

from kilohertz to hundreds of megahertz. They can be sharply resonant or broadband, depending mostly on crystal material. They are relatively cheap, and have been in use long enough for there to be a large amount of information available about their performance. The main drawback with the use of piezoelectrics instead of other types of transducers is the requirement for contact with the specimen.

Some kind of electrical pulse is applied to the transducer to generate a mechanical wave in the specimen, depending on the application. If the response of the crystal is known, the characteristics of the wave in the material can be found. For most applications, only the velocity and the attenuation of the wave are important and the exact wave in the specimen need not be determined. This is very important as the frequency response of the boundary layers, the transducers, and the external electronics is very difficult to quantify.

3. ULTRASONIC MEASUREMENT TECHNIQUES

3.1 Introduction

The purpose of the measurements undertaken in this work was to examine *changes* in ultrasonic velocity and attenuation in certain fibre composites undergoing thermal fatigue. A modified "sing-around" measurement technique was successfully applied. Some absolute measurements were also performed using the sing-around technique.

In addition to the ultrasound measurements, scanning electron microscopy (SEM) was used as a qualitative tool to provide additional information on the physical modes of fatigue damage in the composites.

3.2 The Sing-Around Technique

The sing-around technique is a through transmission technique for making ultrasound measurements that is basic to almost all ultrasonic measurement systems[17]. It is very simple to use and requires minimal external circuitry to implement.

Two transducers are used for this method, one transmitter and one receiver. The transmitter is excited by a pulse generator, at time intervals determined by the arrival of the previous pulse at the receiver. Therefore the time interval between excitations (the pulse repetition rate) matches the transit time through the sample. A frequency counter can be used to count the pulse repetition rate, and neglecting any

delays in the electronics, the velocity through the sample is given by:

$$v_1 = \text{path length} \times \text{pulse repetition rate} \quad (3.1)$$

Figure 3.1 demonstrates how this technique can be realized.

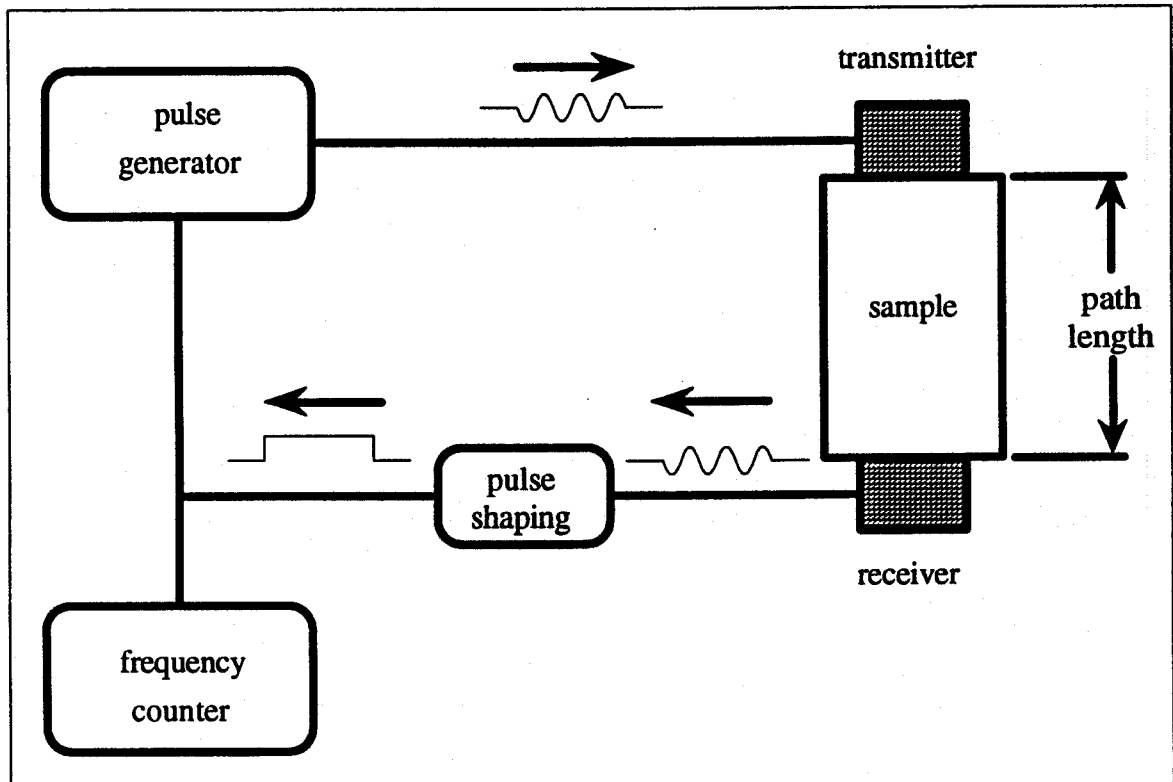


Fig. 3.1 A functional block diagram of the sing-around technique for ultrasonic velocity measurement.

The sing-around method is the basis of the measurements made in this work, but some modifications were made to the above system. The retriggering of the pulse generator as shown above must be accomplished by choosing some voltage level for the output to reach. For a more accurate and flexible system, the pulse repetition rate was set externally and the transit time between two peaks was measured on an oscilloscope. The peaks were the first peak of the excitation voltage waveform and the

first peak of the received. This was possible to measure to a precision of a few nanoseconds, and avoids triggering problems.

Attenuation measurements were also performed from an oscilloscope. The peak to peak voltages of the excitation pulse and the received pulse were measured directly.

3.2.1 Absolute Velocity

The excitation used when measuring velocity is a chopped sine wave, and therefore is actually made up of many frequency components, which are not all propagated the same way. If the material is truly elastic, the wave will not change shape in the specimen. The transducers, unfortunately, will not be perfectly damped, and this will change the shape of the wave somewhat.

Geometric factors influence measurement accuracy, as the faces of the specimen should be parallel and the wave incident at 0° for the measurement of path length to correspond to the actual path length. It was also found in these experiments that the bond layer introduced an error in the measurement of absolute velocity. The transit time measurements showed a strong frequency dependence, which was determined to be due to the bond effects (see Chapter 5).

It is apparent that accurate measurements of the absolute velocity are difficult to carry out. It is possible to obtain accuracies of better than 5% with the sum of the errors in transit time and path length. These measurements were performed for each material examined herein, and results are presented in Chapter 5.

3.2.2 Absolute Attenuation

Attenuation measurements are made by comparing signal amplitudes before and after passing through the sample. It must be recognized that the waves are attenuated by a combination of factors, which include attenuation in the material and geometric factors, such as reflections and diffraction. Parallel surfaces are important for path length considerations. Surface roughness will increase reflection at the interfaces. The reflections at the bonds must also be accounted for. To measure an attenuation coefficient α as defined in Section 2.2.3, the geometric factors must be removed. Measurements of attenuation in the experimental materials are presented in Chapter 5.

3.3 Other Ultrasonic NDT Techniques

The most common technique for ultrasonic NDT is the pulse-echo method. One transducer is used as a transmitter and receiver. The transducer is externally excited with a pulse repetition rate slow enough not to interfere with echoes from the sample. An oscilloscope display will then show the excitation, followed by echoes. This allows measurement of the transit time and attenuation in the specimen. Most industrial uses of ultrasonic NDT are in flaw detection, and the data are processed to reveal location and size of flaws in the sample as indicated by changes in magnitude and time of the echoes.

The crucial disadvantage of the pulse-echo technique is that the path length for the wave is twice as long as for a through-transmission technique like sing-around. For

very highly attenuating materials such as composites, this restricts the sample sizes that can be used. The large difference in amplitude between the excitation and the echo also requires bridging circuitry to isolate the echo to examine it on an oscilloscope. For the work presented here, it was felt that the benefits of the pulse-echo method were not sufficient to warrant the time and expense to implement it.

Newer techniques for ultrasonic NDT have been implemented, mostly aimed towards improving absolute measurements and allowing for automation of the measurement process. Again the benefits of these methods were not very great for the type of measurements carried out here, but the most popular will be discussed below. It should be noted that all of these methods require some basic components: a transmitter and a receiver (which may be the same transducer), signal generation and amplification, an oscilloscope to display waveforms from the transducers, and timing circuitry. Through transmission methods are the simplest to implement.

The pulse superposition technique, originated by McSkimin[18], adjusts the pulse repetition rate so that the excitation is superposed on an echo of a previous excitation. The experimenter chooses for example the second echo, and adjusts the pulse repetition rate until the echoes are in phase. When this condition is reached, the inverse of the pulse repetition rate gives the time between the excitation and the second echo for this example. The benefit of this method is that transit time measurement errors due to coupling are eliminated. Precision is about 1 in 10^6 , but some corrections must be done to get absolute velocities. Automation of the measurements is possible.

The pulse-echo-overlap (PEO) method for velocity measurements was originated by May, and refined by Papadakis[19]. It is somewhat similar to the pulse superposition technique, in that the triggering of the oscilloscope used to view the waveforms is varied until two echoes are overlapped. The triggering time then gives the transit time. This method is very accurate, but requires a complex apparatus and is a time consuming measurement. Automation would be very difficult.

A recent improved method for velocity measurements is the superposed pulse-echo-overlap method implemented by Negita and Takao[20]. Again it is based on changing triggering times to overlap echoes on the oscilloscope. It is simpler to implement than the PEO method, and precision is claimed to be 0.1nsec in round trip time.

As shown above, it is possible to implement measurement systems to very precisely measure ultrasonic velocity. With any of these systems, it would also be possible to make attenuation measurements by simply measuring amplitudes of successive echoes. For the composite materials examined in this work, attenuation in the specimens was very high, and the pulse-echo methods therefore become difficult if not impossible to implement, as very few echoes are of useful magnitude. The value of absolute velocity measurements is also somewhat doubtful, as the aim of the experiment was to examine changes in the materials.

3.4 Scanning Electron Microscopy

Specimens were examined before and after fatigue testing using scanning electron microscopy (SEM) to act as a qualitative indicator of mechanical damage caused by fatigue loading. It was felt that some of the mechanisms of fatigue damage would be visible. The expected failure mode due to fatigue is degradation of the fibre-matrix interface, and it was possible to visually examine individual fibres in the specimens for defects in the bonding. Comparisons of fatigued to unfatigued specimens are displayed in Chapter 5.

4. EXPERIMENTAL APPARATUS AND PROCEDURES

4.1 Experimental Apparatus

A modification of the sing-around ultrasonic measurement technique was used to measure ultrasonic velocity and attenuation. Figure 4.1 is a comprehensive block diagram of the system implemented for this work. Commercial laboratory equipment was utilized wherever possible.

The following Sections 4.1.1 to 4.1.4 describe different elements of the test system in detail. Most of the components were available in house, except the

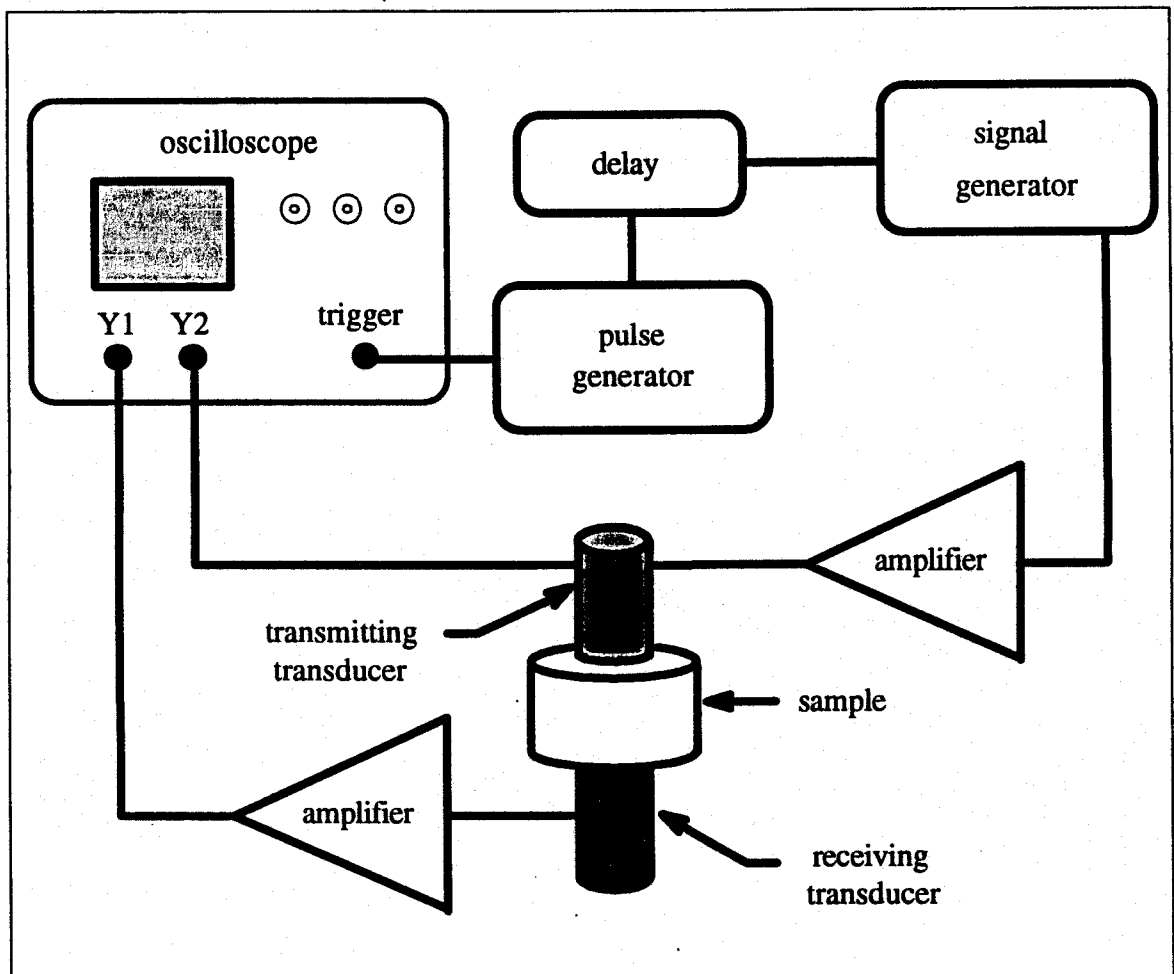


Fig. 4.1 Block diagram of system used in this study.

amplifiers which were built for this experiment and the transducers.

4.1.1 Circuit Timing and Triggering

The triggering or the pulse repetition rate is controlled by a pulse generator (Advance Instruments Pulse Generator PG58), which directly triggers the oscilloscope (Tektronix 2465A). A variable delay (Interstate Electronics Pulse Generator P25) is placed between the pulse generator and a signal generator (Wavetek Sweep Generator

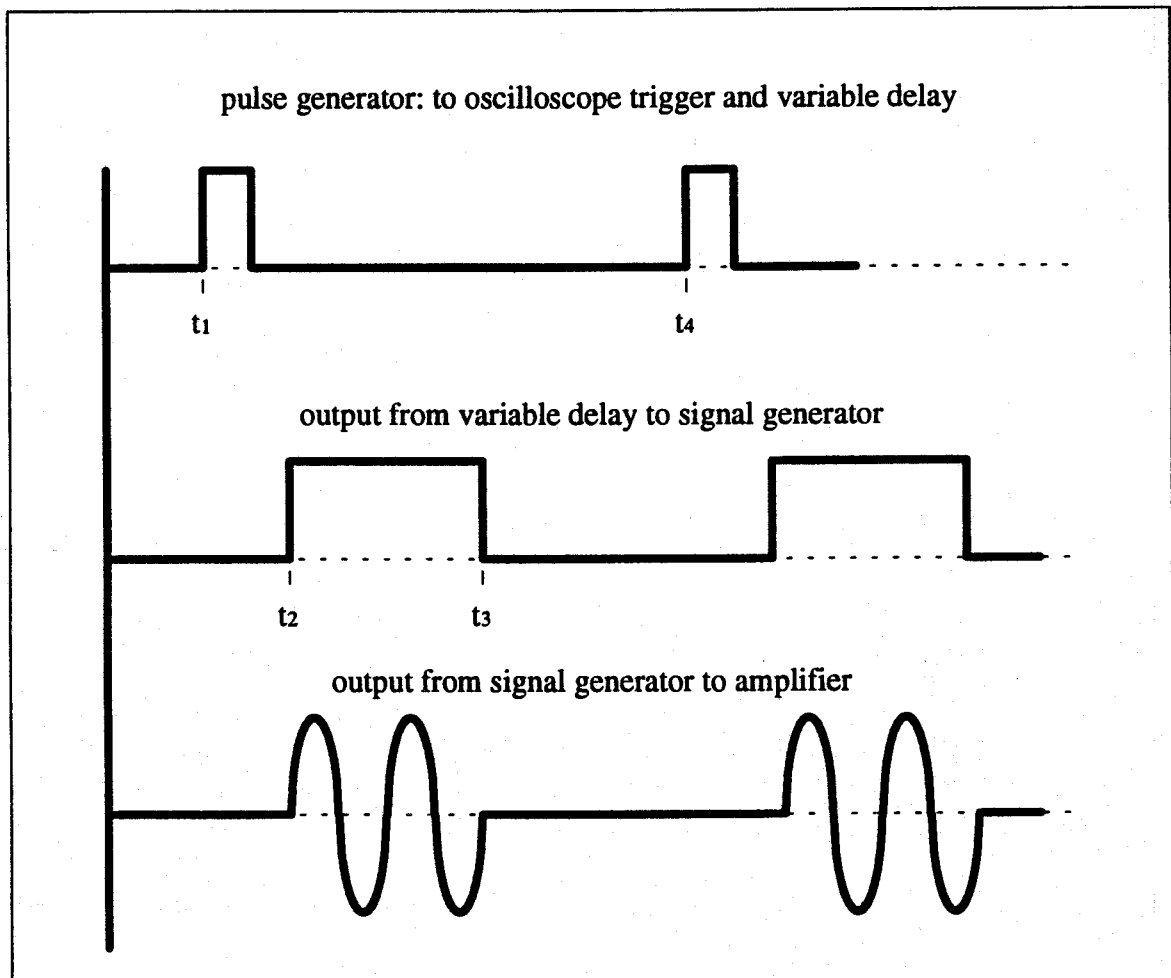


Fig. 4.2 Timing for the modified sing-around apparatus.

model 185). This allows the experimenter to start the oscilloscope sweep before the beginning of the excitation, and therefore view the entire waveform.

From the variable delay unit a rectangular pulse of adjustable width is sent to the signal generator, which is operated in gated mode. This results in a number of wavelengths of a sine wave of the desired frequency being sent through the amplifier to the transmitting transducer. The timing is shown graphically in Figure 4.2. The pulse repetition rate is given by the inverse of (t_4-t_1) . The pulse width input to the amplifier is given by the integer number of periods just under (t_3-t_2) . The delay from the beginning of the oscilloscope sweep to the start of the excitation is (t_2-t_1) . All of these timings can be varied by the experimenter.

4.1.2 Transducers

The transducers used for the measurements were Matec Penetran longitudinal wave PZT transducers with a nominal resonance frequency of 4MHz. These transducers were chosen because of the good performance of PZT (see Section 2.4 and Table 2.1). They also have a protective workface and a damped backface, with a BNC connector on the transducer. This makes them easy to use and less fragile than a simple crystal without casing.

PZT transducers have much larger bandwidth than quartz crystals, due to the imperfect alignment of the polarized molecules (see Section 2.5). A 4MHz quartz crystal at this laboratory was found to have a half power bandwidth of about 50kHz,

while the 4MHz PZT transducers used in these experiments had about a 2MHz half power bandwidth. This allows measurements over a much greater frequency range.

A critical factor in the measurements is the bond between the transducers and the specimens. To ensure maximum transmission through the sample, the bond line must be acoustically matched. In practice, this means there must be no air gap, as the acoustical impedance of air is about a factor of 10^4 smaller than most solids, and can be considered to be vacuum for any gap much larger than the wavelength used[2].

Air gaps in commercial ultrasonic testing are usually eliminated by immersing specimens in a tank of water, with the transducers bonded to the sides of the tank, in a permanent or semi-permanent fashion. The drawbacks of this method are high power requirements to overcome loss in the water, and restrictions on specimens that are sensitive to moisture, such as polymers.

Because of the additional expense and complications of using immersion in water for bonding, dry testing was used in these measurements. Liquid honey was used to wet the surfaces of the specimen-transducer interfaces, on the advice of the transducer manufacturer.

The transducers were clamped to separate stands which were mounted on an optical bench to provide stable support. The transducers were mounted vertically, with the bottom transducer fixed and the top transducer allowed to move vertically (see Figure 4.3). Before specimens were mounted, the transducer faces and the specimen faces were lightly coated with honey. The top transducer was then lowered onto the specimen.

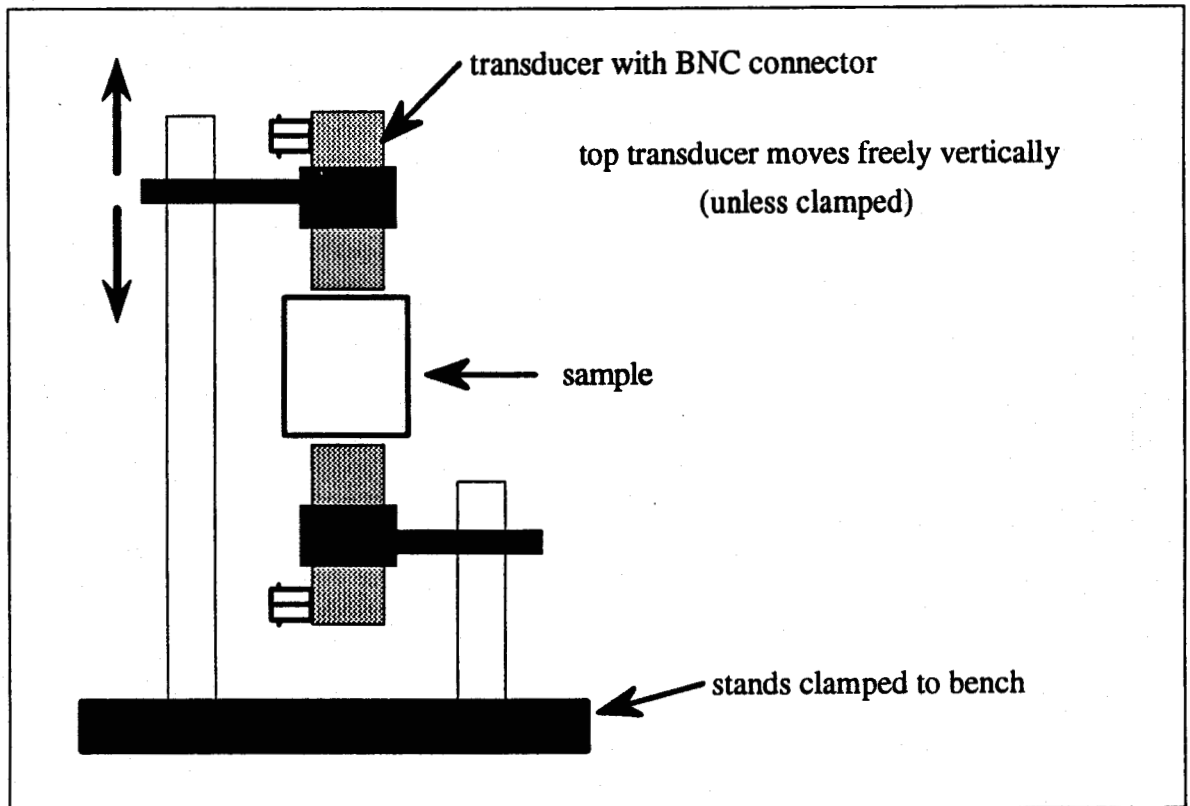


Fig. 4.3 Transducer and specimen mounting arrangement.

To get maximum transmission through the sample, the faces must as close to parallel as possible, with a minimal gap. This was achieved by rotating the specimen until the maximum received signal amplitude was observed on the oscilloscope. When this was found, the top transducer was fixed in position by tightening a screw. The force on the sample was that due to the mass of the transducer and the sliding assembly (about 100g).

4.1.3 Signal Amplification

Two amplifiers were used for these measurements: one before the transmitter

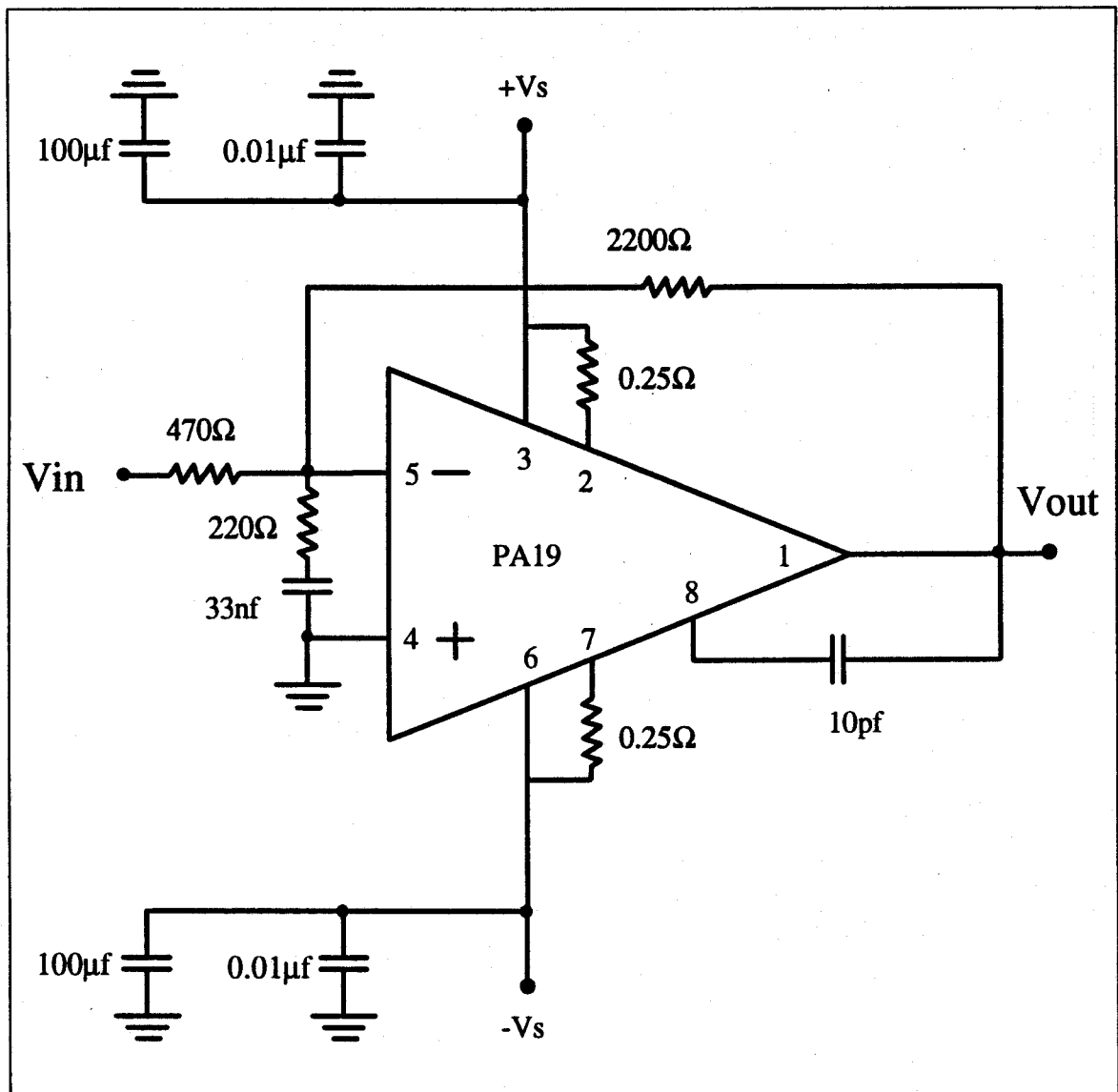


Fig. 4.4 Implementation of the PA19 power amplifier.

and another after the receiver. The transmitter amplifier was a simple inverting amplifier based on the Apex PA19 power amplifier (see Figure 4.4). The circuit was mounted on a heatsink in a chassis with a cooling fan.

The transducers chosen for this work are PZT, which has very high current requirements, having a much larger dielectric constant than quartz (see Table 2.1). An equivalent circuit of a transducer is given in Figure 2.5. An estimate of the transducer

impedance at 4MHz was obtained by placing a 1Ω resistor in series with the transducer and measuring the voltage across this resistor. It was found to be roughly 10Ω . This meant that an amplifier with a very high slew rate and with low output impedance was needed.

The Apex PA19 was chosen after a careful search of available options. In this circuit, the large current demands of the transducer limit the amplifier output voltage at the transducer to about 15V peak to peak (at the transducer resonance), even with a supply of $\pm 40V$. The pulse power output is estimated to be of the order of 5W. Pulse repetition rates used were in the order of 1kHz, and it was found that the amplifier dissipated enough heat during this operation to require forced air cooling. This was accomplished via a heatsink and fan.

Voltage gain was set at a nominal value of 4.7, in order to fully exploit the maximum 80V peak to peak range from a 0 to 20V peak to peak output available from the signal generator. A compensation network consisting of a 220Ω resistor and a 33nf capacitor was placed across the inputs to eliminate oscillation. Small signal open loop gain was flat within 3dB to greater than 10MHz (see Figure 4.5), but the maximum voltage output was down to 50.2V peak to peak at 5MHz (see Figure 4.5).

The output from the receiving transducer could also be amplified. Signal magnitudes depended on the sample being examined, but were typically of the order of 10mV. Noise on the output signal occasionally made it difficult to determine the location of the first received peak, which was used to measure transit time. A small-signal amplifier was then constructed with a band-pass characteristic to increase the

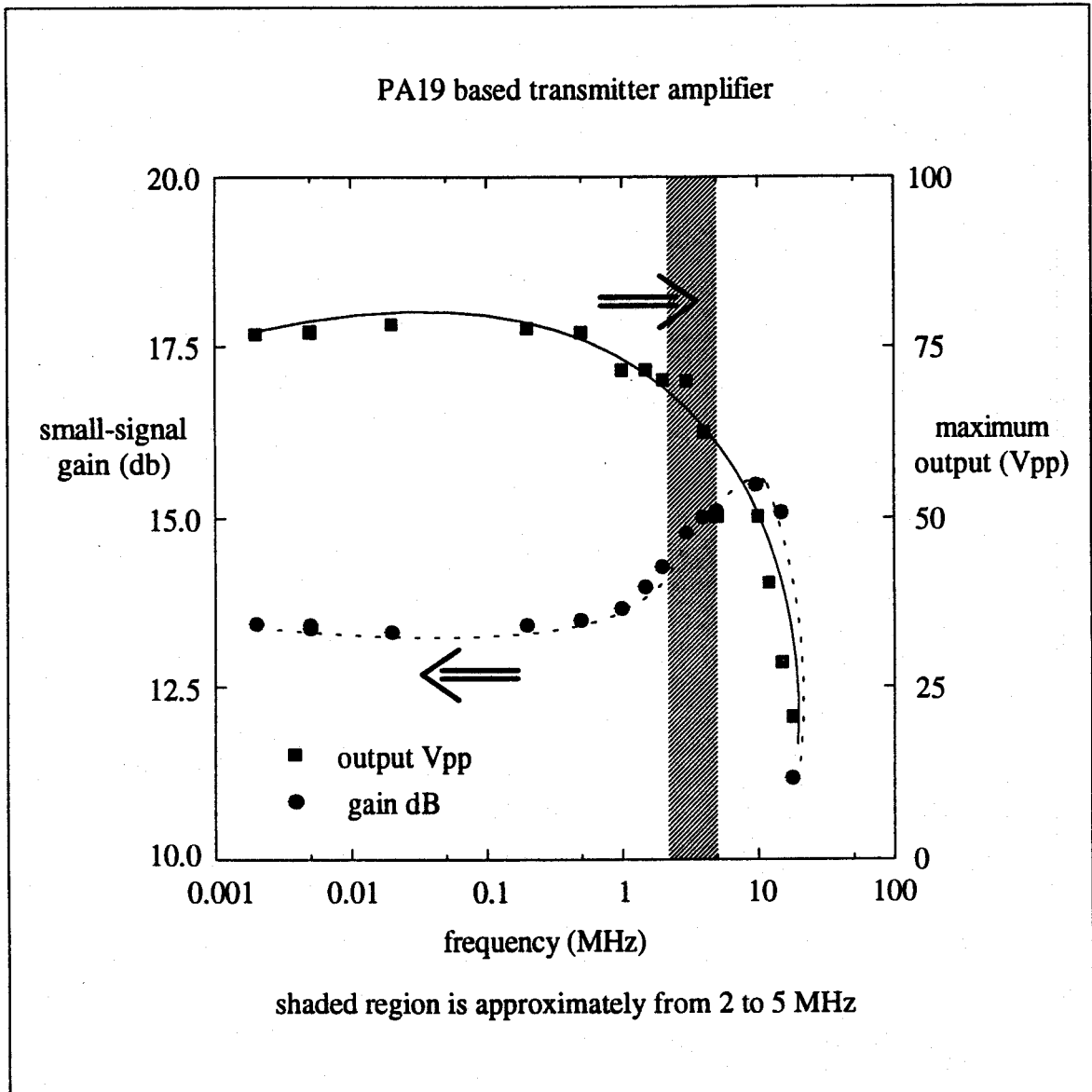


Fig. 4.5 Performance data for the PA19 based transmitter amplifier.

signal to noise ratio. Figure 4.6 shows the design of the output amplifier. A high pass filter was cascaded with a low pass filter into an inverting amplifier. The filters are based on a two pole Bessel design, and the nominal pass band is 1MHz to 6MHz. Nominal voltage gain in the pass band is 47.

The output amplifier did not have a very flat passband, but did significantly

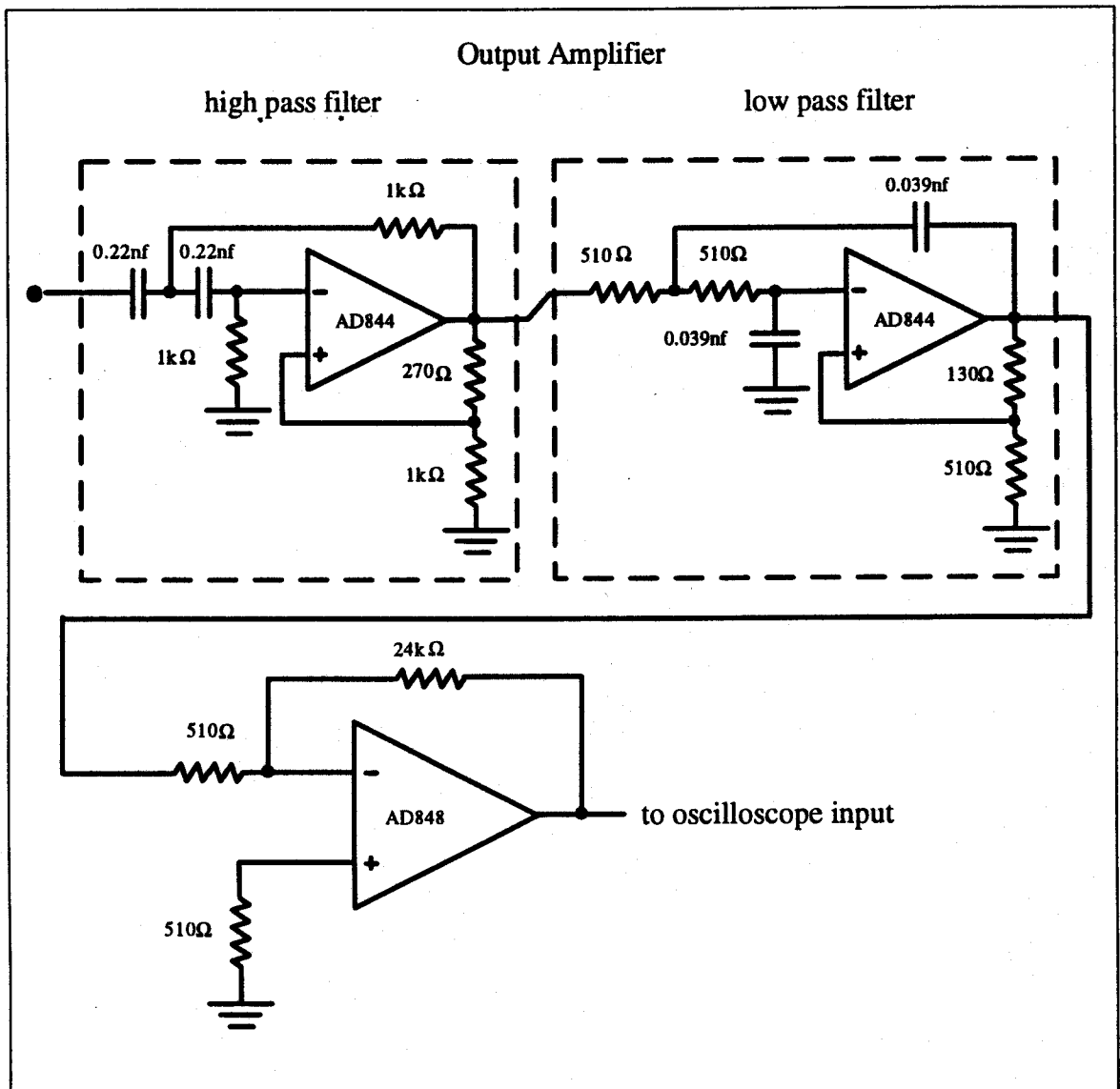


Fig. 4.6 Design of output amplifier.

reduce the problem of noise. For the differential measurements, a flat passband is not necessary. Figure 4.7 shows the frequency response of the amplifier as measured on the same oscilloscope input ($1\text{ M}\Omega$) used during the ultrasonic measurements.

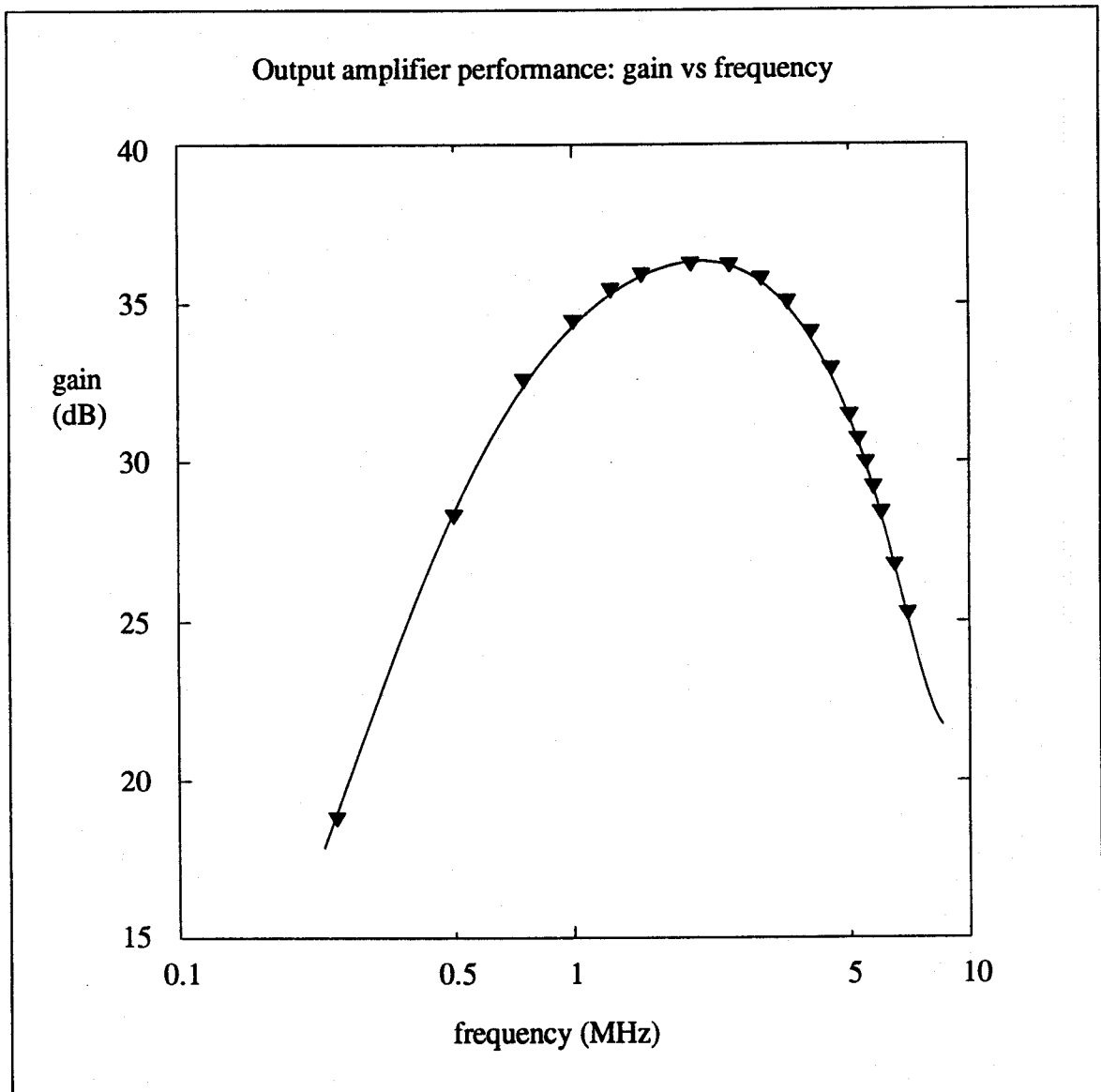


Fig. 4.7 Performance of output amplifier.

4.1.4 Oscilloscope Measurements

The measurements of transit time and signal amplitudes were made using the Tektronix 2465A oscilloscope. This oscilloscope has built in time and amplitude measurement capabilities, with cursors adjusted by the experimenter to the desired points of the waveforms.

The minimum time resolution used for the measurements in Chapter 5 was 1nsec. The manufacturer's performance specifications claim an accuracy of $\pm 0.5\%$ of the measurement plus 0.3% of full scale, and the repeatability of choosing the measuring points is estimated by the author to be $\pm 2\text{nsec}$. Over the course of the experiments it was found that transit time measurements were very consistent, and were repeatable to better than 1%.

Voltage amplitude measurements are considered by the manufacturer to be $\pm 1.25\%$ plus 0.03 times the voltage per division being used. For a 10mV signal being measured on 2mV per division scale, this corresponds to a total error of 1.85%. Again there is some error introduced by the external apparatus. Due to the random nature of the bond quality, some scatter in measurements is expected.

4.1.5 Scanning Electron Microscopy

A number of SEM photographs were taken of samples before and after thermal fatigue testing to attempt to determine how thermal fatigue was affecting the samples. These samples were not subject to ultrasonic testing, except in one case noted in Chapter 5. It was expected that the dominant mode of failure would be damage to the fibre-matrix interface, and this could be examined visually under the SEM. Samples were prepared as described in Section 4.2.2.

All the samples for SEM testing were polished on a Dap-U polishing wheel, with final polishing using 1 micron diamond paste. Samples were examined under an

optical microscope to ensure polishing had removed all cutting damage, as described in Section 4.2.2. For the SEM examinations it was necessary to gold coat the samples so they would have a conducting surface. The gold coating was applied by sputtering in an evacuated chamber at room temperature. Results of the SEM examinations are given in Chapter 5.

4.2 Test Materials

Three different polymeric fibre composites were examined in this work. Two geometrical arrangements were examined, continuous uniaxial fibre (composites 1 and 2) and randomly oriented fibre (composite 3). All materials were obtained from Goodfellow Metals Ltd. These were:

composite 1: carbon fibre uniaxial in vinylester matrix

composite 2: aramid (Kevlar®) fibre uniaxial in vinylester matrix

composite 3: aramid fibre randomly oriented in polyphenylene sulphide (PPS) matrix

Both composites 1 and 2 were manufactured by pultrusion, which involves feeding continuous fibres through a resin bath and then a die. Composite 3 is an injection molded sample.

Pultruded composites such as composites 1 and 2 are widely used in the aerospace industry for structural applications[23, 26]. They are also often pultruded as

tubes for industrial applications, due to the good chemical resistance of vinylester[24]. Randomly oriented fibres in plastics, similar to composite 3, are often used as non-structural parts for the automotive industry, appliances, and for electronics[23, 24, 26]. Electrical applications include sockets, integrated circuit and capacitor encapsulations, switches, and relay components.

4.2.1 Properties

Important properties of the components of the experimental materials are shown in Table 4.1. It is important to note the large difference in the thermal expansion coefficients between the polymer matrix materials and the fibre materials, which is responsible for thermal fatigue damage in the specimens. These numbers are for the axial coefficients of the fibres.

The thermal conductivity of the materials is also very important in this experiment. All the materials other than the carbon fibres have very low thermal conductivities. This means that temperature gradients will develop across the specimens during thermal cycling. This limits the size of the specimens because it is desirable to minimize the stresses due to thermal gradients across the sample in comparison to the stresses induced by the different thermal expansions. Measurements of the temperature gradients across specimens in the thermal cycling apparatus are presented in Section 5.1.

The fibre volume content of the composite samples was determined from image

Table 4.1 Properties of component materials. Asterix indicates from manufacturer's specifications.

property	carbon fibres	aramid fibres	vinylester	PPS
density (kg m^{-3})	1820*	1450*	1120*	1350 [21]
specific heat ($\text{J kg}^{-1}\text{K}^{-1}$)	709 [24]	1400 [22]	1500 [21]	1100 [21]
thermal expansion ($1 \times 10^{-6}\text{K}^{-1}$)	-0.5 [23]	-2 [23]	50 [21]	50 [21]
thermal conductivity ($\text{Wm}^{-1}\text{K}^{-1}$)	50 [22]	0.02 [23]	0.2 [21]	0.29 [21]

analysis or density measurements. Results are shown in Table 4.2. Fibre content does influence the magnitude of the interfacial stresses due to thermal cycling[25, 26] and is discussed in Chapter 5 and appendix A.

Table 4.2 Fibre content of the composites.

material	density (kg m^{-3})	fibre percent by volume	fibre percent by weight
composite 1	1470	50	62
composite 2	1260	61	70
composite 3	1380	30	31

4.2.2 Sample Preparation

All samples were cut using an oil cooled diamond saw. Composites 1 and 2 were continuous fibre specimens in the form of long cylindrical rods of diameter 10mm. Fibre diameters were approximately 8×10^{-3} mm and 10×10^{-3} mm respectively. Composite 3 was in the form of a square plate, about 7mm thick and 150mm square. Fibre diameter for composite 3 was about 10×10^{-3} mm. It was found that the saw caused damage visible under the SEM. The faces to be mounted on the transducers were then polished to remove damage caused by the saw. Unpolished specimens were more attenuating, very likely due to this damaged surface layer.

For composites 1 and 2, two different sample shapes were cut to examine ultrasonic propagation parallel and perpendicular to the fibre direction. Figure 4.8 demonstrates how the samples were cut.

Thicknesses of the samples in the direction for wave propagation were then measured, using a Sylvac electronic measuring probe, to a precision of 1×10^{-3} mm. This probe has a contact surface area of about 1mm^2 . Many measurements were made for each specimen to determine how close to parallel the specimens were. The maximum allowed variation across a sample was 0.1mm (about 5°), and most were significantly better than that. These variations were due to non-parallel cutting, not surface roughness as samples were polished before thickness measurements.

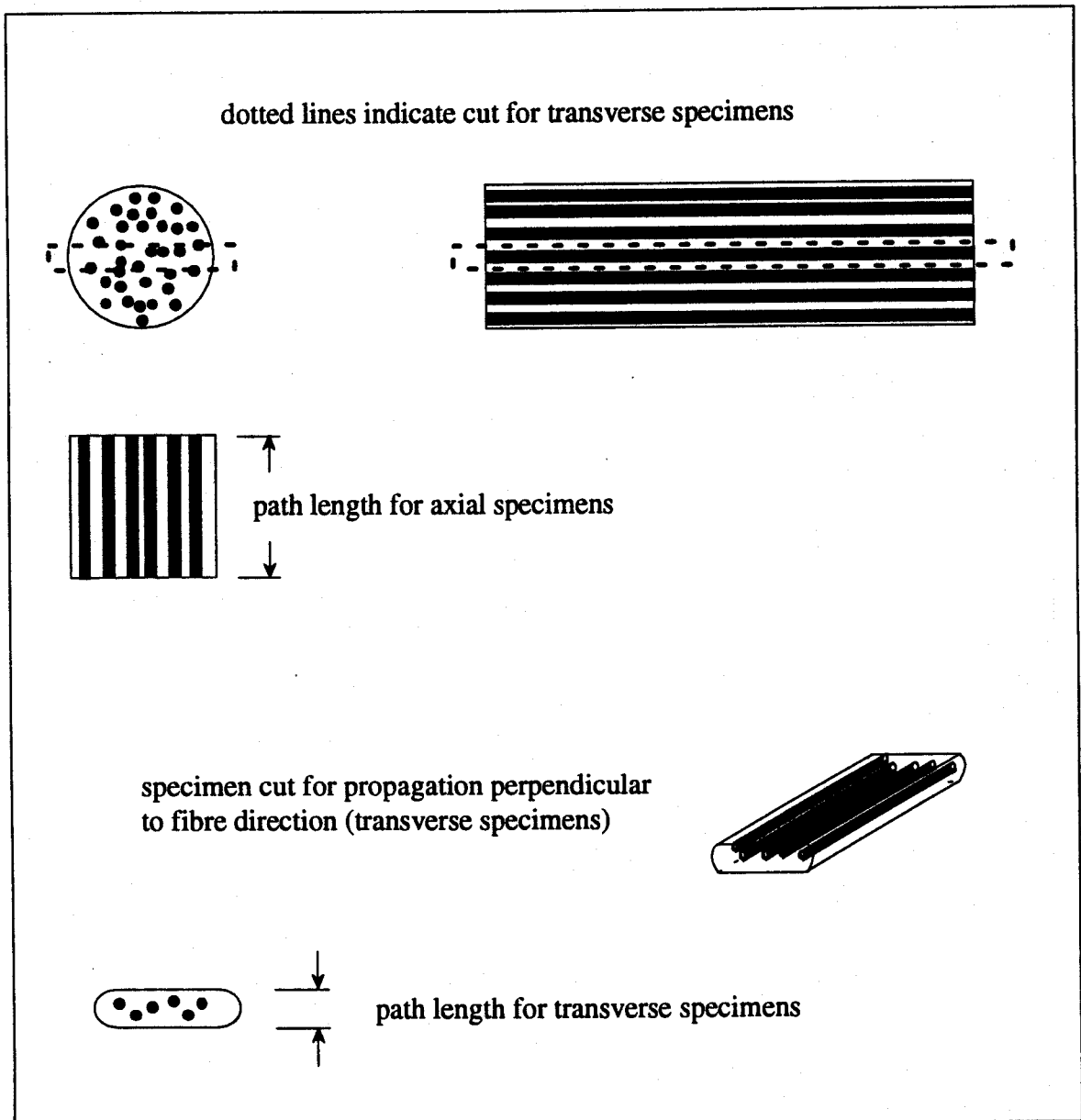


Fig. 4.8 Specimens cut from composites 1 and 2 (transversely isotropic).

4.3 Thermal Cycling

Thermal cycling of the specimens was carried out in an apparatus designed and built in the Mechanical Engineering Department at the University of Saskatchewan. A schematic is shown in Figure 4.9. Samples are moved from a furnace to a refrigerated airspace and back. Soak times in each are controlled by the user from a personal computer. The number of cycles to be performed in a run is also controlled from the personal computer.

The refrigeration unit was kept at a constant temperature throughout all the experiments. The air temperature at the height of the samples was -35°C . The furnace temperature was varied along with the soak times in each chamber. The details of the temperature cycles are presented in Section 5.1.

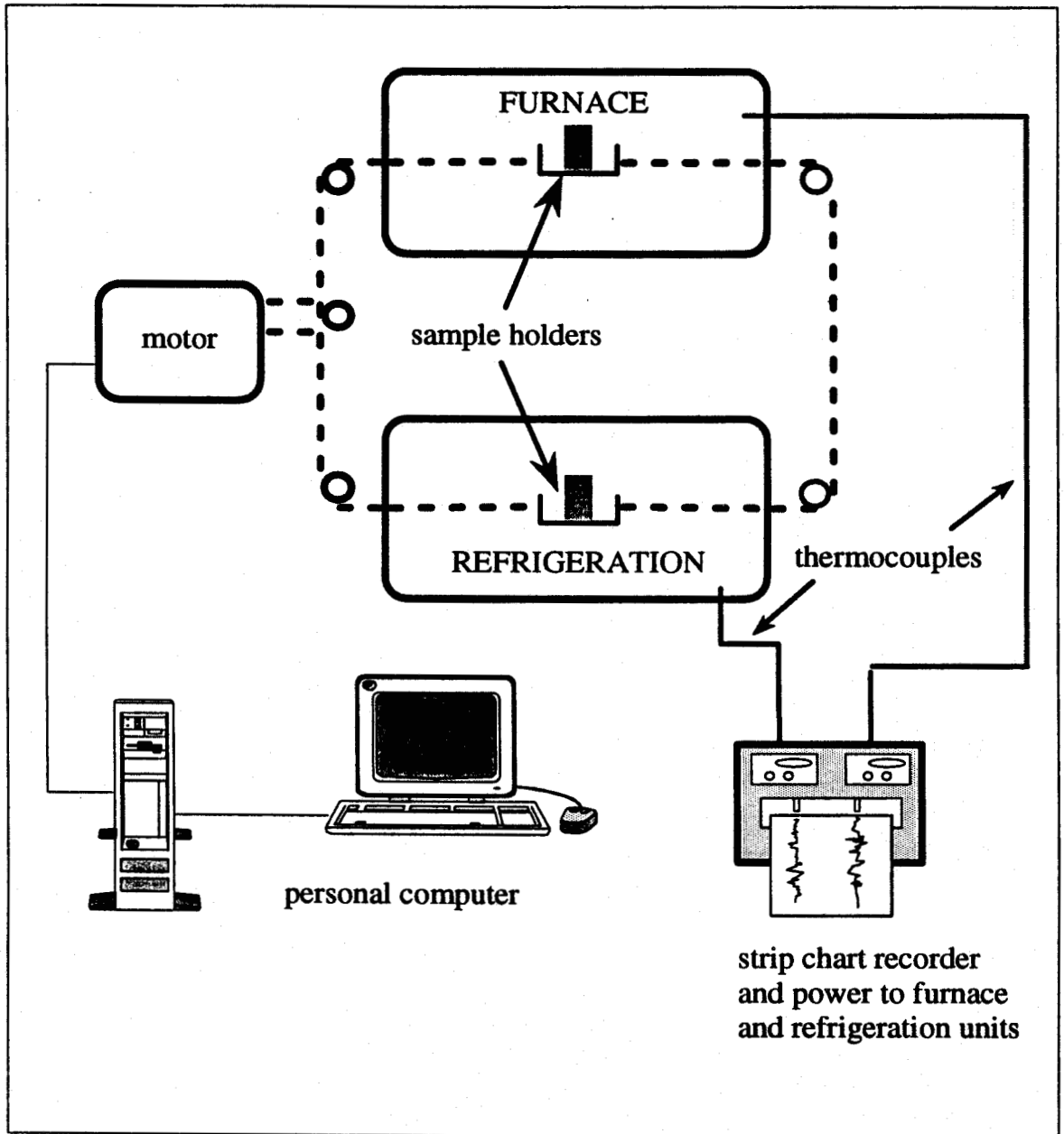


Fig. 4.9 A block diagram of the thermal cycling apparatus.

5. RESULTS AND DISCUSSION

5.1 Thermal Cycling

Thermal cycling of the composite materials was carried out as described in Section 4.3, with specimens being moved from the furnace to the refrigeration unit and back, as in Figure 4.9. At each station, the specimens were held for a user-defined time. There were two different thermal cycle schedules used in these measurements, denoted by schedule 1 and schedule 2. The first cycle schedule involved four minute soak times in each chamber, with a higher furnace temperature than the second cycle schedule, which used six minute soak times to achieve greater range and smaller thermal gradients in the specimens.

The temperature of the refrigeration unit was kept constant throughout all the experiments at -35C. This was measured by attaching a thermocouple directly to the specimen holder and allowing it to reach equilibrium in the refrigeration unit. The thermocouple used by the refrigeration controller was in a slightly different location, and this thermocouple measured a variation of $\pm 3C$ during experiments.

For schedule 1, the oven temperature was kept at 85C at specimen height, measured as above. Schedule 2 used a temperature of 80C, because of the longer soak time. The glass transition temperatures of the matrix materials were as low as 90C, so a lower oven temperature was used to prevent stress relaxation and flow of the matrix material. The oven temperature was very consistent with time, varying less than $\pm 2C$.

The true temperature ranges experienced by the specimens during the experiments were estimated by attaching thermocouples to actual specimens and using

a strip chart recorder to plot the results. Two thermocouples were used in each case. One thermocouple was placed in a hole drilled to the approximate centre of the specimen, and the other fixed to the outside. Not only does this provide information about cycle temperatures, but also the temperature gradient across the specimen. It was found that the carbon fibre materials had higher effective thermal conductivities, due to the conductivity of the carbon fibres themselves (see Section 4.2.1). For the axial fibre specimens, only the rod shaped specimens were examined, as the flat specimens were very thin and would have developed similar temperatures but smaller gradients.

For composite 1, a 15mm length was cut off the rod and thermocouples fixed to the centre through a hole, and at the outside of the rod at the centre position. The specimen was taken from room temperature to the furnace, then to the refrigeration chamber. A 7mm long rod-shaped specimen of composite 2 and a 10mm×10mm×6.5mm specimen of composite 3 were also tested for temperature profiles in cycle 2. Figure 5.1 shows approximate temperature-time curves for this experiment, as estimated from the above measurements.

It was difficult to continuously measure temperatures as the specimen holders moved between chambers, but it was found that the maximum and minimum temperatures did not change more than 1-2C after the first cycle.

There was a definite temperature gradient across the specimens, as much as 10C in some cases. This was an important factor in limiting the size of specimens, as the experiment was designed to measure thermal fatigue damage, not thermal shock damage, which results from thermal gradients across a material.

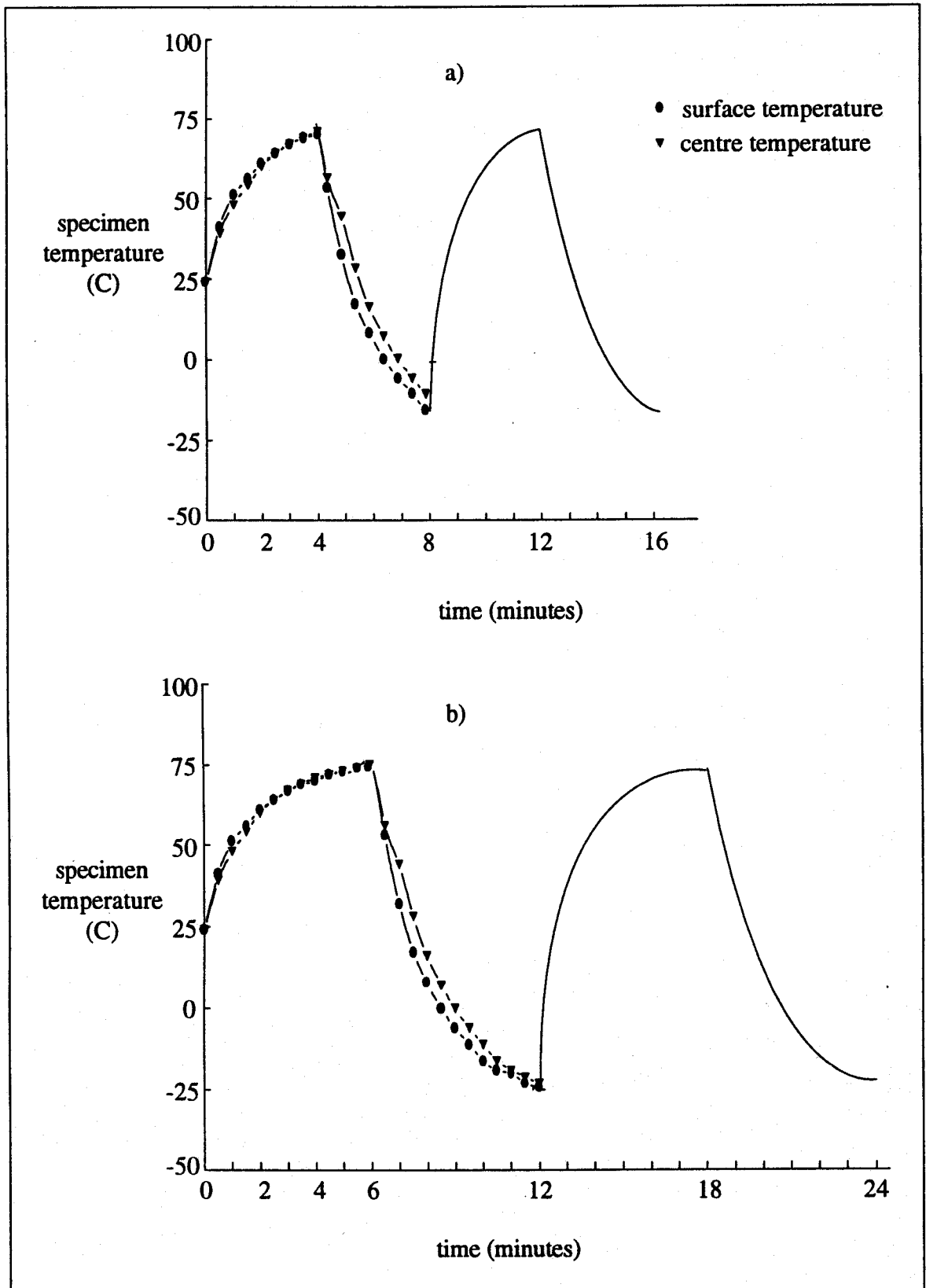


Fig. 5.1 Temperature versus time plot for thermal cycle schedules: a) schedule 1 and b) schedule 2. Composite 1 test sample.

5.2 Composite 1: Carbon Fibres in Vinylester Matrix

Composite 1 refers to a carbon fibre in vinylester composite, which was in the form of a cylindrical rod with continuous fibres running along its axis. The volume percent of fibre in the composite was 50%. Other information about the material is given in Section 4.2. This composite showed consistent degradation of material properties due to thermal fatigue.

Measurements performed on composite 1 included measurements of absolute ultrasonic velocity v and attenuation α in an unfatigued state, as well as changes in velocity and attenuation due to thermal fatigue. Ultrasonic measurements were performed using longitudinal waves either parallel (v_{\parallel} and α_{\parallel}) to the fibre axis or perpendicular (v_{\perp} and α_{\perp}), using frequencies from 3.00MHz to 5.00MHz. All ultrasonic measurements were performed at room temperature, 19C.

For all the plots of ultrasonic attenuation and velocity versus number of thermal cycles, measured quantities were normalized to the unfatigued state for each individual specimen. These were averaged, for 2-4 specimens, to give the data shown. Lengths of specimens were kept very close to eliminate variation in effects due to specimen size. Curves drawn on the plots are not meant to represent a particular curve fit but rather are a visual aid. This treatment is consistent for all the graphs of velocity and attenuation change with cycling throughout Chapter 5.

Error bars are shown for the first point on each plot of velocity and attenuation change. The magnitude of these errors was estimated from the measurement error as described in Section 4.1.4.

5.2.1 Determination of Ultrasonic Velocity and Attenuation

A significant frequency dependence in the transit times was found for all specimens examined. This was determined to be due to the boundary layer as follows. The measured transit time t_m is modeled as the sum of the two boundary layers t_a and t_b , and the transit time t_s through the sample, as illustrated in Figure 5.2. Now the actual velocity in the sample can be determined from measurements of samples of different lengths. The frequency dependence of the transit times was found to be a characteristic of the boundary layer, not the materials.

When the boundary layers were modeled as above, the measured time t_m is given by:

$$t_m = t_a + t_b + t_s \quad (5.1)$$

The path length L_s through the specimen only, can be written as:

$$L_s = v_s \times t_s = v_m \times t_m - v_a \times (t_a + t_b) \quad (5.2)$$

Where v refers to the velocity of propagation in the medium indicated by the subscript. If the boundary transit times are assumed to be constant, a plot of measured transit times versus path length will have a slope given by the measured velocity, v_m .

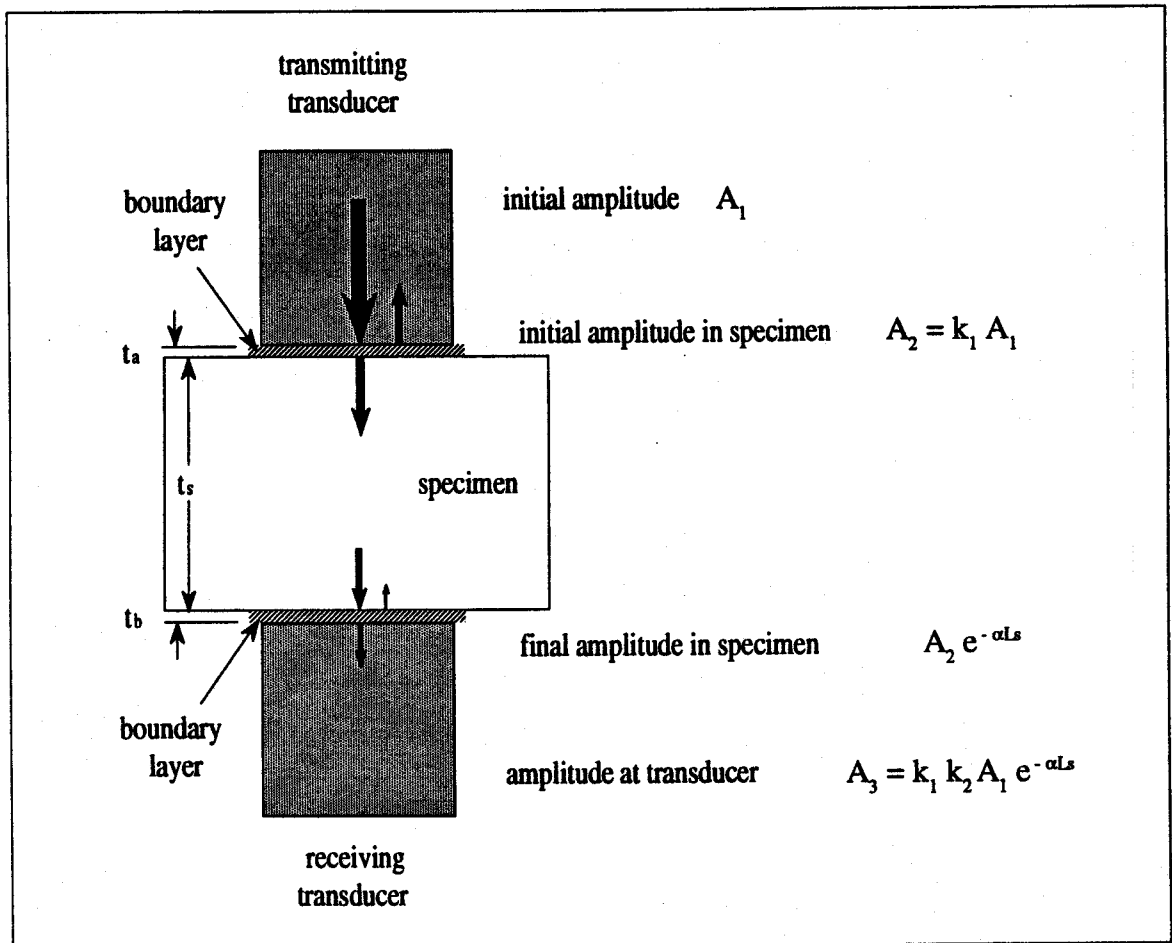


Fig. 5.2 Schematic of transducer assembly for absolute measurement derivations.

This value is related to the velocity in the specimen by:

$$v_m = \frac{L_s + L_a + L_b}{t_s + t_a + t_b} \quad (5.3)$$

$$v_m \approx v_s + \frac{L_a + L_b}{t_s + t_a + t_b} \approx v_s \quad (5.4)$$

Two approximations are made in Equation 5.4: that the transit times through the boundary layers are small compared to the specimen time, and that the second term on the right side of Equation 5.4 is small compared to v_s . The thickness of the

boundary layers is very small, only enough to wet the surfaces, and therefore the transit times through the boundaries will be very small compared to the specimen transit times. The next term is in dimensions of velocity, and will give a number much smaller than either the velocity in the coupling medium or the specimen, and can also be safely neglected compared to the velocity in the specimen.

Another important assumption is that the boundary layer effects are consistent from sample to sample. The ability to make any of the measurements described in this chapter depends on this consistency. The measurements of absolute velocity and especially absolute attenuation provide a means of checking this assumption.

To find the absolute attenuation in the specimen material, refer to Figure 5.2. The experimenter measures the amplitude of the initial wave A_1 at the transmitting transducer, and of the received wave A_3 at the receiving transducer. There is assumed to be one reflecting surface at each boundary layer, with coefficients of transmission given by k_1 and k_2 . The specimen is characterised by an exponential decay described by the attenuation parameter α . The measured received amplitude can be expressed in terms of the measured initial amplitude as:

$$A_3 = k_1 k_2 A_1 e^{-\alpha L_s} \quad (5.5)$$

The attenuation coefficient in the material can be isolated from Equation 5.5 and written as:

$$\alpha = \frac{\ln(k_1 k_2)}{L_s} = -\ln\left(\frac{A_3}{A_1}\right) \times \frac{1}{L_s} \quad (5.6)$$

The terms on the right side of Equation 5.6 are measured values. If these values are

plotted against L_s^{-1} , the result should be a straight line with slope $-\ln(k_1 k_2)$ and a y-axis intercept of α , the actual material attenuation. This derivation can also be found in Read and Dean[10].

As previously mentioned, the important assumption being made here is that the slope of the line, as given by the transmission coefficients of the bonds, remains constant for all trials. If this is true, the data should be very linear. This is why the correlation coefficients, a measure of the closeness of fit, are quoted as supporting this assumption.

The values of absolute ultrasonic velocity v_H and attenuation α_H were determined for composite 1 as previously described. The graphs used for the calculations are shown in Figures 5.3 and 5.4, with values summarized in Table 5.1.

For Table 5.1, errors given are estimates of the standard deviation of the value. Regressions and error estimation were performed by the software package Sigma Plot version 5.0. The data was fit to a linear relationship, and the correlation coefficients are for this fit.

As mentioned in Section 3.2.1, the velocity is shown to be independent of frequency within the error of the measurements. Correlation coefficients of the velocity data indicate that the assumption of consistent bond quality is valid. The values for attenuation coefficients increase with frequency. Again the correlation coefficients for the attenuation data indicate that the assumption of consistent bond quality is valid.

The velocity measured here corresponds to v_1 in Equation 2.33, and with a density of 1470 kg m^{-3} for composite 1, c_{11} is found to be 19.4GPa.

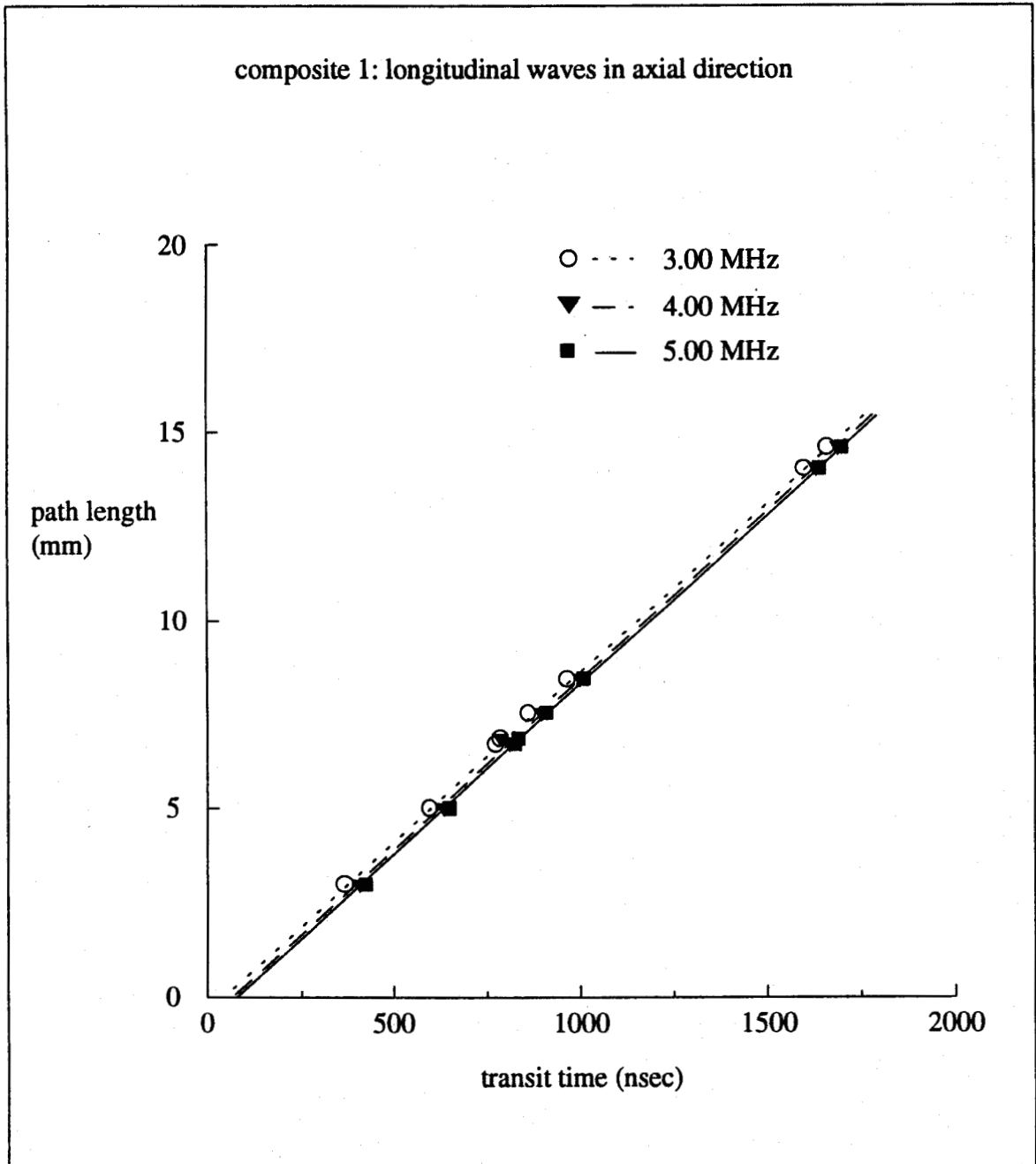


Fig. 5.3 Dependence of transit time on specimen length. (Graph used for determination of v_l for composite 1.)

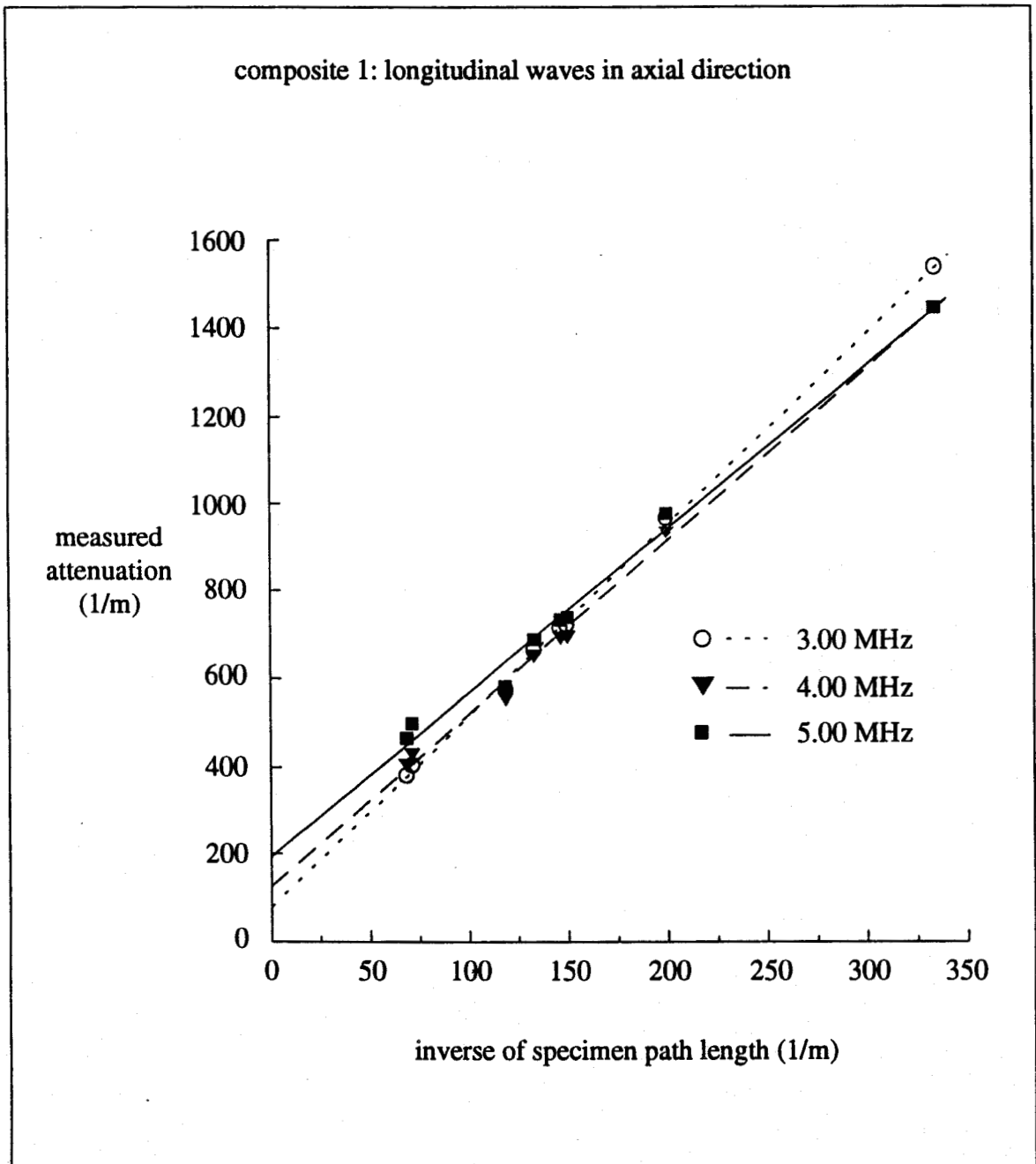


Fig. 5.4 Dependence of attenuation on specimen length. (Graph used for determination of α_l for composite 1.)

Table 5.1 Absolute velocity and attenuation values for composite 1 (unfatigued).

excitation frequency (MHz)	velocity (m/sec)	correlation coefficient of linear fit	attenuation coefficient (1/m)	correlation coefficient of linear fit
3.00	8959 ± 41	0.9994	78 ± 11	0.9994
4.00	8986 ± 130	0.9993	125 ± 17	0.9980
5.00	9071 ± 52	0.9990	194 ± 25	0.9954

5.2.2 Ultrasonic Waves Perpendicular to the Fibre Axis (Composite 1)

The material properties perpendicular to the fibre axis are less influenced by the fibres. Ultrasonic velocities are lower, and attenuations higher. Much smaller path lengths were used for these measurements than for axial, due to the specimen geometry and attenuation. Absolute measurements were not made due to this restriction on path length.

Figures 5.5 and 5.6 display graphically the attenuation and velocity data for these specimens in thermal cycle 1 and 2 respectively. Two specimens for cycle 1 and four specimens for cycle 2 provided the data. Specimen lengths were 3.5 ± 0.5 mm.

For all of these specimens examined, ultrasonic attenuation increased and ultrasonic velocity decreased as the number of thermal cycles increased. Magnitude of damage did not change when the thermal cycle schedule was changed. The magnitude of the velocity decrease was independent of frequency, but the magnitude of

attenuation change increased with frequency. Both plots show the greatest change in the first one or two hundred thermal cycles, with much more gradual change throughout the rest of the measurements.

SEM photographs of these specimens of composite 1 give clear indications of damage after thermal cycling. Figures 5.7 to 5.10 show SEM photographs for a typical specimen before and after thermal cycling. Magnifications are given in the figure captions. All of these photographs are taken from one specimen.

In Figure 5.8, the specimen had undergone 1000 thermal fatigue cycles (cycle schedule 2), and the matrix material here appears to show more cracks than the unfatigued specimen in Figure 5.7. Figures 5.9 and 5.10 are at the same magnification, with the specimen in Figure 5.10 fatigued 1000 cycles. The fatigued specimen shows a broken fibre and extensive matrix cracking around this fibre.

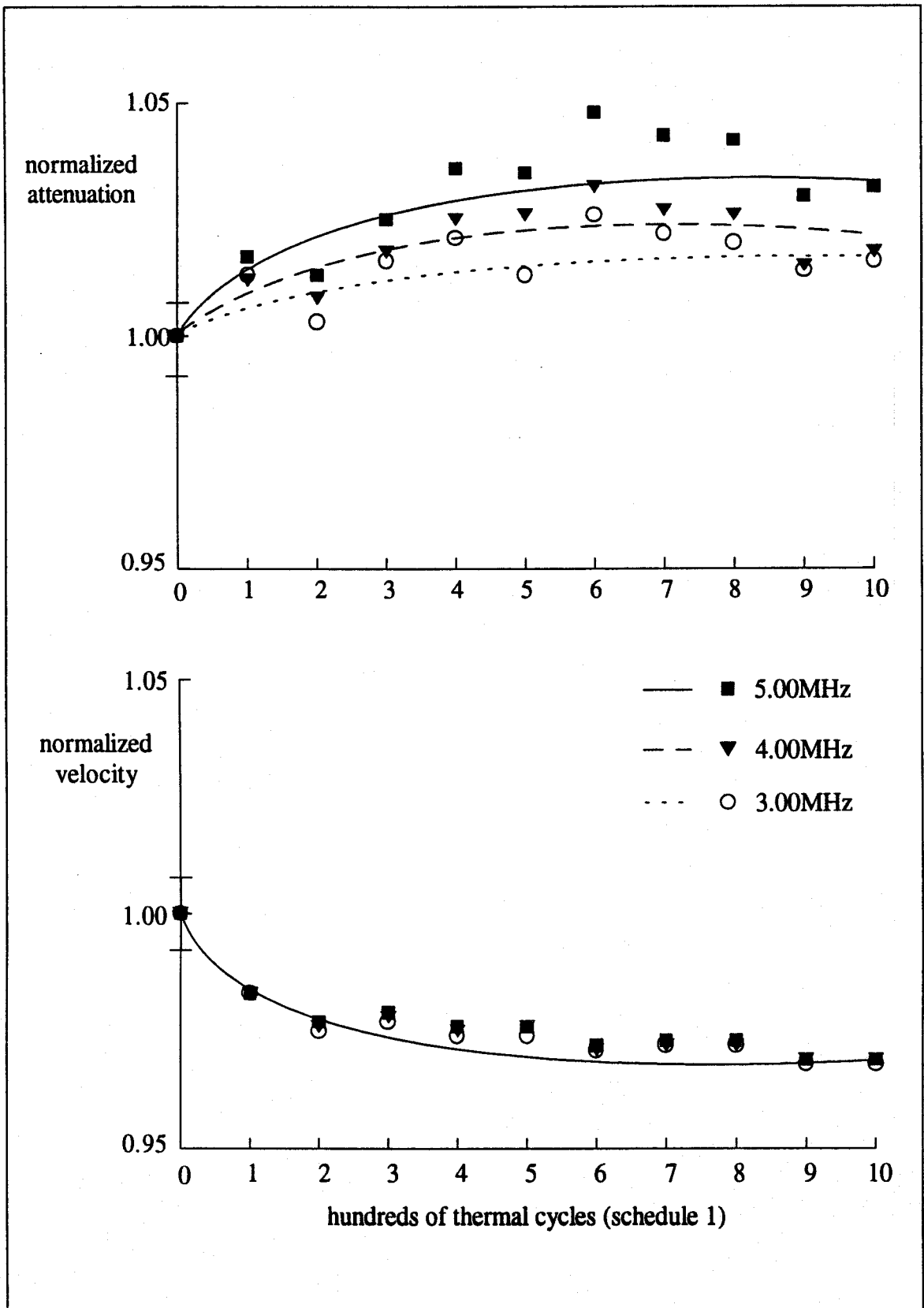


Fig. 5.5 Graph of velocity and attenuation changes for composite 1: longitudinal wave perpendicular to fibre axis (thermal cycle schedule 1).

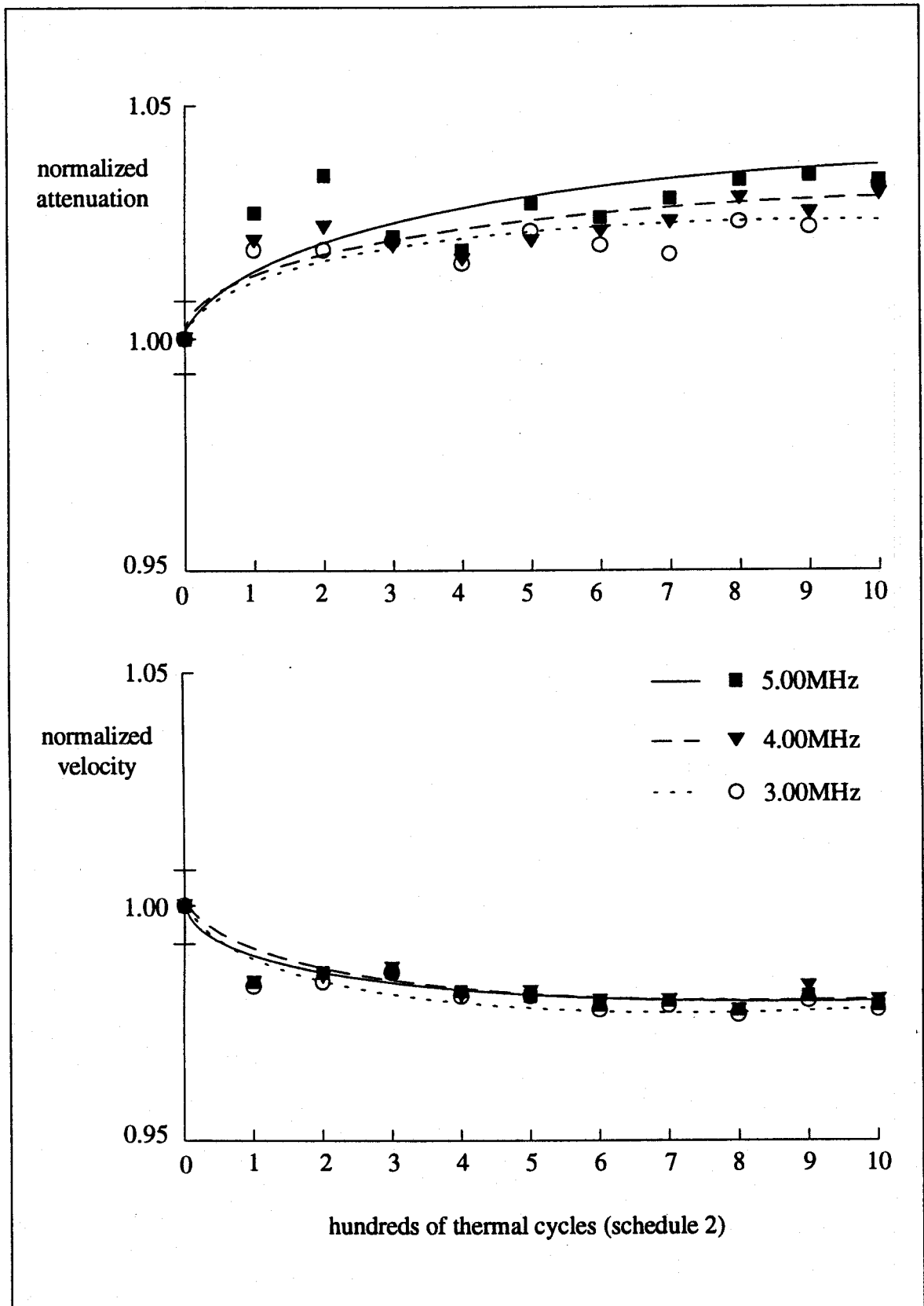


Fig. 5.6 Graph of velocity and attenuation changes for composite 1: longitudinal wave perpendicular to fibre axis (thermal cycle schedule 2).

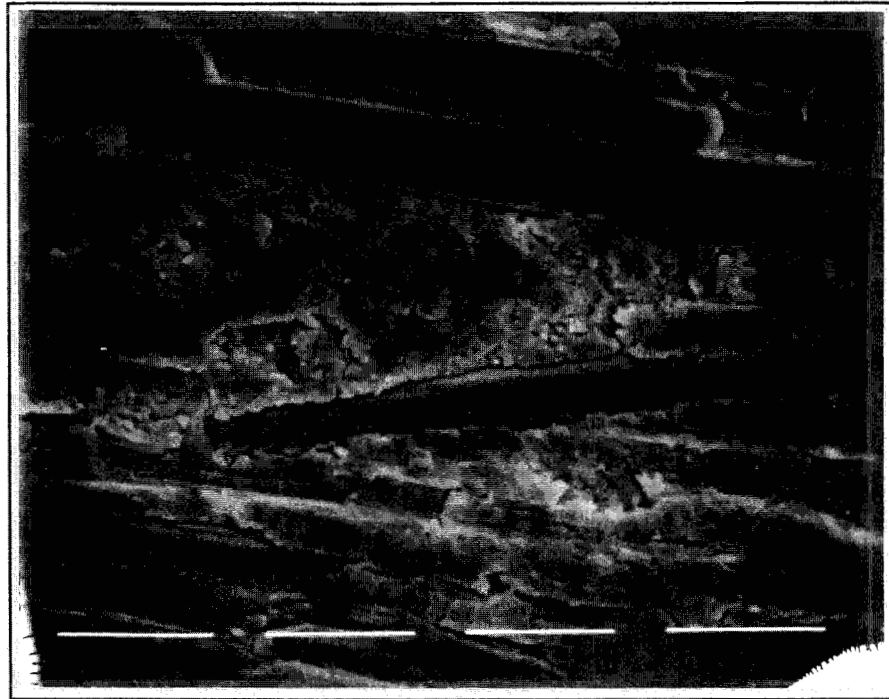


Fig. 5.7 SEM photograph of composite 1, 2000× magnification, unfatigued.



Fig. 5.8 SEM photograph of composite 1, 2000× magnification, 1000 cycles (schedule 2).

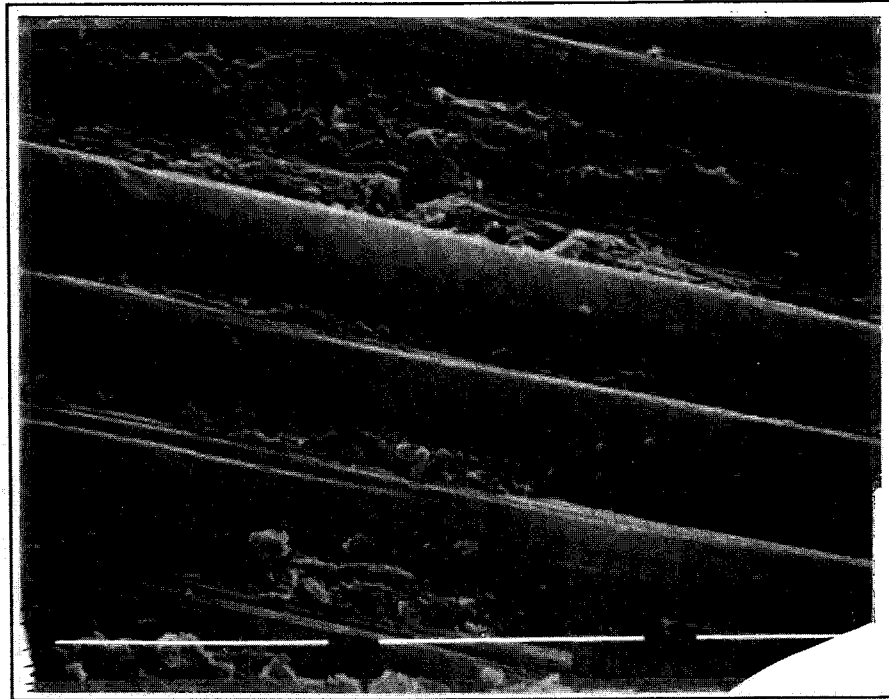


Fig. 5.9 SEM photograph of composite 1, 3500× magnification, unfatigued.

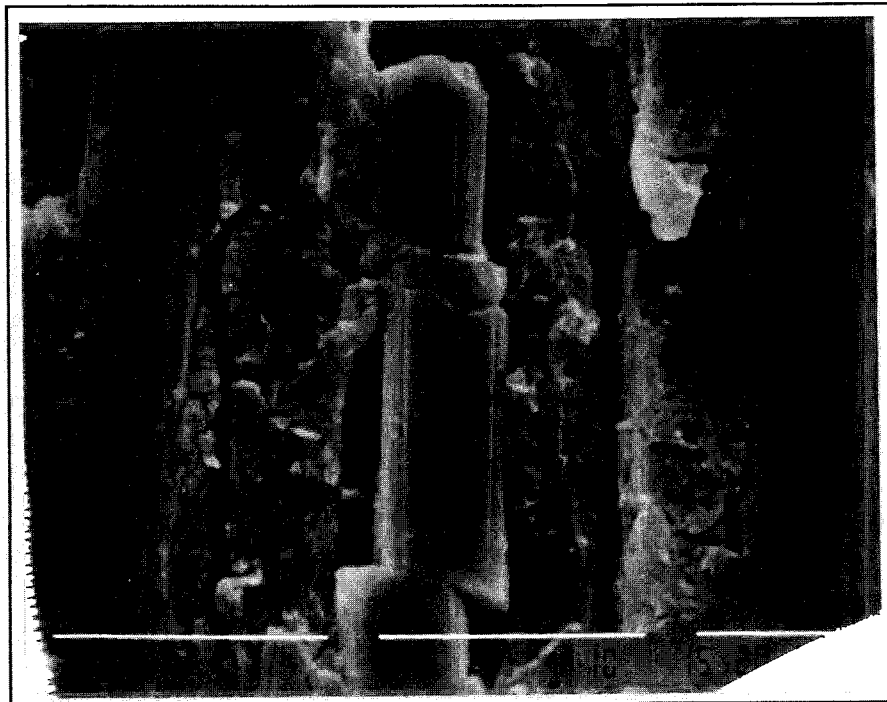


Fig. 5.10 SEM photograph of composite 1, 3500× magnification, 1000 cycles (schedule 2).

5.2.3 Ultrasonic Waves Parallel to the Fibre Axis (Composite 1)

Changes in v_l and α_l in composite 1 due to thermal cycling were evaluated and are presented in Figure 5.11. The velocity does not vary more than 0.5% from the unfatigued state at any time. Attenuation shows a large increase after 200 cycles, and a slower increase thereafter. The higher frequencies are more attenuated.

Specimen lengths for these measurements were 14.5 ± 0.5 mm. Four individual specimens were evaluated. Composite 1 has good thermal conductivity due to the carbon fibre, and was less attenuating than composite 2, which allows the use of larger specimens. This will decrease the relative error of the measurements, and as can be seen from the plot of normalized velocity versus number of cycles in Figure 5.11, the measurements are very consistent over the course of the experiment. This indicates that the method will be very sensitive to changes in velocity.

SEM studies of composite 1 also showed damage in the plane perpendicular to the fibre axis. Figure 5.12 shows a view of an unfatigued specimen. Large voids at the surface can be seen at the left edge of the photograph. A large matrix rich area can be seen at the top centre of the photograph.

It was found that the isolated fibres in matrix rich regions showed more visual evidence of damage, as for Figure 5.14. This figure shows significant fibre-matrix debonding, and microcracks in the matrix spreading radially from the fibre axis. The specimen was fatigued 800 cycles using schedule 2. Figure 5.15 shows the same specimen after 600 cycles, in a more fibre dense region, with less pronounced debonding. Figure 5.13 shows a similar view of an unfatigued specimen.

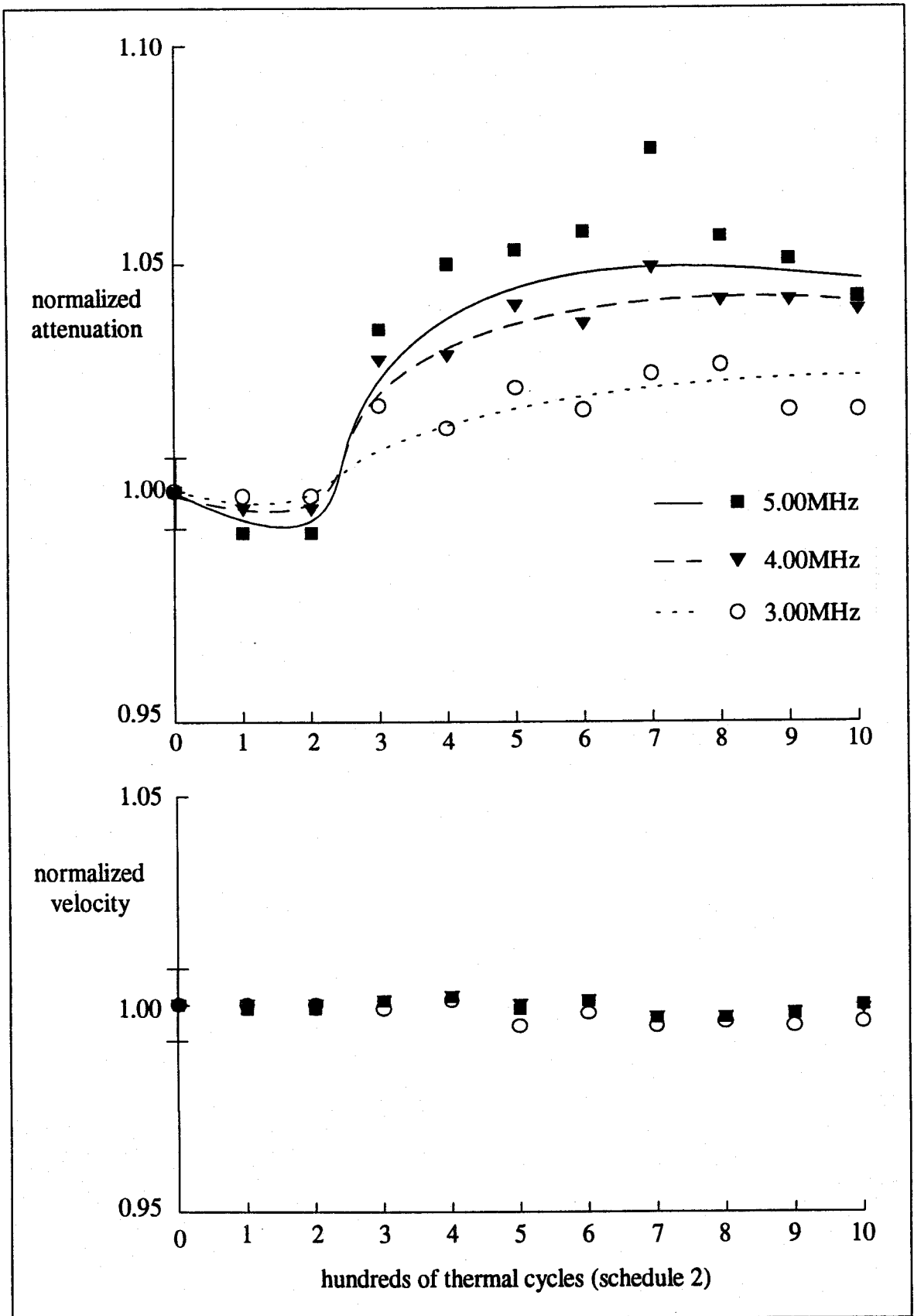


Fig. 5.11 Graph of velocity and attenuation changes for composite 1: longitudinal wave parallel to fibre axis (thermal cycle schedule 2).

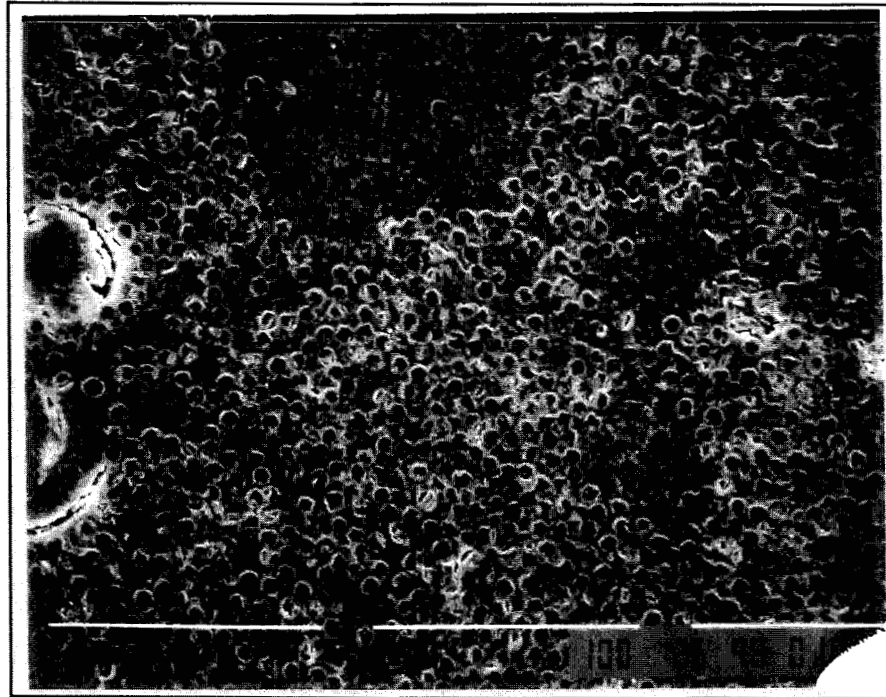


Fig. 5.12 SEM photograph of composite 1, perpendicular to fibre axis. The magnification is 350 \times , and the specimen is unfatigued.

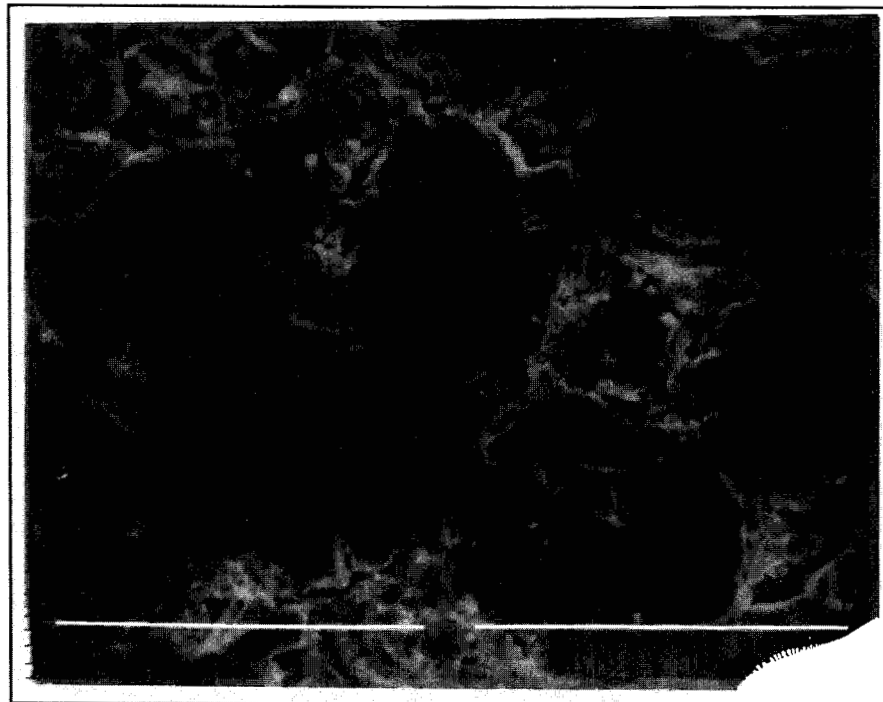


Fig. 5.13 SEM photograph of unfatigued specimen of composite 1, 5000 \times magnification. See Figures 5.14 and 5.15 for comparison.



Fig. 5.14 SEM photograph of composite 1, after 800 cycles (schedule 2). Magnification is 5000 \times . Note low fibre density.

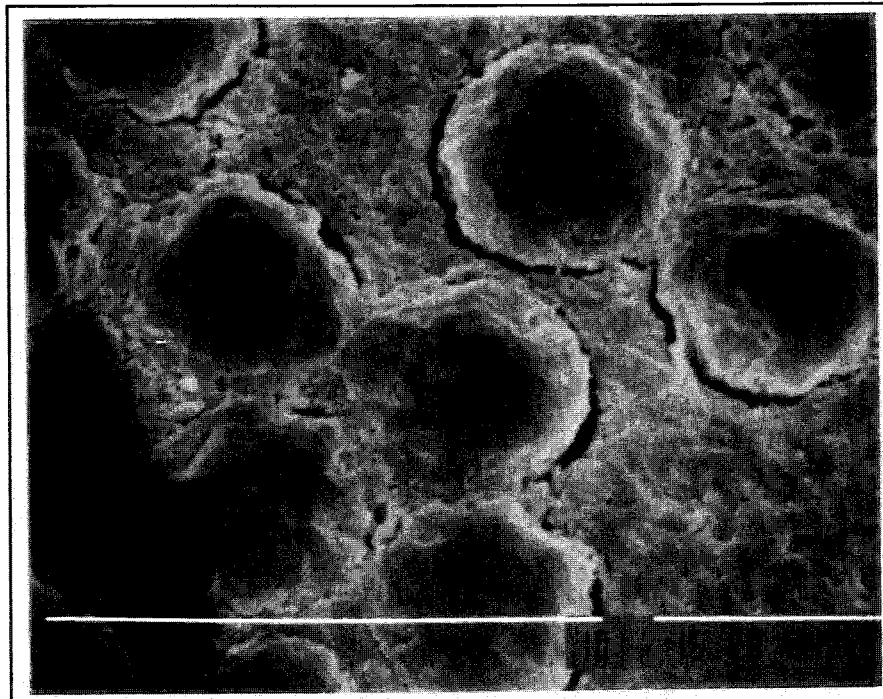


Fig. 5.15 SEM photograph of composite 1 after 600 cycles (schedule 2). Magnification is 7500 \times .

5.3 Composite 2: Aramid Fibres in Vinylester

Composite 2 refers to an aramid fibre in vinylester composite, which was in the form of a rod with continuous fibres running along its axis, the same as composite 1. The volume percent of fibre in the composite was 61%. Other information about the material is given in Section 4.2. This composite did not show much evidence of degradation of material properties due to thermal fatigue in the axial direction, but there was good indication of damage perpendicular to the fibre direction.

Measurements performed on composite 2 included measurements of absolute velocity and attenuation in an unfatigued state, as well as changes in velocity and attenuation due to thermal fatigue. Ultrasonic measurements were performed using longitudinal waves either parallel to the fibre axis or perpendicular, using frequencies from 3.00MHz to 5.00MHz.

5.3.1 Determination of Ultrasonic Velocity and Attenuation

The values of absolute ultrasonic velocity v_f and attenuation α_f were determined for composite 2 as described in Section 5.2.1. The graphs used for the calculations are shown in Figures 5.16 and 5.17, with values summarized in Table 5.2.

Absolute velocity is given by the slope of a plot of transit time versus specimen length. Absolute attenuation is given by the y-axis intercept of a plot of measured attenuation versus inverse of the path length. The assumption of a consistent boundary layer effects can be evaluated by the fit of the data to a linear relationship: if

this assumption is good, the data should be linear. Table 5.2 summarizes the absolute velocity and attenuation measurements for composite 2.

Table 5.2 Absolute velocity and attenuation values for composite 2 (unfatigued).

excitation frequency (MHz)	velocity (m/sec)	correlation coefficient of linear fit	attenuation coefficient (1/m)	correlation coefficient of linear fit
3.00	7895 ± 154	0.9987	159 ± 40	0.9917
4.00	7962 ± 148	0.9988	298 ± 46	0.9868
5.00	7968 ± 148	0.9988	524 ± 20	0.9968

For Table 5.2, errors given are estimates of the standard deviation of the value. Regressions were performed by the software package Sigma Plot version 5.0. The data was fit to a linear relationship.

As mentioned in Section 3.2.1, the velocity is shown to be independent of frequency within the error of the measurements. Correlation coefficients of the velocity data indicate that the assumption of consistent bond quality is valid. The values for attenuation coefficients increase with frequency as was expected. Again the correlation coefficients of the attenuation data indicate that the assumption of consistent bond quality is valid.

The velocity measured here corresponds to v_1 in Equation 2.33, and with a density of 1260 kg m^{-3} for composite 2, c_{11} is found to be 12.6GPa.

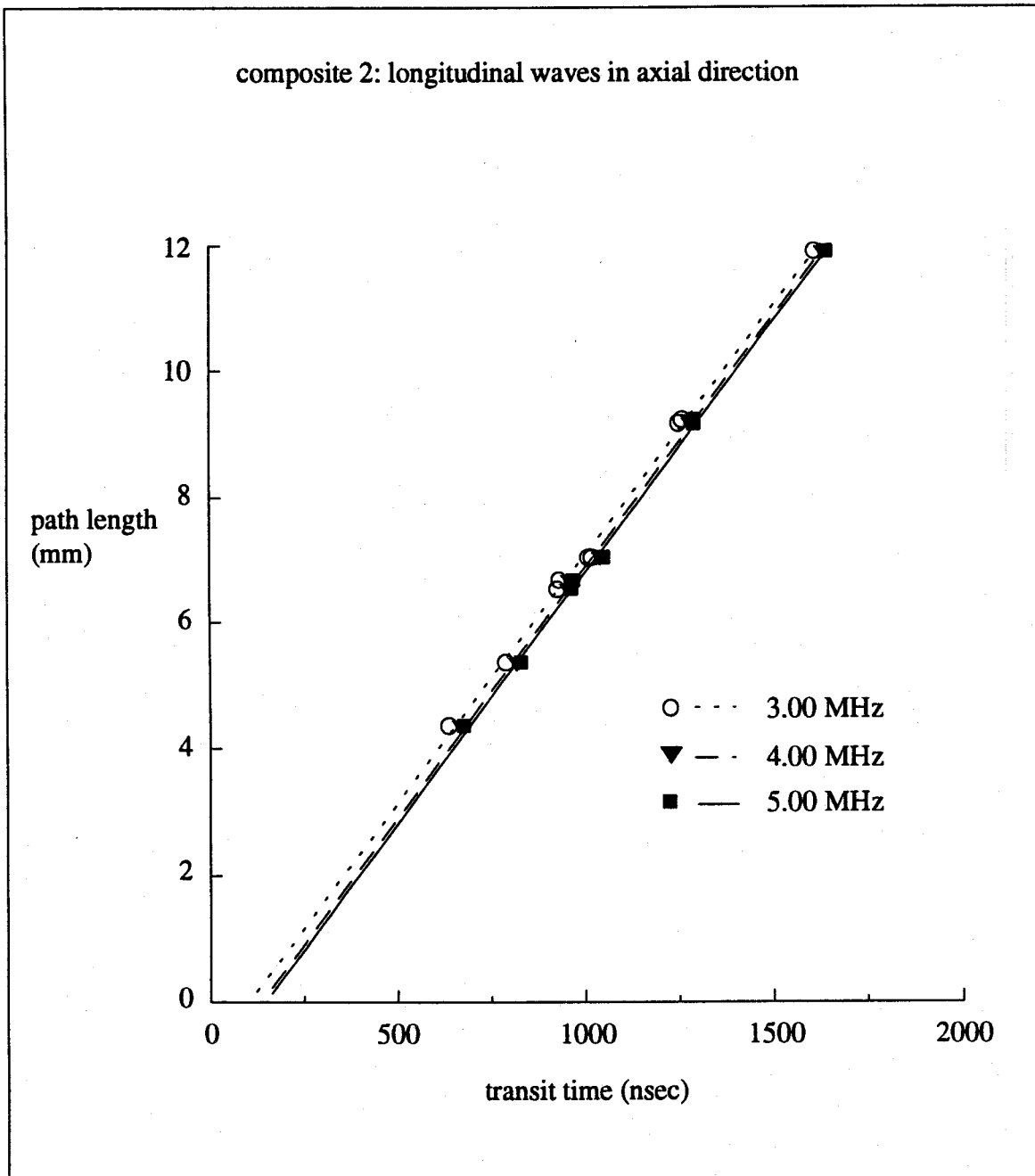


Fig. 5.16 Dependence of transit time on specimen length. (Graph used for determination of v_l for composite 2.)

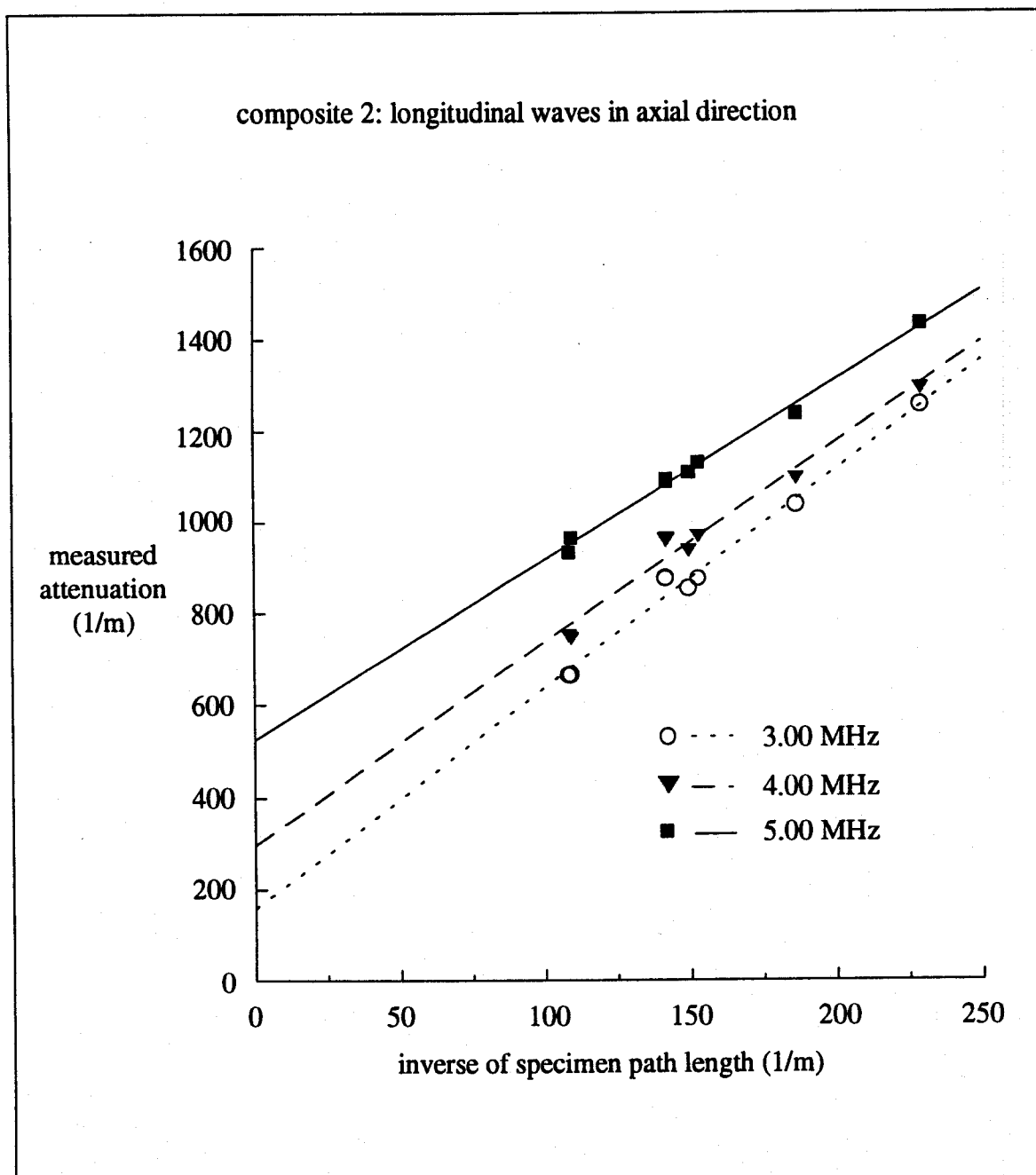


Fig. 5.17 Dependence of attenuation on specimen length. (Graph used for determination of α_l for composite 2.)

5.3.2 Ultrasonic Waves Perpendicular to the Fibre Axis (Composite 2)

The material properties perpendicular to the fibre axis are less influenced by the fibres. Ultrasonic velocities are lower, and attenuations higher. Much smaller path lengths were used for these experiments than for axial mode measurements, due to the specimen geometry and attenuation. The very high attenuation of composite 2 made accurate measurements very difficult to achieve. Absolute measurements of ultrasonic velocity or attenuation perpendicular to the fibre axis were not made.

Figure 5.18 shows a graph of the attenuation and velocity data for these specimens in thermal cycle 2. Two specimens provided the data. Specimen lengths were 2.05 ± 0.2 mm.

It was found that ultrasonic attenuation increased and ultrasonic velocity decreased as the number of thermal cycles increased. The magnitude of the velocity decrease and of the attenuation increase were independent of frequency. Scatter in this data makes it difficult to give conclusive interpretations. The very short path lengths and the high attenuation which made them necessary are the main causes of this uncertainty.

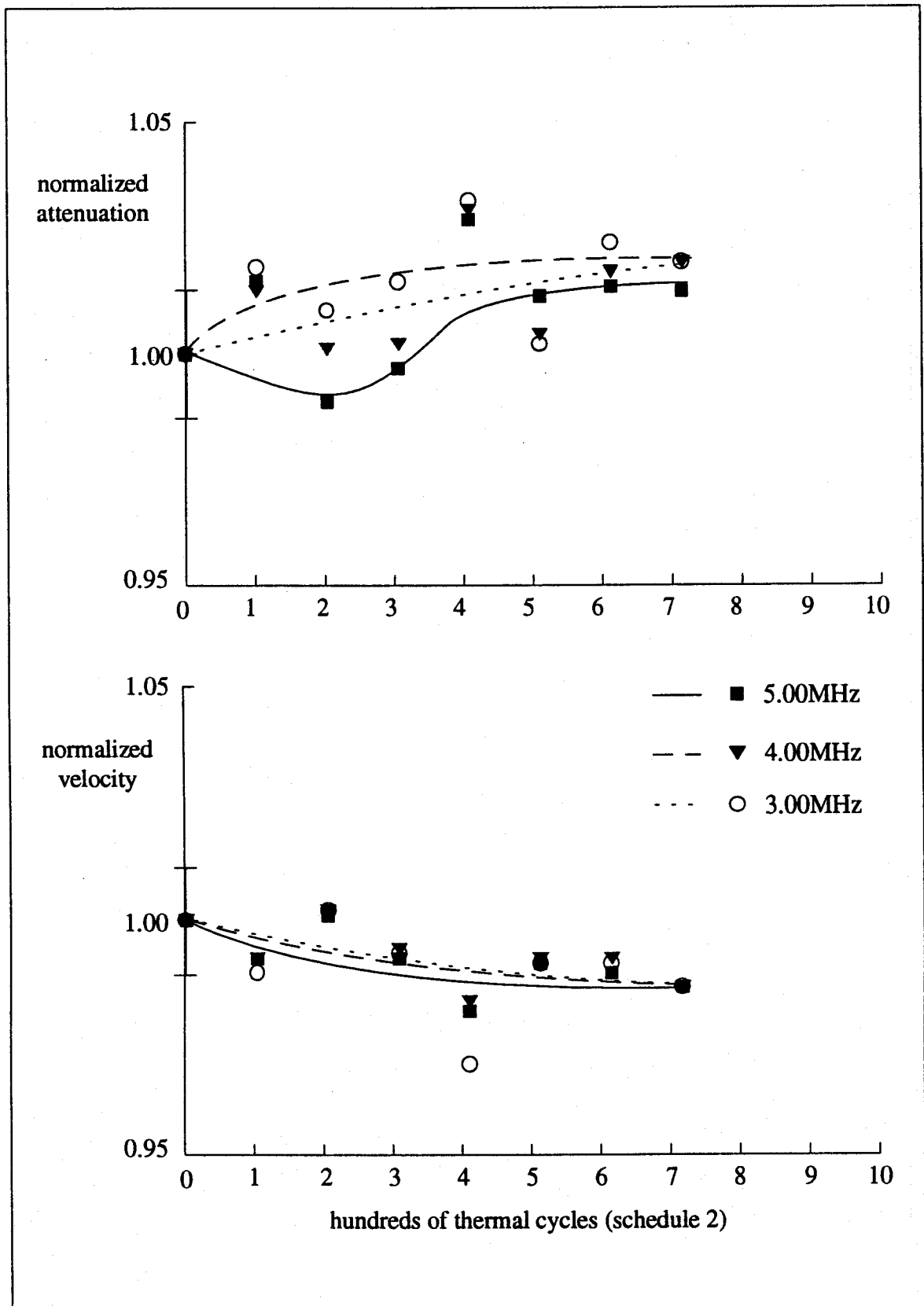


Fig. 5.18 Graph of velocity and attenuation changes for composite 2: longitudinal wave perpendicular to fibre axis (thermal cycle schedule 2).

SEM examination of composite 2 in the plane parallel to the fibre also indicated damage after thermal fatiguing. Figure 5.19 shows an unfatigued specimen. The surface is very smooth. Figure 5.21 shows the same specimen after 500 cycles (schedule 1), and the surface now shows a great deal of matrix cracking. Figure 5.20 shows the unfatigued material near the edge of the specimen, with visible fibre ends. A photograph of a specimen after 500 fatigue cycles is shown in Figure 5.22, and there appears to be a fibre pulled out and matrix cracking as well. Figures 5.23 and 5.24 show fibre ends in a fatigued specimen (1000 cycles, schedule 2) that have pulled out of the matrix and curled up.

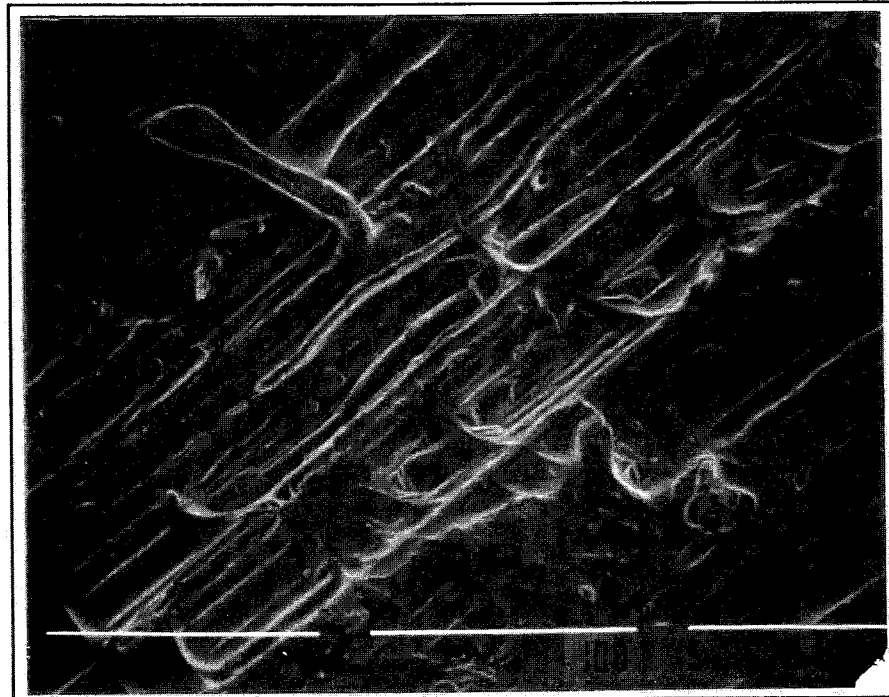


Fig. 5.19 SEM photograph of composite 2, unfatigued at 350 \times magnification.



Fig. 5.20 SEM photograph of composite 2, unfatigued at 1500 \times magnification. Note fibre ends at edge of specimen (see Figures 5.23, 5.24).



Fig. 5.21 SEM photograph of composite 2, after 500 cycles (schedule 1) at 200× magnification. Note matrix cracking at surface.

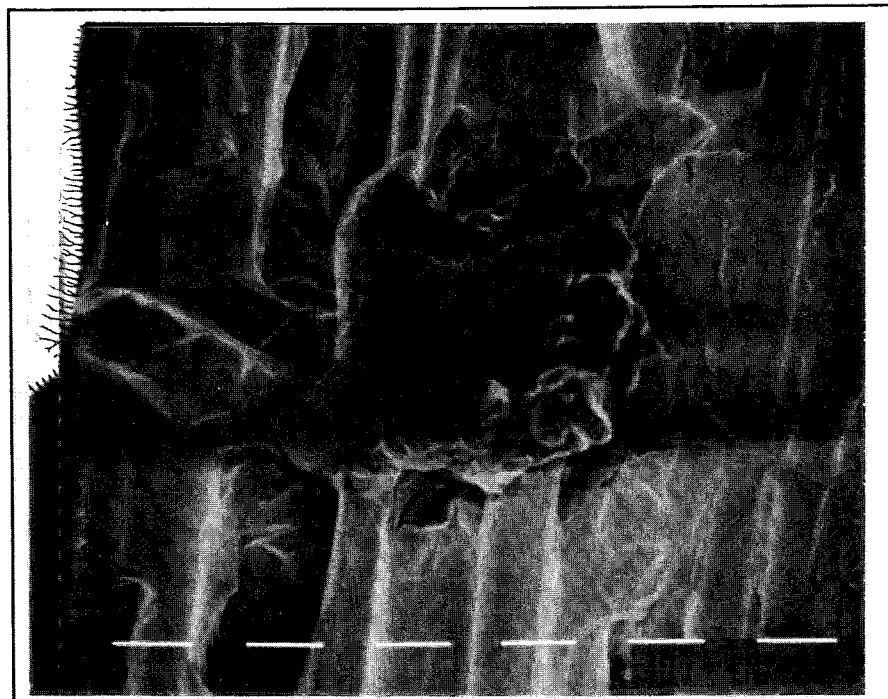


Fig. 5.22 SEM photograph of composite 2 at 1000× magnification, after 500 cycles (schedule 1). Note fibre pullout.

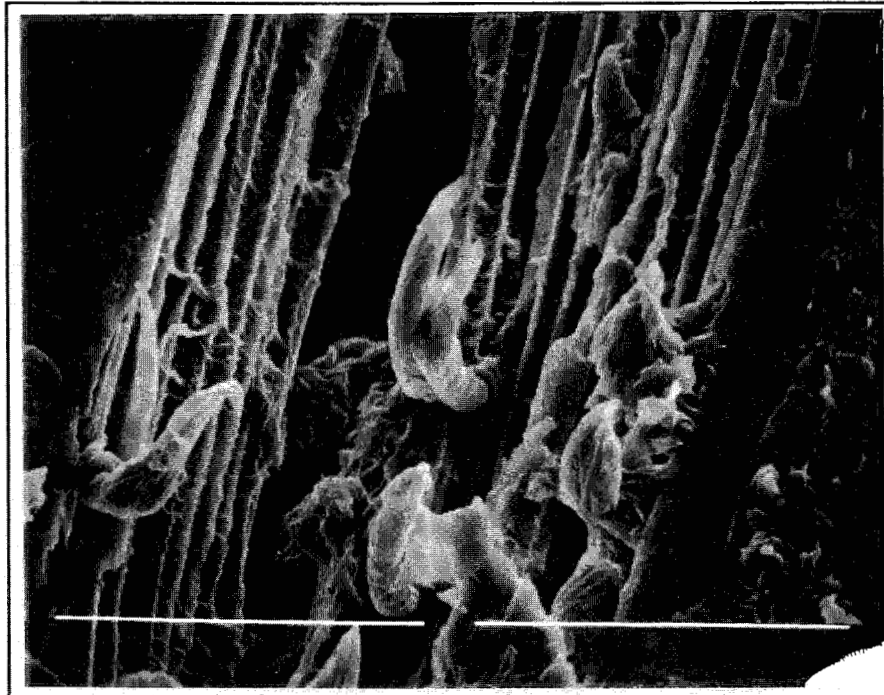


Fig. 5.23 SEM photograph of composite 2 at 500× magnification, after 1000 cycles (schedule 2). Note fibres pulled out from matrix.

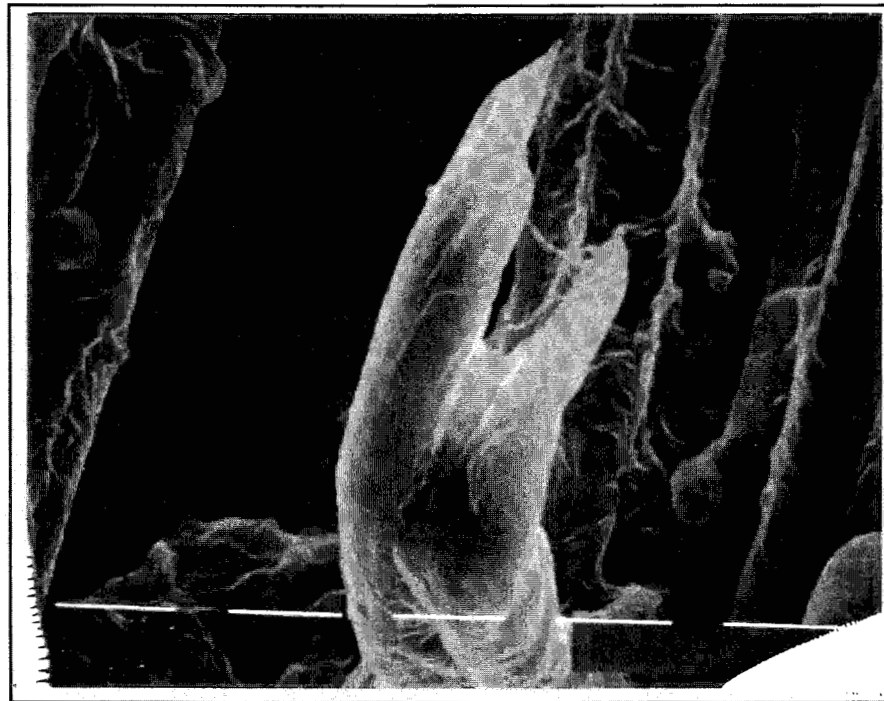


Fig. 5.24 SEM photograph of composite 2: same view as Figure 5.23, at 1500× magnification.

5.3.3 Ultrasonic Waves Parallel to the Fibre Axis (Composite 2)

The change in properties of composite 2 along the fibre axis were examined using thermal cycle schedule 2, and Figure 5.25 shows the results. The longitudinal velocity does not vary more than 0.5% from the unfatigued state at any time. Attenuation increases for the 3.00 and 4.00MHz measurements, but not the 5.00MHz. Specimen lengths for these measurements were 9.2 ± 0.1 mm. Two individual specimens were evaluated.

SEM examination of composite 2 in the plane perpendicular to the fibre axis was also somewhat inconclusive. It is difficult to obtain good contrast between fibre and matrix in this material and for composite 3 as well, due to the similarity in electrical properties of the fibre with the matrix material, both being polymers.

Figures 5.26 and 5.28 show unfatigued specimens of composite 2. Figures 5.27 and 5.29 show fatigued specimens, Figure 5.27 after 1000 cycles (schedule 2) showing surface damage, perhaps due to fibre pullout at the ends. Figure 5.29 after 800 cycles (schedule 1) appears little different from Figure 5.28.

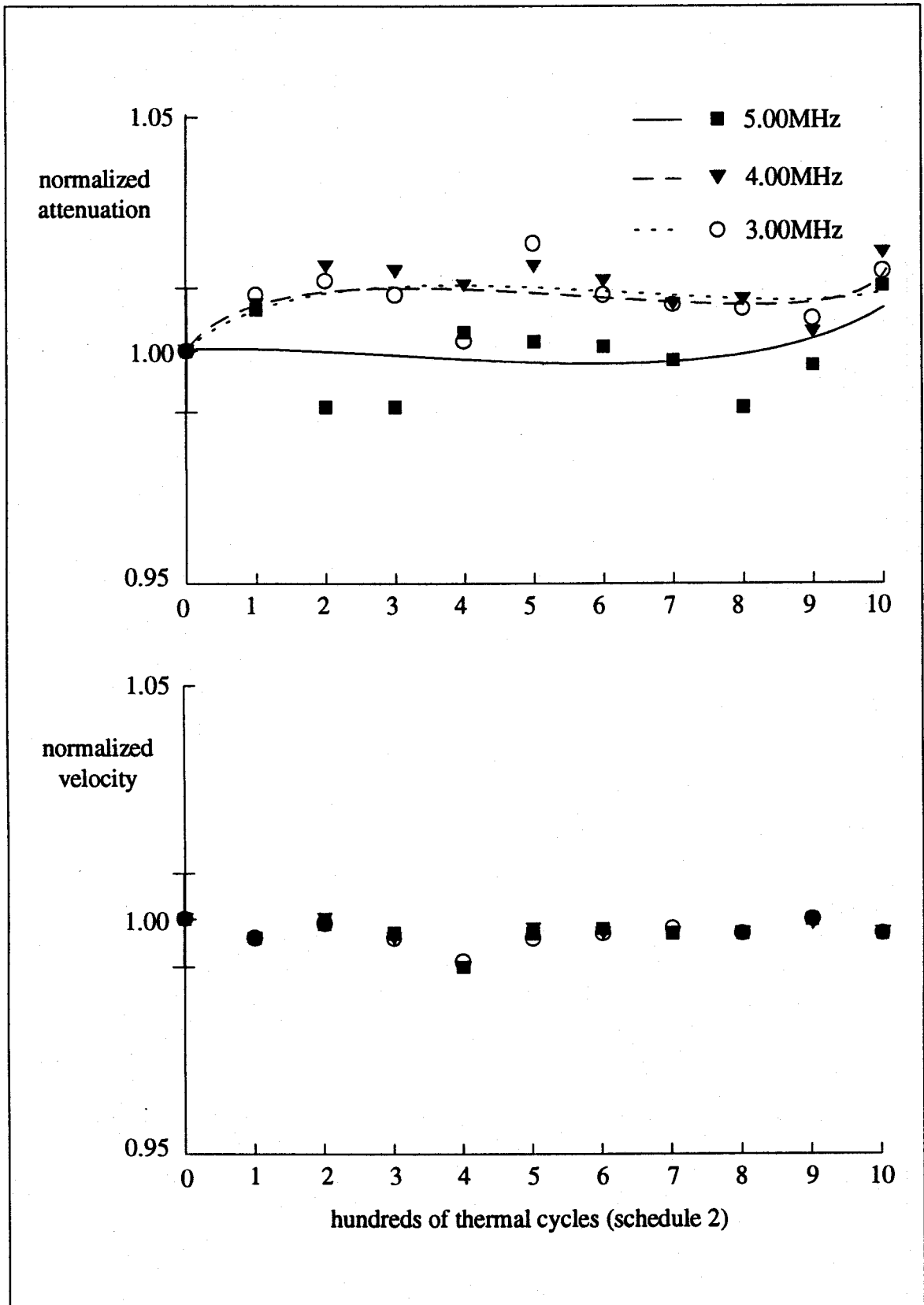


Fig. 5.25 Graph of velocity and attenuation changes for composite 2: longitudinal wave parallel to fibre axis (thermal cycle schedule 2).

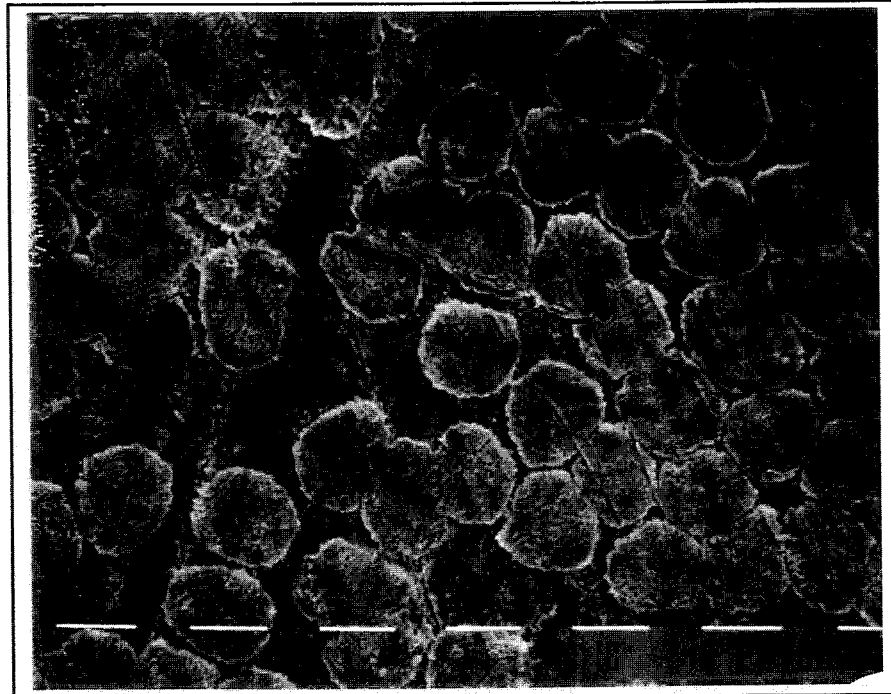


Fig. 5.26 SEM photograph of composite 2 unfatigued at 1000× magnification.

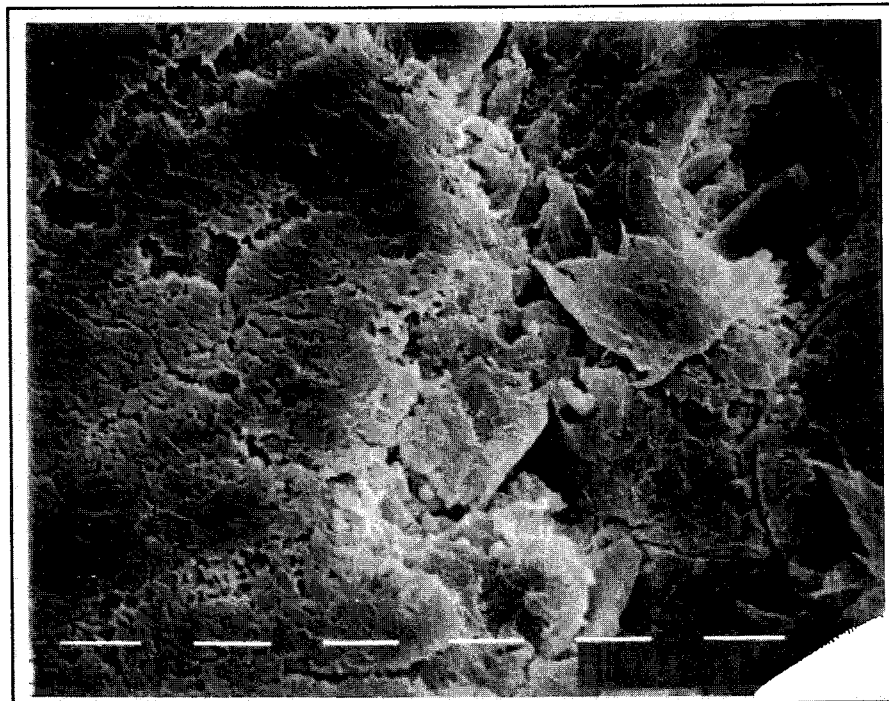


Fig. 5.27 SEM photograph of composite 2 after 1000 cycles (schedule 2) at 1000× magnification.

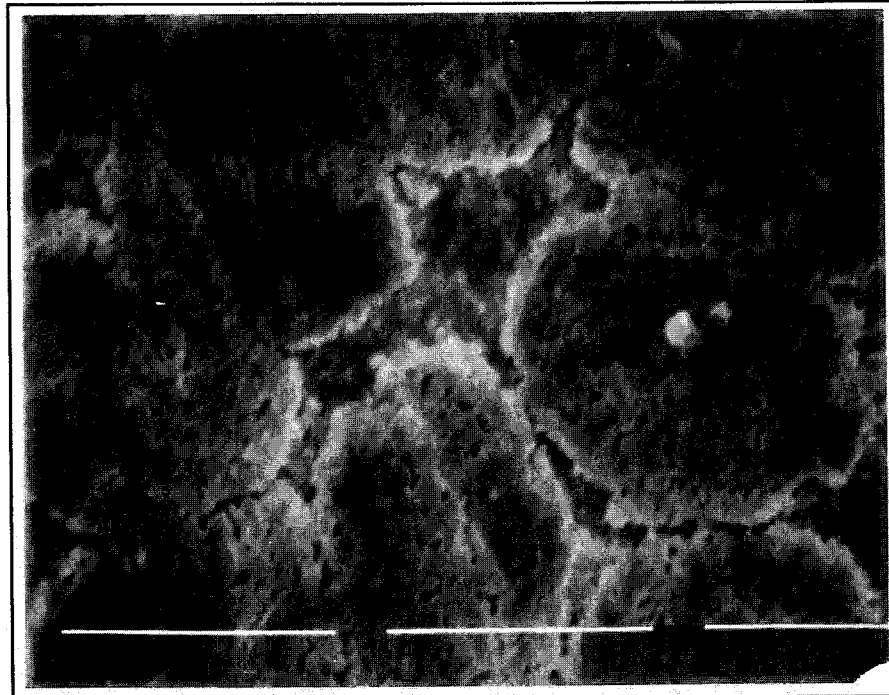


Fig. 5.28 SEM photograph of composite 2 unfatigued at 3500 \times magnification.

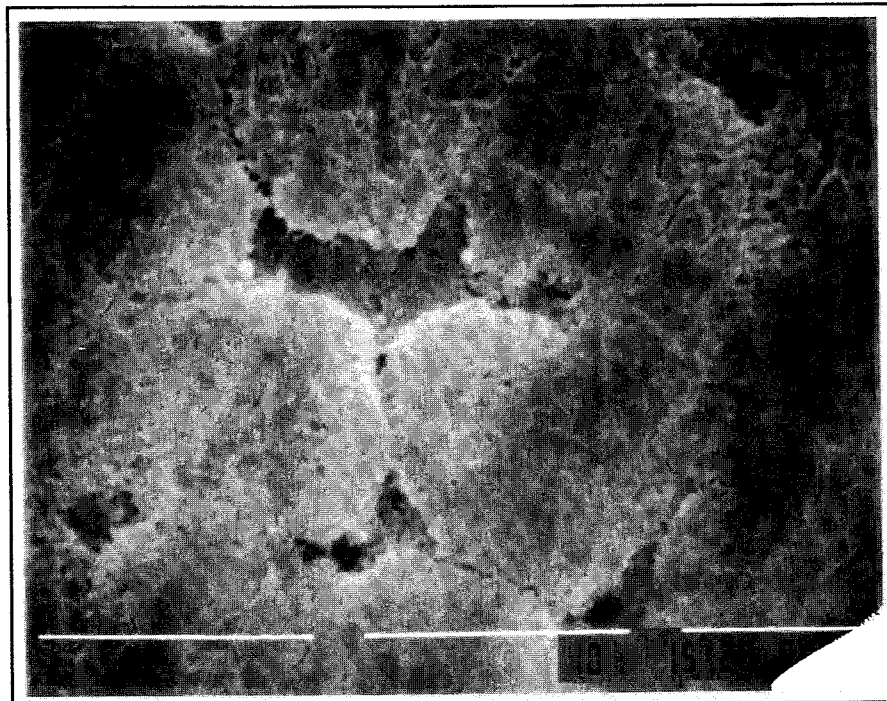


Fig. 5.29 SEM photograph of composite 2, after 800 cycles (schedule 1) at 3500 \times magnification.

5.4 Composite 3: Aramid Fibres in Polyphenylene Sulphide

Composite 3 is a mixture of randomly oriented aramid fibres in a polyphenylene sulphide (PPS) matrix. This composite is isotropic on a macroscopic scale. The fibre volume fraction of the composite is 30%, as determined by image analysis and density measurements. This composite is not as stiff as the pultruded composites are (in their axial direction), and the modulus of the composite is not as much influenced by the fibre, due to the lower fibre fraction and the geometric arrangement of the fibre.

5.4.1 Determination of Absolute Velocity and Attenuation

The values of absolute ultrasonic velocity v and attenuation α were determined for composite 3 as described in Section 5.2.1. The graphs used for the calculations are shown in Figures 5.30 and 5.31, with values summarized in Table 5.3.

Absolute velocity is given by the slope of a plot of transit time versus specimen length. Absolute attenuation is given by the y-axis intercept of a plot of measured attenuation versus inverse of the path length. The assumption of a consistent boundary layer effects can be evaluated by the fit of the data to a linear relationship: if this assumption is good, the data should be linear. Table 5.3 summarizes the absolute velocity and attenuation measurements for composite 3.

For Table 5.3, errors given are estimates of the standard deviation of the value. Regressions were performed by the software package Sigma Plot version 5.0. The data

Table 5.3 Absolute velocity and attenuation values for composite 3 (unfatigued).

excitation frequency (MHz)	velocity (m/sec)	correlation coefficient of linear fit	attenuation (1/m)	correlation coefficient of linear fit
3.00	2566 ± 44	0.9993	185 ± 11	0.9941
4.00	2564 ± 43	0.9993	273 ± 65	0.9974
5.00	2564 ± 48	0.9991	355 ± 44	0.9988

was fit to a linear relationship.

As mentioned in Section 3.2.1, the velocity is shown to be independent of frequency within the error of the measurements. Correlation coefficients for velocity and attenuation data indicate that the assumption of consistent bond quality is valid.

The values for attenuation coefficients increase with frequency as was expected.

The velocity measured here corresponds to v_x in Equation 2.30, and with a density of 1380 kg m^{-3} for composite 3, c_{xx} is found to be 4.88GPa.

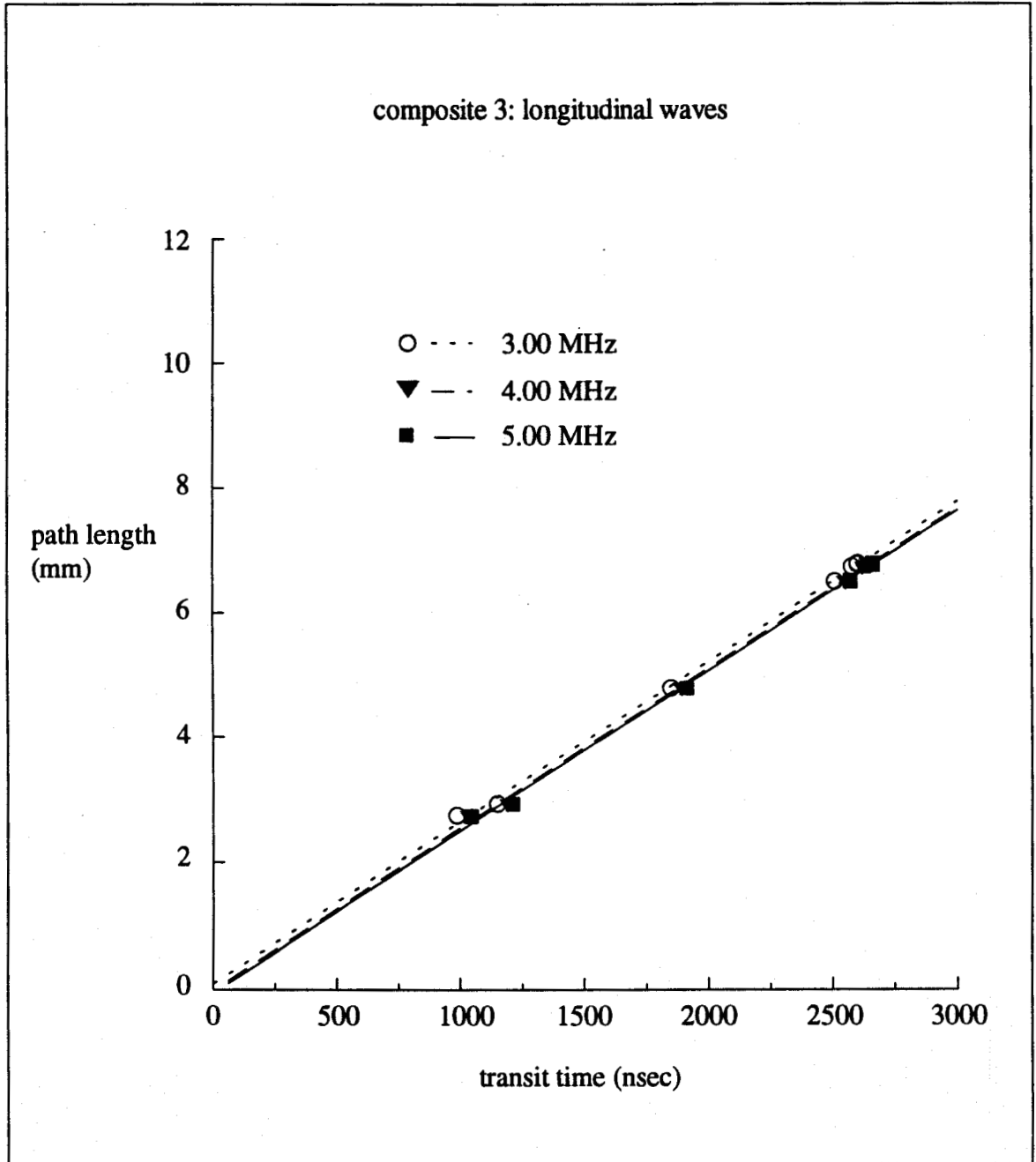


Fig. 5.30 Dependence of transit time on specimen length. (Graph for determination of absolute velocity for composite 3.)

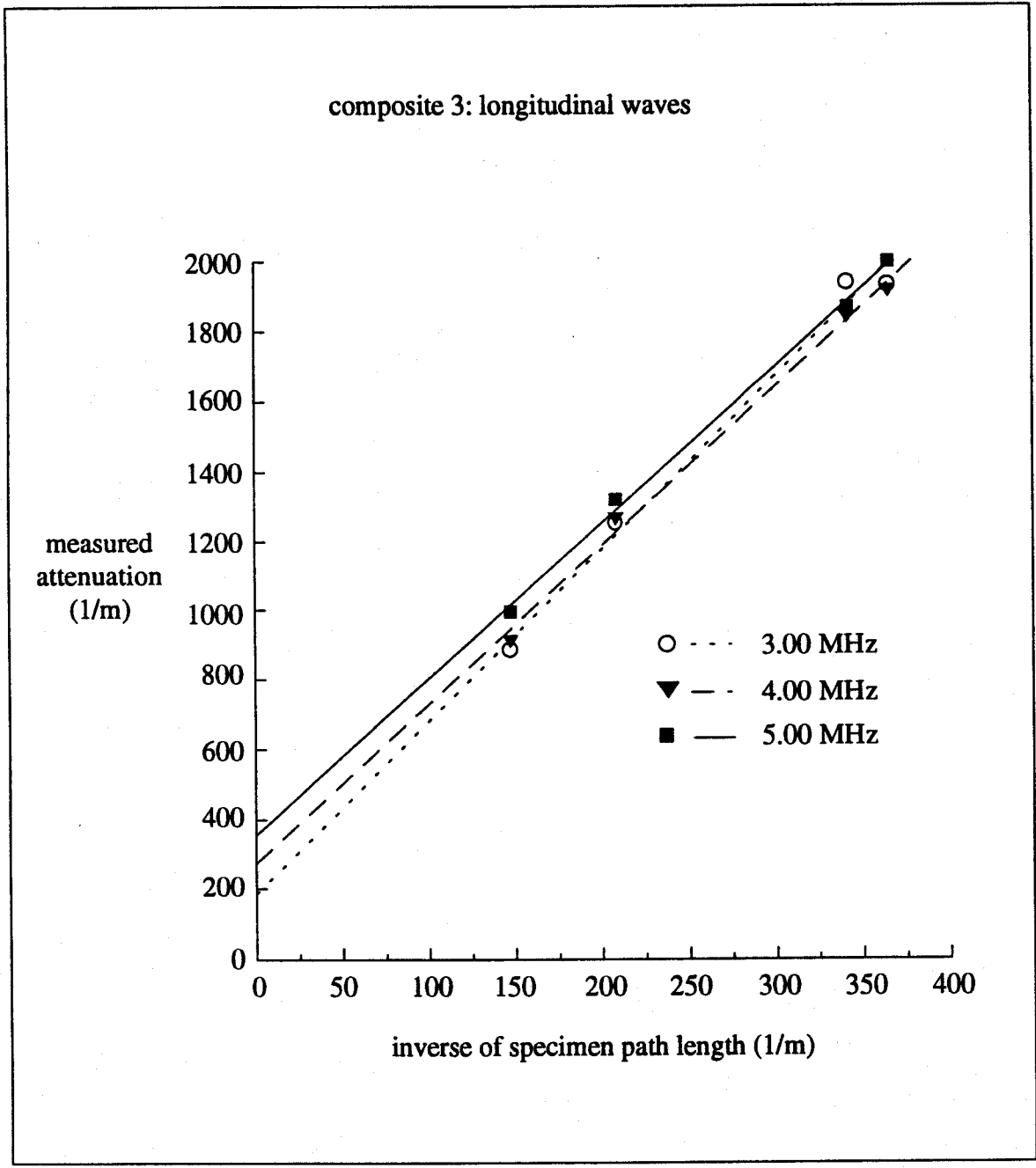


Fig. 5.31 Dependence of attenuation on specimen length. (Graph for determination of absolute attenuation for composite 3.)

5.4.2 Ultrasonic Waves in Composite 3

Composite 3 was in the form of a plate, and four specimens of path length between 6.50mm and 7.00mm were examined using thermal cycle schedule 1. Attenuation increased and velocity decreased slightly with increasing thermal cycles. Attenuation also increased with increasing frequency, while velocity changes showed no frequency dependence. Figure 5.32 shows plots of the attenuation and velocity changes with thermal cycling.

SEM examination of composite 3 showed evidence of fibre-matrix debonding after thermal cycling. There was little matrix cracking observed. Figure 5.33 shows an unfatigued specimen. The bright areas are where the fibres reach the surface. Figure 5.34 shows a view of a fibre, running vertically in the centre of the photo. Figures 5.35 and 5.36 show a specimen after 1000 cycles (schedule 2). Both show fibre ends pulled away from the matrix.

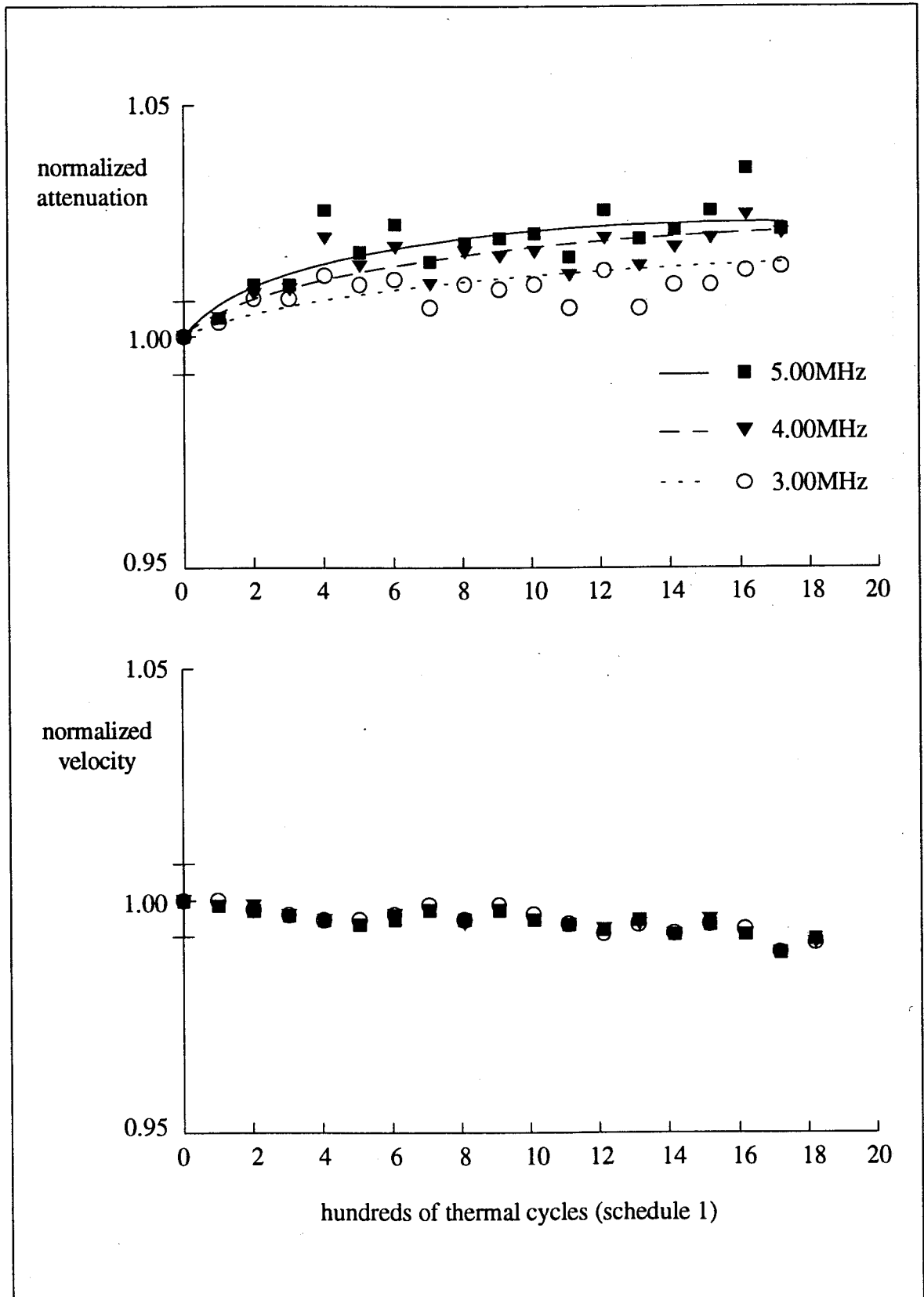


Fig. 5.32 Graph of velocity and attenuation changes for composite 3: longitudinal wave in random fibre orientation (thermal cycle schedule 1).

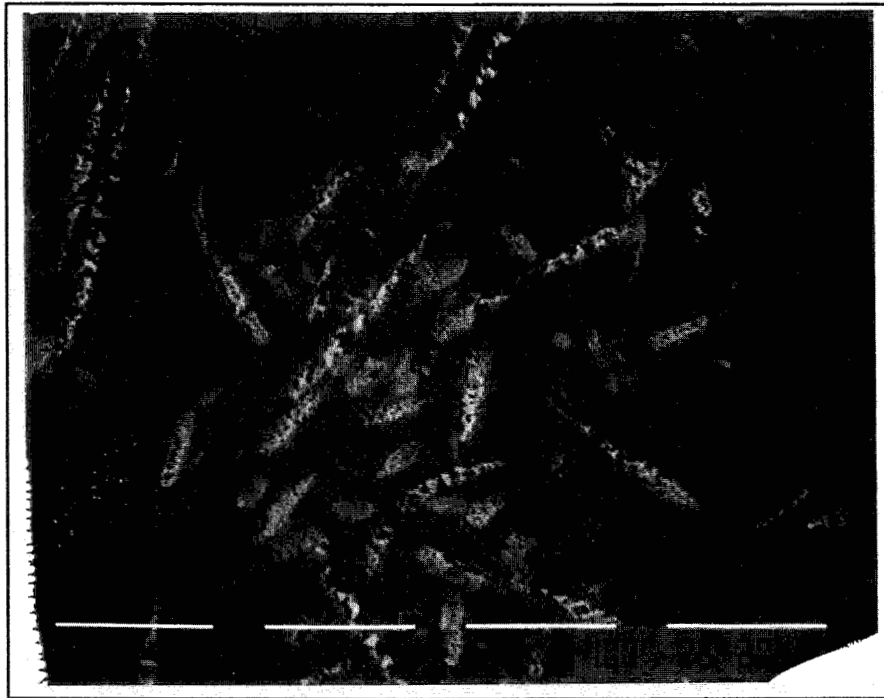


Fig. 5.33 SEM photograph of composite 3 at 200x magnification, unfatigued.

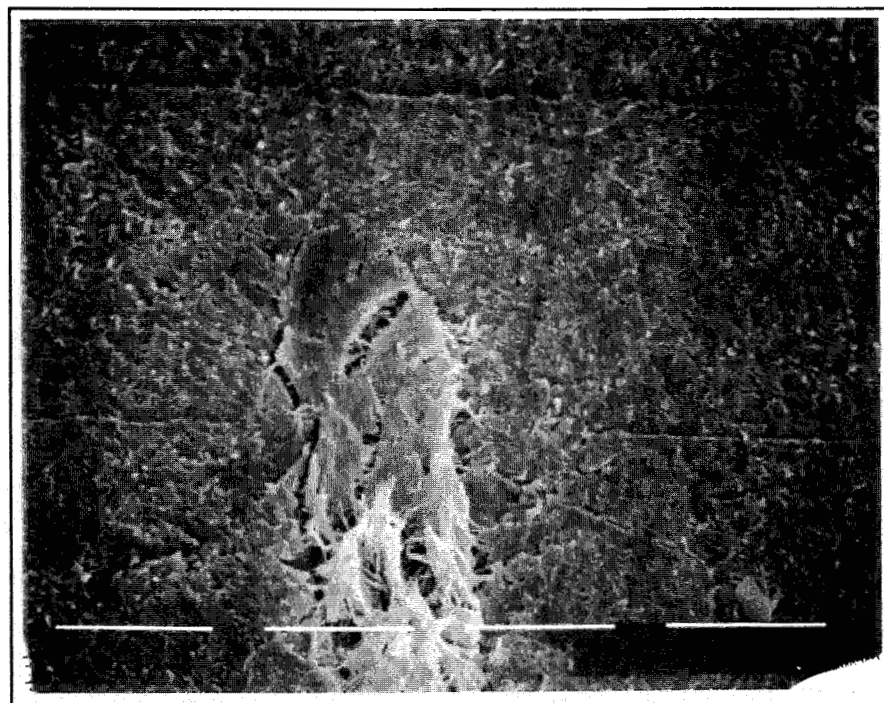


Fig. 5.34 SEM photograph of composite 3 at 2000x magnification, unfatigued.

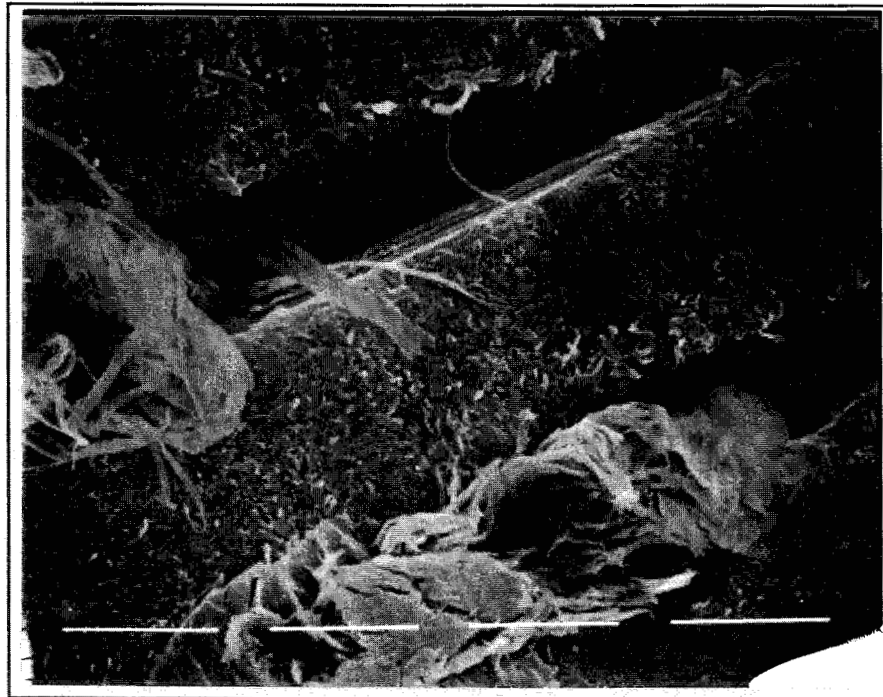


Fig. 5.35 SEM photograph of composite 3, after 1000 cycles (schedule 2), at 2000 \times magnification. Note fibre pullout.

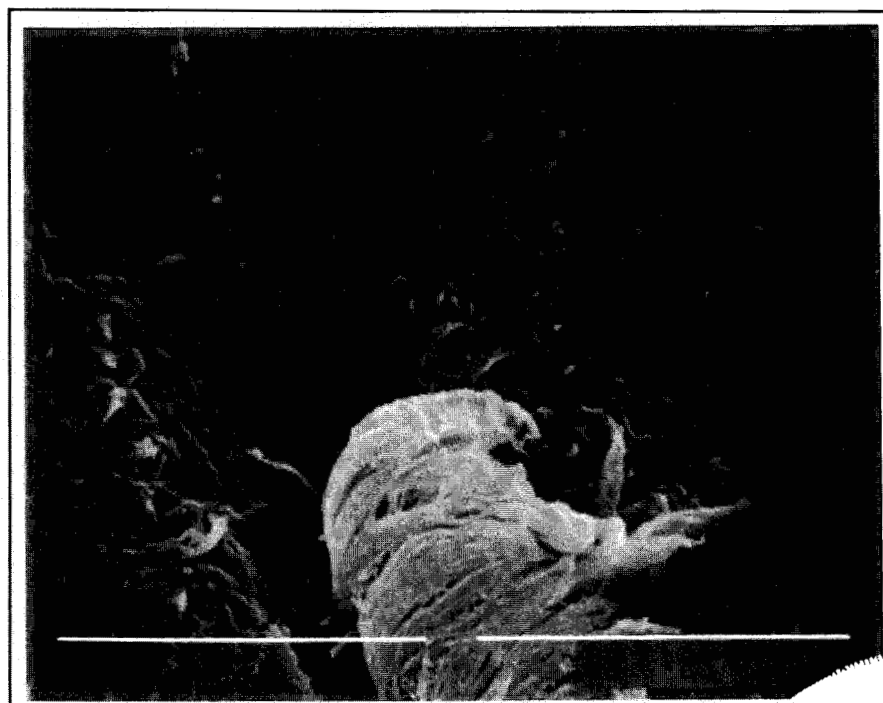


Fig. 5.36 SEM photograph of composite 3, after 1000 cycles (schedule 2), at 3500 \times magnification. Again note separation of fibre from matrix.

5.5 Discussion

The measurements described in this chapter were performed to examine the ability of the ultrasonic test system developed in this work to evaluate thermal fatigue damage in systems of two or more macroscopically distinct components. Three polymer matrix fibre composites were examined for changes in ultrasonic velocity and attenuation as they were thermally fatigued, and scanning electron microscopy was used as an additional qualitative tool to obtain evidence of visual damage after cycling. Table 5.4 summarizes the materials examined.

The thermal cycling has been described in Sections 4.3 and 5.1. Although two different schedules were used, it was found that the effective temperature ranges in the specimens were only slightly different. Where similar specimens were evaluated with both schedules, no significant difference in damage was found.

Table 5.4 A summary of the materials examined.

material	matrix	filler	fibre geometry
composite 1	vinylester	carbon fibres, 50% by volume	continuous axial
composite 2	vinylester	aramid fibres, 61% by volume	continuous axial
composite 3	polyphenylene sulphide (PPS)	aramid fibres, 30% by volume	random

When FRP (fibre reinforced polymer) composites are manufactured, the fibres are combined with the matrix material at high temperatures where the matrix is a viscous liquid. This means that the actual thermal stress equilibrium temperature is at

the point where the matrix begins to solidify. This is called the cure temperature[25], and interfacial stresses are proportional to the difference in temperature from this point[25, 26] (see Appendix A). Therefore at room temperature, there is already a level of interfacial stress due to thermal expansion mismatch, and this will increase with cooling and decrease with heating from room temperature towards the cure temperature. It can be seen from the plot in Figure 5.1 that after four minutes, the cooling rate is very small and little additional decrease in specimen temperature occurs. This explains the similarity in effect of the two different thermal cycling schedules.

All of the materials examined showed some evidence of damage due to thermal fatigue. Composite 1 was the most affected. Perpendicular to the fibre axis, ultrasonic velocity decreased and attenuation increased (see Figures 5.5 and 5.6). Parallel to the fibres, attenuation increased but velocity showed no change (see Figure 5.11). Models of interfacial stress indicate the highest stress levels at the ends of the specimens[25, 26] (see Appendix A), and if this is the case a highly damaged surface layer should be expected on the specimens after thermal fatigue cycling, with damage decreasing towards the centre.

The specimens of composite 1 examined for axial change were cylindrical and all within 1mm of 15mm length. The increase in attenuation without velocity change seems to indicate a surface layer change that does not affect the bulk properties (especially elastic moduli along the axis) of the specimens. SEM photographs also indicate fibre pullout at these faces, which would create a surface layer of different

acoustical properties. This increases scattering[30], and causes the increase in attenuation that is observed. This damaged layer is likely to be very thin in the direction of wave propagation, (see Appendix A), and thus insignificant mechanically. This explains the insensitivity of ultrasonic velocity to the damage.

Stress relaxation due to end pullout reduces the effect of further cycling, as shown in the decrease in attenuation change after the initial jump in all materials examined. It seems obvious that the regions of highest interfacial stress move down the fibre to the regions which border the detached area, but the problem is not equivalent to that of the undamaged material, and it is likely that these stresses are smaller than the stresses on the unfatigued specimen interfaces. For all materials examined here, it was found that rates of accumulated damage were initially very high but quickly slowed. This is in agreement with observations of Kasap, Mirchandani, Yannacopoulos, and Hildebrandt[27]; and Hartung[6].

Perpendicular to the fibre direction, composites 1 and 2 showed increased attenuation and decreased velocity (Figures 5.5-6, 5.18). SEM examination also showed evidence of damage (Figures 5.7-10, 5.19-23). Matrix cracking and fibre detachment from the matrix appear to be the main mechanisms of damage, similar to observations made on e-glass reinforced composites by Yannacopoulos, Hildebrandt, and Kasap[29]. The causes of increased attenuation are likely the same as for the previous case, with a surface layer that is cracked and contains even broken fibres.

The velocity decrease may be due to the fact that the path length for these specimens was much smaller than for the axial specimens, due to specimen geometry

and attenuation. The weakened layer may be significant in size. Although measurements of absolute velocity perpendicular to fibre direction were not made as for in the fibre direction, the author estimates these to be about 2600m/s for composite 1 and 2000m/s for composite 2. These values are about a factor of four smaller than the velocities in the fibre direction. It is somewhat surprising that there is a more measurable change in velocity in these specimens, as the fibre is not as important for the elastic moduli in this direction.

Due to the very high attenuation perpendicular to fibre axis in composite 2, it was very difficult to evaluate properties in this direction. Specimens had to be cut with very small path lengths, and relative errors in measurement become much larger. SEM results did indicate that these specimens were damaged by thermal cycling. For more confidence in the measurement of damage (perpendicular to fibre direction) in composite 2, more specimens should be examined.

In the fibre direction, composite 2 showed little degradation of properties due to thermal fatigue in ultrasonic examination, and only inconclusive evidence was found using SEM. The geometric arrangement of composite 2 is the same as composite 1, and the fibre contents are similar (61% for composite 2 versus 50%). Two important physical differences are that the aramid fibre is much less thermally conductive (see Table 4.1), and much less brittle: the manufacturer specifies elongation to failure for carbon fibres of 0.7 to 1.5%, and 2.5% for the aramid fibres. Models of interfacial stress (Appendix A) give very similar estimates of stress at fibre ends for composites 1 and 2: 593kPa for composite 1 and 612kPa for composite 2.

The large difference in thermal conductivity between the carbon fibres (about $50 \text{ Wm}^{-1}\text{K}^{-1}$) and the matrix material (about $0.2 \text{ Wm}^{-1}\text{K}^{-1}$) may give rise to thermal gradients in the direction perpendicular to the fibre axes. The fibres will heat much quicker than the surrounding matrix, but it is very difficult to estimate the actual size of these gradients. This may contribute to debonding at the fibre-matrix interface, and matrix microcracking as well. The aramid fibre composites have slightly smaller thermal conductivities than the matrix materials, which would create much smaller thermal gradients than carbon fibres.

One factor that was not evaluated here was the quality of the bonding between the fibres and the matrix material. The bond may have very different characteristics for the different fibre types, and can range from purely mechanical to mostly chemical [5, 23, 25]. There may be different bonding mechanisms acting for the different composites, and this may result in different bonding strengths. The sizes of specimens used resulted in similar temperature ranges across the specimens, despite thermal conductivity differences. The difference between performance of composites 1 and 2 may be partially due to the characteristics of the fibre-matrix bond.

Some attenuation increase was found for composite 2 in the fibre direction at the test frequencies of 3.00MHz and 4.00MHz, but not at 5.00MHz. This was the only case where the higher frequency or shorter wavelength was not more sensitive to defects. The magnitudes of received voltages for the 5.00MHz measurements were very small (1mV compared to 10-20mV for 3.00MHz and 4.00MHz), and the relative error much larger. This may have resulted in the lack of measurable change in

attenuation at 5.00MHz.

Composite 3 was a mixture of polyphenylene sulphide (PPS) matrix material with randomly oriented aramid fibres. Attenuation increased and velocity decreased with increasing thermal cycles, as shown in Figure 5.32. The magnitude of the velocity change was very small. SEM examination of this material showed detachment of fibre ends from the matrix after cycling (see Figures 5.33-36), with no visible matrix cracking.

It is impossible to calculate the interfacial stresses without knowing the geometric arrangement of fibres in the material. They will depend on the difference between the cure temperature and material temperature, on the size and spacing of fibres, and on the distance from the fibre ends. The fibre content is 30% by volume, and the velocity of propagation is a relatively modest 2564m/sec (at 5MHz). This implies that the mechanical properties of composite 3 are not as dependent on fibre as the other composites, due to the low fibre volume.

The mechanisms of damage for composite 3 appear to be debonding of fibres from the matrix material, especially at fibre ends, where stress concentrations are going to be largest (see Figures 5.33-36). This creates scattering centres for ultrasound, leading to increased attenuation. Even after 1800 cycles the velocity decrease is very small, less than 1%. This demonstrates that the debonding is not occurring over a significant interface area.

6. CONCLUSIONS AND RECOMMENDATIONS

FOR FUTURE WORK

6.1 Conclusions

In this work, an ultrasonic based testing system has been utilized for the evaluation of thermal fatigue damage in material systems of more than one macroscopically distinct component. The system was designed, built, and tested on three types of fibre-reinforced plastics (FRP).

Sound propagation in a medium reflects the mechanical characteristics of the medium, and as such changes in mechanical properties due to thermal fatigue are expected to be exhibited in changes in sound propagation. Therefore the test system was designed to evaluate changes in ultrasonic velocity and attenuation. Scanning electron microscopy (SEM) was used as an additional qualitative tool for the identification of thermal fatigue effects.

Three fibre-reinforced plastics were evaluated for thermal fatigue damage, being cycled from -25C to 75C up to 1800 cycles. Evidence of thermal fatigue damage was shown most dramatically by attenuation measurements, with higher frequencies showing greater change. Measurements also indicated decreased ultrasonic velocities in some cases. SEM examinations showed two main damage mechanisms, debonding of fibres from the matrix material and cracking of the matrix material. Some fibre breakage was also found.

Quantitatively the findings of thermal fatigue damage in the composites studied can not be easily generalized. However, the failure modes of the composites are

consistent with studies done on other composites, where debonding at the interface and matrix cracking are the dominant mechanisms[8, 9, 27-29]. These defects create scattering centres which scatter energy away from the direction of propagation, causing an increase in measured attenuation[30]. These findings are useful because they demonstrate the applicability of ultrasonic NDT to the evaluation of thermal fatigue effects in material systems.

In summary, an ultrasonic test system has been evaluated for use in detecting thermal fatigue damage in composite materials. It was found that ultrasonic attenuation is sensitive to thermal fatigue damage. Ultrasonic velocity is not very sensitive to thermal fatigue damage, and may not be a useful tool for the investigation of thermal fatigue. SEM studies of the fatigued materials indicated damage was mostly fibre-matrix debonding, and some matrix cracking.

As the use of composite materials increases and is broadened to include more critical applications it will be necessary to better understand the problem of thermal fatigue. The problem of two materials with different thermal expansion coefficients is common to FRP's, metal-ceramic composites, and to systems such as soldered joints, plastic-die interfaces, and bonded joints between materials[7-9, 31-34]. Ultrasonic testing is an effective tool for NDT of these systems in many cases.

6.2 Recommendations for Future Work

In this work, longitudinal ultrasonic waves of frequencies between 3.00MHz

and 5.00MHz were used for studying the test materials. Additional information about the mechanical characteristics of materials can be gained by the use of shear waves. Surface waves are also commonly used to evaluate bonds or joints in materials[31, 35]. The main difficulties in using shear and surface waves are the coupling of the waves into the specimen, and the high attenuations of composite systems. For many of the electronics problems of thermal fatigue, the actual components are very small, requiring the use of very high frequencies which are highly attenuated, and of smaller transducers, which are difficult physically to use.

For the study of the FRP's as described in Chapter 5, additional benefit could possibly have derived from the use of shear waves in addition to longitudinal, using higher test frequencies, and in some cases additional specimens to provide more reliable data. A high power RF amplifier and higher frequency transducers together may benefit the study of these composites, although the cost of the test system is dramatically increased.

The design of appropriate test specimens for systems such as solder joints and multilayer thin films will allow the use of ultrasonic NDT of these systems. Extension of the present system to shear or even surface waves is easily accomplished by replacing the transducers, but a better couplant is required for these excitations. A more powerful amplifier will likely be necessary, especially to make use of higher excitation frequencies, which have been found to be more sensitive to thermal fatigue damage.

References

1. Halmshaw R., Non-destructive Testing, 1987, Edward Arnold Ltd., London.
2. Krautkramer J. and Krautkramer H., Ultrasonic Testing of Materials, 1969, Springer-Verlag, New York.
3. Van Vlack L. H., Elements of Materials Science and Engineering (5th ed.), 1987, Addison Wesley Publishing Co., Reading.
4. Hale D.K., "Review: The physical properties of composite materials", 1976, J. Mater. Sci., **11**, 2105-2141.
5. Sheldon R.P., Composite Polymeric Materials, 1982, Applied Science Publishers, London.
6. German Aerospace Research Establishment, Development of Fracture Mechanics Maps for Composite Materials, 1985.
7. Frost H. J. and Howard R. T., "Creep Fatigue Modelling for Solder Joint Reliability Predictions Including the Microstructural Evolution of the Solder", 1990, IEEE Transactions on Components, Hybrids, and Manufacturing Technology, **13**, 727-735.
8. Van Doorselaer K. and De Zeeuw K., "Relation Between Delamination and Temperature Cycling Induced Failures in Plastic Packaged Devices", 1990, IEEE Transactions on Components, Hybrids, and Manufacturing Technology, **13**, 879-882.
9. Darveaux R. et al., "Thermal Stress Analysis of a Multichip Package Design", 1989, IEEE Transactions on Components, Hybrids, and Manufacturing Technology, **12**, 663-672.
10. Read B.E. and Dean G. D., The Determination of Dynamic Properties of Polymers and Composites, 1978, Adam Hilger Ltd., Bristol.
11. Zimmer J.E. and Cost J.R., "Determination of the Elastic Constants of a Unidirectional Fiber Composite Using Ultrasonic Velocity Measurements", 1970, J. Acoust. Soc. Am., **47**, 795-803.
12. Bray D. E. and Stanley R.K., Nondestructive Evaluation, 1989, McGraw-Hill Book Co., New York.

13. Kittel C., Introduction to Solid State Physics (6th ed), 1986, John Wiley and Sons, Inc., New York.
14. Silk M.G., Ultrasonic Transducers for Nondestructive Testing, 1984, Adam Hilger Ltd., Bristol.
15. Blitz. J., Fundamentals of Ultrasonics (2nd ed.), 1967, Butterworths, London.
16. Beam W. R., Electronics of Solids, 1965, McGraw-Hill Book Company, New York.
17. Holbrook R.D., "A Pulse Method for Measuring Small Changes in Ultrasonic Velocity with Temperature", 1948, J. Acous. Soc. Am., **20**, 590-595.
18. McSkimin H.J., "Pulse superposition method for measuring ultrasonic wave velocities in solids", 1961, J. Acoust. Soc. Am., **33**, 12-16.
19. Papadakis E.D., "Ultrasonic phase velocity by the pulse-echo-overlap method incorporating diffraction phase corrections", 1967, J. Acoust. Soc. Am., **42**, 1045-1051.
20. Negita K. and Takao H. "Superposed pulse echo overlap method for ultrasonic sound velocity measurement", 1989, Rev. Sci. Instrum., **60**, 3519-3521.
21. ASM Engineered Material Handbook vol. 2: Engineering Plastics, 1988, ASM International, Metals Park.
22. Donnet J. and Bansal R. C., Carbon Fibers, 1984, Marcel Dekker Inc., New York.
23. Lubin G. ed., Handbook of Composites, 1982, Van Nostrand Reinhold Co., New York.
24. Weast R. C. ed., CRC Handbook of Chemistry and Physics (70th ed.), 1989, CRC Press Inc., Boca Raton.
25. Plueddemann E.D. ed., Composite Materials Volume 6: Interfaces in Polymer Matrix Composites, 1974, Academic Press, New York.
26. Chawla K.K., Composite Materials Science and Engineering, 1987, Springer-Verlag, New York.

27. Kasap S.O., Yannacopoulos S., Mirchandani V., and Hildebrandt J., "Ultrasonic Evaluation of Thermal Fatigue of Composites", 1992, *J. Eng. Mater. Tech.*, **114**, 132-136.
28. Owens G.A. and Schofield S.E., "Thermal Cycling and Mechanical Property Assessment of Carbon Fibre Reinforced PMR-15 Polyimide Laminates", 1988, *Comp. Sci. and Technol.*, **33**, 177-190.
29. Yannacopoulos S., Hildebrandt J., and Kasap S.O., "Thermal Fatigue of Composites". to appear in Proceedings of the Third International Symposium on Advanced Composites in Emerging Technologies, 1990, Patras Greece. refereed and in press.
30. Hayford D.T. and Henneke E.G., "A Model for Calculating Damage and Ultrasonic Attenuation in Composites", in Composite Materials: Testing and Design. Fifth Conference ASTM STP 674., S.W. Tsai ed., 1979, ASTM, 184-200.
31. Ahlberg L., Tittman B.R. and Elsley R.K., "NDE of Simulated Space Shuttle Tile Disbonds", Review of Progress in Quantitative NDE, D. Thompson and D. Chimenti, ed., 1982, **1**, Plenum Press, New York.
32. Pan T., "Thermal Cycling Induced Plastic Deformation in Solder Joints-Part 1: Accumulated Deformation in Surface Mount Joints", 1991, *Journal of Electronic Packaging*, **113**, 8-15.
33. Lee S. and Stone D.S., "Grain Boundary Sliding in Surface Mount Solders During Thermal Cycling", 1991, *IEEE Transactions on Components, Hybrids, and Manufacturing Technology*, **14**, 628-632.
34. Harada M. and Satoh R. "Mechanical Characteristics of 96.5Sn / 3.5Ag Solder in Microbonding", 1990, *IEEE Transactions on Components, Hybrids, and Manufacturing Technology*, **13**, 736-742.
35. Williams J.H., Lee S.L., and Wang T.K., "Nondestructive Evaluation of Strength and Separation modes in Adhesively Bonded Automotive Glass Fiber Composite Single Lap Joints", 1987, *J. Comp. Mater.*, **21**, 15-35.
36. Walter W.F. ed., Electronics Design Materials, 1971, The Macmillan Press Ltd., Hampshire.
37. Truell R. , Elbaum C., and Chick B., Ultrasonic Methods in Solid State Physics, 1969, Academic Press, New York.

38. McSkimin H.J., "Ultrasonic Methods for Measuring the Mechanical Properties of Liquids and Solids" in Physical Acoustics: Principles and Methods. W.P. Mason, ed. 1964, Academic Press, New York.

APPENDIX A
MODELS OF INTERFACIAL STRESSES

APPENDIX A: MODELS OF INTERFACIAL STRESSES

A.1 Introduction

Models exist for the problem of thermal and moisture inequilibrium effects in uniaxial fibre composites, such as the composites 1 and 2 in this study. The interfacial shear stress distributions should provide some information on how the composites are affected by thermal fatigue. The differences between the two composites should also be shown by the models, if they are sufficiently accurate. This appendix examines two models of interfacial shear stresses in these composites, and applies them to the problem studied in this work.

A.2 Modelling

Two different models of internal stresses in uniaxial composites were evaluated. Derivations by Chawla[26] and Chamis[25] were used to find estimates of the shear stress at the fibre-matrix interface for both composites 1 and 2. The two models gave very similar results. The shear stress equations and final results are presented here for both models.

A.2.1 Chawla's Model

There are some important assumptions used for both models. The Poisson's ratio of the fibres is assumed to be equal to that of the matrix material. It is assumed

that there is no slippage between the fibre and the matrix. Chawla's model requires that there is no direct loading of the fibre. This requires that the thermal expansion coefficient of the fibres themselves are zero. Given the geometric arrangement shown in Figure A.1, Chawla writes the interfacial shear stress τ as:

$$\tau = \frac{E_r \epsilon_m \beta}{2} \frac{\sinh \beta \left(\frac{L}{2} - x \right)}{\cosh \left(\frac{\beta L}{2} \right)} \quad (\text{A.1})$$

The subscripts f refer to properties of the fibre, and the subscripts m to the matrix. E is the Young's modulus, and ϵ_m is the matrix strain due to the change in temperature from thermal equilibrium, given by:

$$\epsilon_m = \Delta T \times k_m \quad (\text{A.2})$$

where ΔT is the temperature change, and k_m is the coefficient of thermal expansion of the matrix material. β in Equation A.1 is a constant determined by the material properties and geometry:

$$\beta = \left(\frac{2\pi G_m}{E_r A_f \ln \left(\frac{\pi}{2\sqrt{3} V_f} \right)} \right)^{\frac{1}{2}} \quad (\text{A.3})$$

G_m is the shear modulus of the matrix, and V_f is the volume fraction of fibre.

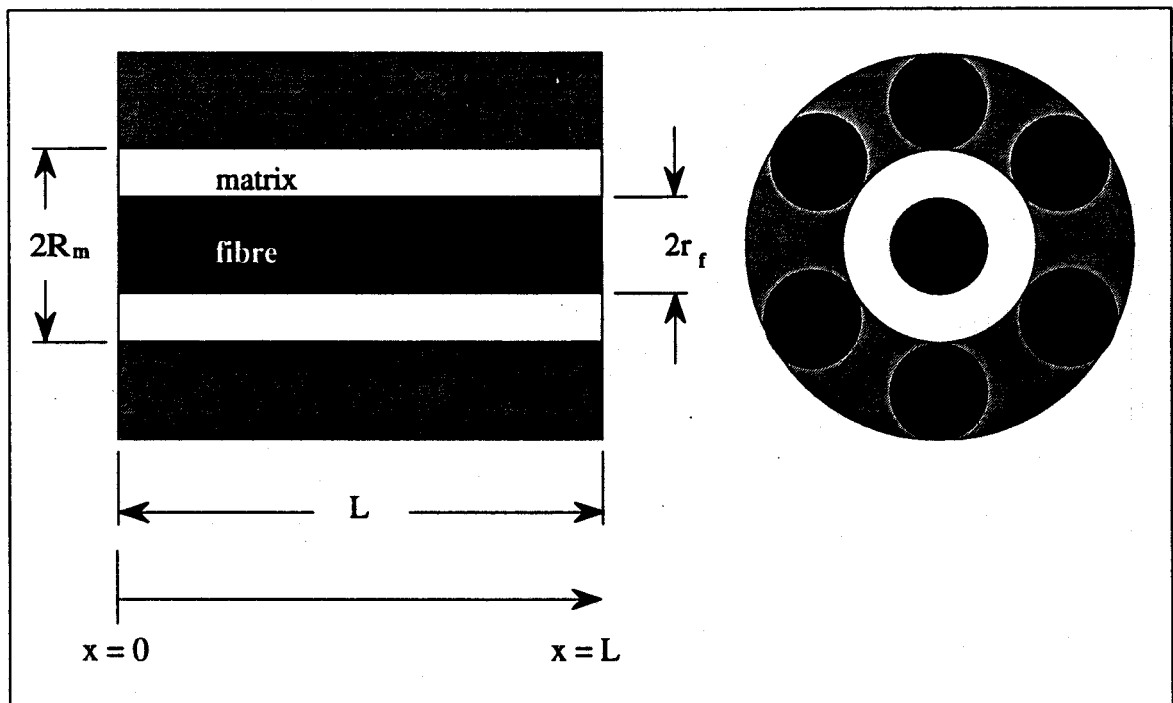


Fig. A.1 Geometrical arrangement of composite for Chawla and Chamis models.

A.2.2 Chamis' Model

Chawla's model used above is designed for the problem of load transfer from matrix to fibres. It can be extended with some assumptions to the thermal coefficient mismatch problem, and gives results similar to Chamis' model here. Chamis uses a more complex derivation, but it is more rigorous. Poisson's ratios of the fibre and matrix are not required to be the same, and the coefficient of thermal expansion of the fibre is considered. Otherwise, the same variables and the geometric arrangement of Figure A.1 are used in the following.

Chamis' result for the interfacial shear stress is:

$$\tau = \frac{E_f \lambda}{4} \varepsilon_m e^{-\frac{\lambda x}{2r_f}} \quad (\text{A.4})$$

The value λ is a constant which depends on the composite geometry and material properties, and is defined as:

$$\lambda = 2 \left(\frac{G_m}{E_f (p - 1)} \right)^{\frac{1}{2}} \quad (\text{A.5})$$

where p is determined by geometry of the fibre packing:

$$p = \begin{cases} \left(\frac{\pi}{4V_f} \right)^{\frac{1}{2}} & \text{for a square array} \\ \left(\frac{\pi}{2\sqrt{3}V_f} \right)^{\frac{1}{2}} & \text{for a hexagonal array} \end{cases} \quad (\text{A.6})$$

Both uniaxial composites examined in this work were hexagonally packed.

A.3 Modelling Results

Figures A.3 and A.4 show the results for both models for composites 1 and 2 respectively. The graphs only show the ends of the specimens, because the stress quickly becomes effectively nothing. The results are also symmetric about the halfway point in the specimen, which gives a shape like that shown in Figure A.2. It should be noted that the area of non-zero stress is greatly exaggerated, and in fact at 1mm into either composite, the models give a shear stress less than 1 Pa.

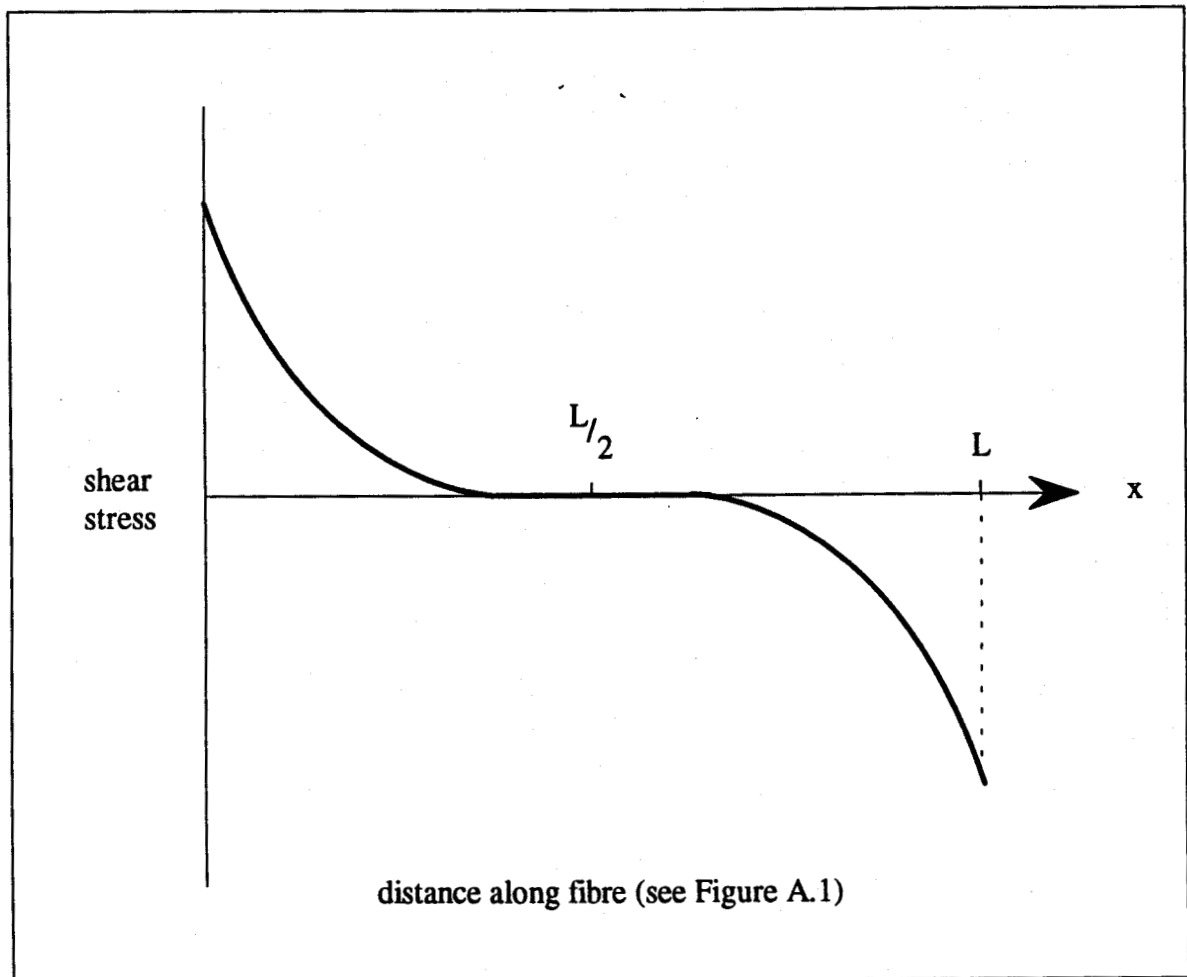


Fig. A.2 Schematic of shear stress variation in composite.

The models examined here do support the conclusions of Chapters 5 and 6, as the highest stress levels occur at the specimen ends. This would result in damage similar to that observed in these experiments, with debonding and matrix microcracking occurring at the ends of the specimens, creating scattering that would increase attenuation. Because the depths of these failure zones are so small compared to the specimen lengths, little change to the bulk properties, and thus to the ultrasonic velocity, would be expected.

The maximum shear stress in the interface is very similar for the two

composites: Chamis gives 593 kPa for composite 1 versus 612 kPa for composite 2. It was found that composite 1 was more adversely affected than composite 2 by thermal fatigue cycling. This may indicate that better bonding characteristics occur in composite 2.

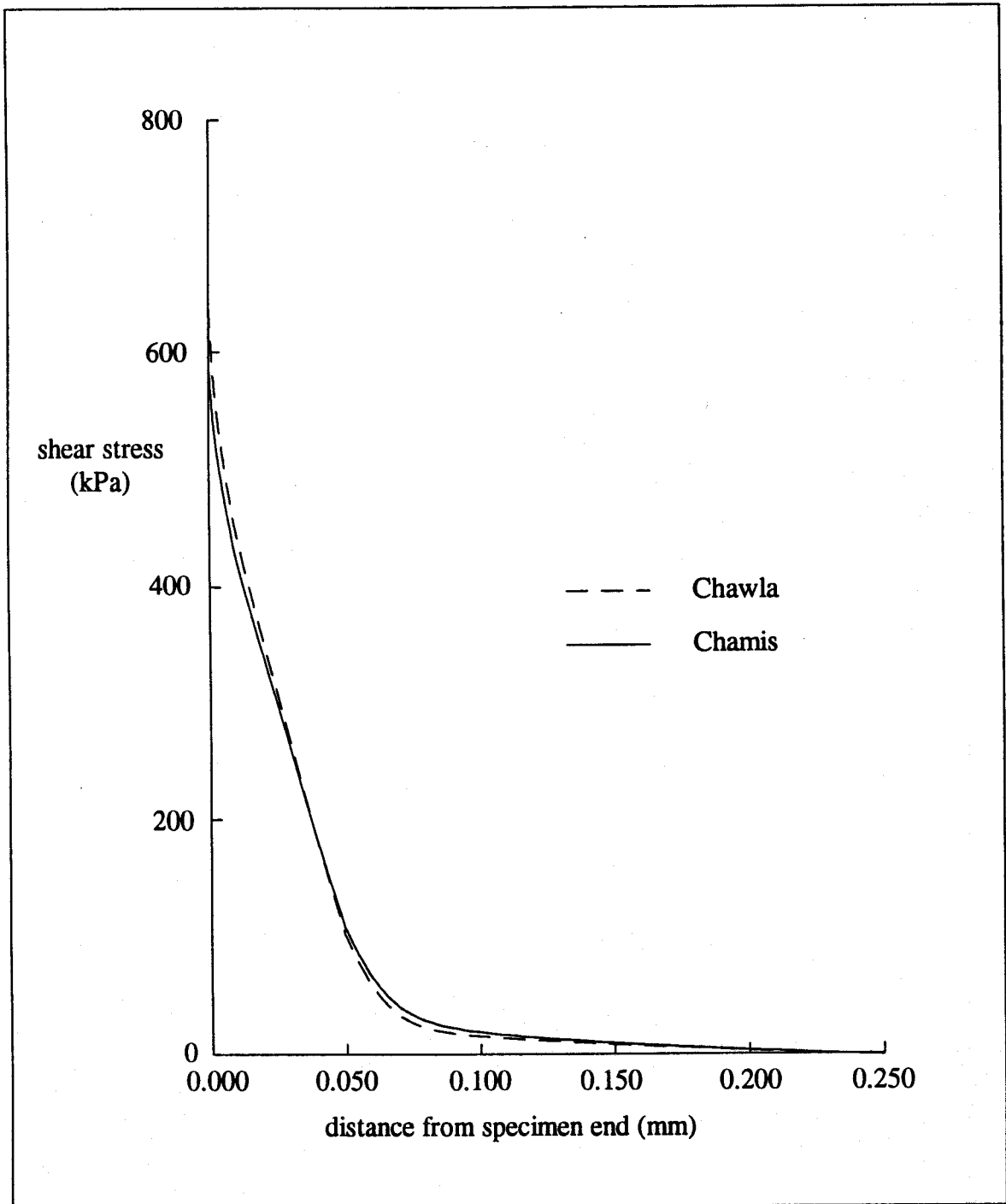


Fig. A.3 Models of interfacial shear stress for composite 1 as a function of distance from the end of the specimen.